Mission-Oriented Seismic
Research Program

An inverse scattering series algorithm for depth imaging of reflection data from a layered acoustic medium with an unknown velocity model

Ph.D. Thesis

Simon A. Shaw

March 27, 2005

M-OSRP

University of Houston

ABSTRACT

Depth imaging of seismic reflection data plays an fimportant role in discovering oil and gas reservoirs as well as in characterizing and defining the extent of previously discovered reservoirs. The quality of the image produced by current depth imaging algorithms is inextricably linked to the adequacy of the velocity model, which can be difficult to estimate, especially in geologically complex areas.

The inverse scattering series, a multidimensional direct inversion procedure, can be applied to the seismic inverse problem to directly achieve seismic processing objectives without *a priori* knowledge of the Earth's material properties. As a result, it has the potential to image reflectors in depth without requiring the actual propagation velocity. The inverse series is non-linear in the scattered field, which includes the source wavelet and a chosen reference medium's properties.

Building on concepts laid out by Weglein et al. (2001), an imaging subseries of the inverse series for a 1-D constant density variable velocity acoustic medium is isolated and analyzed. This imaging series is recognizable as a Taylor series expanded about each mislocated reflector whose approximate coefficients are leading order in the scattered field.

The leading order imaging series is shown numerically and analytically (through the derivation of a closed form) to converge for arbitrarily large finite contrasts between the actual and reference velocities and for data whose maximum frequency is finite. A condition is derived which, when satisfied, shows that the leading order imaging series improves the depths of reflectors over a linear imaging algorithm using the reference velocity. The impact of residual internal multiples on the imaging series is also studied. While the computational expense of the series algorithm is proportional to the number of terms required for a particular example, the closed form efficiently encapsulates an infinite number of terms in a single operation.

The impact of missing low frequencies on the leading order imaging series is examined. It is found that, while the algorithm benefits from having low frequency information, it retains effectiveness even when zero and some low frequencies are absent. Some improvement in the effectiveness of the algorithm when low frequency information is missing can be achieved by fixing the limits of the algorithm's integral to be over the known extent of the perturbation. The acquisition of lower frequency data, and the development of low frequency spectral extrapolation techniques support the progression of this work to eventual field data tests. To that end, some remarks are included that describe extensions of this algorithm to include higher order imaging series terms, a variable background velocity, and more complex wave propagation.

CONTENTS

1. PROBLEM STATEMENT AND RESEARCH OBJECTIVES

The primary goal of depth imaging is to produce a spatially accurate map of reflectors below the Earth's surface. This structural map is important to the oil and gas industry because it plays a key role in determining where to drill for hydrocarbon reserves which, in turn, can have an enormous global economic, environmental and political impact. The same principles that underly imaging the Earth's subsurface also apply to problems in medical and space imaging and other remote sensing and nondestructive testing methods.

Current depth imaging algorithms can be formulated from a linear inverse scattering model in which the reference velocity is assumed to be close enough to the actual velocity that reflectors are placed at their correct spatial locations. In practice, especially in complex geological environments, the most accurate methods for deriving the reference velocity model may be inadequate for linear imaging algorithms inasmuch as they fail to focus the reflected wavefield at the correct location. This motivates the search for new imaging algorithms that have the ability to accurately locate reflectors, even when the precise velocity model is not known.

Weglein et al. (2000) have proposed using the inverse scattering series, a multidimensional direct inversion procedure, to derive a velocity-independent imaging algorithm. The primary objective of this thesis is to progress that idea by developing an embryonic algorithm for the simplest models in which unknown reflectors may be imaged accurately without precise knowledge of the velocity field. Once the algorithm is derived, it will then be analyzed for convergence and under conditions where the input data are bandlimited.

1 Introduction, motivation and background

Producing oil and gas at a pace that meets current global demand while also replacing reserves to meet future demand are important objectives that have enormous economic, environmental and political implications in the world today. Seismic exploration plays a key role in defining and characterizing existing reservoirs as well as in discovering new oil and gas reservoirs.

In the seismic experiment (see Figure 1.1), a controlled source sends an incident wave into the

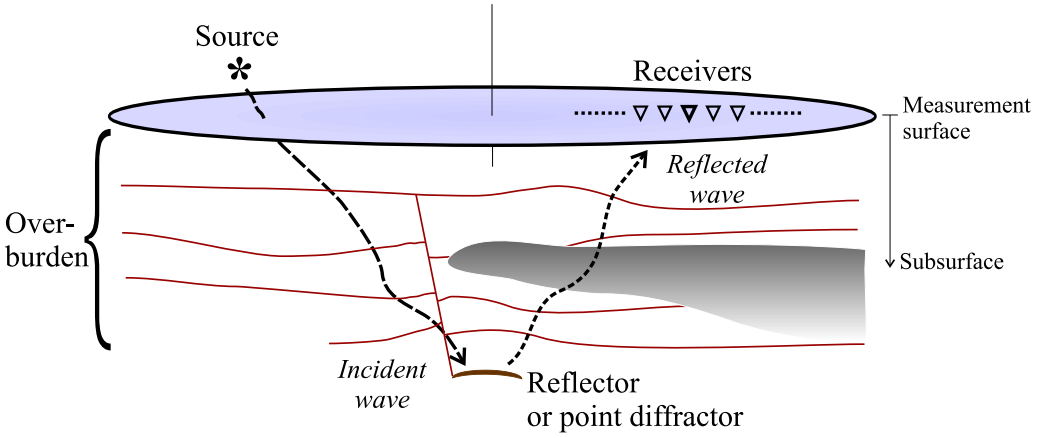

Fig. 1.1: *An illustration of the seismic experiment. A seismic survey consists of repeated shots (excitations of the source) at different locations above the measurement surface. A wave incident upon a reflector produces a reflected wave. The displayed travel paths give rise to a primary event in the recorded data.*

Earth. Rapid changes[1] in Earth properties will cause the incident wave to reflect or diffract and a portion of the reflected wave will return to the surface where it will be recorded by groups of receivers. The reflected wave contains information about the source that created it, the medium that the wave has travelled through, and the inhomogeneities (or reflectors) that caused part of the incident wave to return to the surface.

The recorded seismic data are processed to reveal information about the Earth's subsurface. Ultimately, this information is interpreted to deduce the geological structure and the size and type of possible hydrocarbon accumulation. The quality of the processed seismic data has a direct impact on our ability to find and describe reservoirs. False or inaccurate reservoir prediction can lead to drilling wells in the wrong location – an expensive mistake given that an offshore deep water well can cost more than $70 million. Such high stakes motivate research into new, more effective, seismic data processing algorithms.

Seismic data processing can be considered in the context of an inverse problem. Naturally, the seismic inverse problem will be different depending on whether we consider acoustic, elastic, or more complex wave propagation. Furthermore, methods to solve the inverse problem will depend on how many acoustic or elastic parameters govern wave propagation, and on how many spatial dimensions the Earth is considered to vary in. However, these details aside, to solve the seismic inverse problem is to process seismic reflection data to reveal the Earth's subsurface properties, including the spatial location of reflectors and contrasts in density and mechanical properties at these reflectors.

In practice, seismic data processing is carried out in a sequence of steps, e.g., random noise

[1] "Rapid changes" means rapid relative to the wavelength of the incident wave, which is a function of its temporal frequency.

attenuation, source wavelet deconvolution, removal of multiple reflections, imaging and, finally, inversion for changes in Earth properties. The order in which these steps are carried out can be important because most algorithms assume that the data have been preconditioned by preceding processes. Imaging is the processing step addressed in this thesis. To produce a seismic image is to generate a picture, or image, of the subsurface from the data recorded on the measurement surface. The most ambitious seismic imaging algorithms output a spatially accurate map of the reflectivity below the Earth's surface. In these cases, seismic imaging is the process of locating reflectors while also preserving the strength of these reflectors, which will be proportional to the impedance contrasts.

There are many different ways to produce images from seismic data. Seismic data are, in general, a function of five independent variables: source and receiver surface coordinates (x_s, y_s, x_g, y_g)[2] and source-to-receiver travel time (t). A natural way to display raw seismic data is to plot a subset of the traces (e.g., for a fixed source-receiver offset) as some function of surface location (e.g., source-receiver midpoint) on the horizontal axis and time (increasing down) on the vertical axis. A display such as this (an example of a seismic section) would be considered to be one of the most primitive images of the subsurface. It is primitive because the events on the section are (1) a superposition of primaries and reverberatory multiples (2) distorted by the wave's spatially-variable propagation velocity between the surface and the subsurface reflectors, and (3) composed of diffracted energy that has scattered in all directions from single points in the subsurface. In short, the events on this primitive seismic section are not located in a position that well-represents the subsurface reflectivity and therefore do not constitute a good image. Fortunately, many seismic processing and imaging algorithms exist that can improve upon this primitive image.

In the development of seismic imaging theory and practice (e.g., Hagedoorn, 1954; Claerbout, 1971; French, 1974; Schneider, 1978; Stolt, 1978), the term "migration" is widely used. Seismic migration refers to the moving, or migrating, of seismic events on a section to locations that better represent the structure of the subsurface. For example, migrating the primitive image just described would collapse diffractions thereby improving coherence, move dipping reflectors in an up-dip direction while making them appear steeper, and correct the distortions resulting from the wave propagating through the overburden.

Probably the most important prerequisite of current imaging algorithms is the need to know the propagation velocity *a priori*. In order to know where an unknown reflector is located in the Earth from travel times recorded at the surface, these algorithms require the velocity with which the wave has travelled on its journey from the source down to the reflector and then up to the receivers. To have this information is to have the "velocity model", which may be described in terms of, e.g., an interval velocity as a function of spatial coordinates. In one spatial dimension, and for a normal incidence experiment, it is easy to see that the relationship between the depth, z_R, to a reflector buried below an overburden with interval

[2] Consistent with much of the literature, subscript s derives from the word "shot" or "source" while subscript g derives from the word "geophone" and signifies the receiver.

velocity $c(z)$ and the travel time, t_R, for that reflection event is

$$t_R = \int_{z_s}^{z_R} \frac{dz}{c(z)} - \int_{z_R}^{z_g} \frac{dz}{c(z)} = 2\int_0^{z_R} \frac{dz}{c(z)} \tag{1.1}$$

where the source and receiver depths are, for convenience, assumed to be at $z_s = z_g = 0$. The depth to the reflector may also be written as an integral:

$$z_R = \int_0^{t_R/2} c(t)dt \tag{1.2}$$

where the velocity must be known as a function of the travel time, t. Equation (1.2), or some approximation to it, is at the heart of all current imaging algorithms. These algorithms use the velocity to predict the wavefield in the Earth from measurements at the surface. This process is called "downward continuation of sources and receivers" or "survey sinking" and is the map

$$D(x_g, y_g, z_g = 0|x_s, y_s, z_s = 0; t) \rightarrow D(x_p, y_p, z_p|x_p, y_p, z_p; t). \tag{1.3}$$

At each point (x_p, y_p, z_p) in the Earth that the wavefield is predicted, an imaging condition is applied that returns the strength of the local reflectivity, or image I, at that point (see, e.g., Stolt and Benson, 1987, p. 141). The $t = 0$ imaging condition relies on the reflected wavefield at small times carrying information only about the medium near the location of the coincident source and receiver:

$$I(x, y, z) \sim D(x, y, z|x, y, z; t = 0) \tag{1.4}$$

There is an inherent paradox in current imaging theory called the *velocity paradox* (Stolt and Benson, 1987). The data are back propagated through a volume, whose velocity is assumed to be known, in search of sharp discontinuities (i.e., reflectors). However, reflectors are themselves likely to be evidence of rapid changes in the velocity. How can we be propagating the wavefield through the correct velocity model if we don't know where the rapid changes are? This dichotomy is also evident when we consider current imaging as part of the general inverse problem. On the one hand, we often consider imaging as a preprocess to amplitude versus angle (AVA) analysis, which is a procedure for estimating the changes in parameters across reflectors in the Earth. Since velocity is one of these parameters, then how is it that we need the velocity to image, and yet we still consider it an unknown when we perform AVA analysis?

The velocity paradox has been explained by the fact that, while the wave does indeed respond to rapid changes in the velocity, in the end, its net response is to an integral of the velocity over the distance that it has propagated. Another point of view considers the notion of "two velocities": one slowly-varying *known* background velocity, upon which is superimposed a rapidly-varying *unknown* velocity. The latter discontinuous velocity is one possible mechanism responsible for generating the unknown reflectors. The background

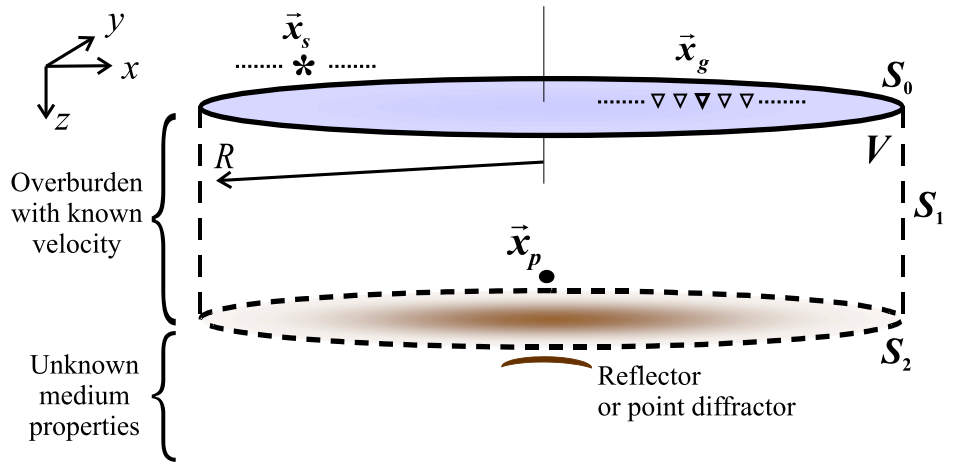

Fig. 1.2: The model behind current linear seismic imaging algorithms. In order to image a reflector, the algorithms downward continue the data from the surface, S_0, to points in the subsurface, e.g., $\vec{x}_p = (x_p, y_p, z_p)$, using a velocity model that is assumed to be adequately known inside the source-free volume, V. By applying an imaging condition, the reflectivity in the subsurface is estimated.

velocity is assumed to be adequate in its ability to focus the wavefield at depth and, hence, it should correctly position reflectors.

The second viewpoint is closer to the one adopted in this thesis where we are using scattering theory to address the problem of imaging. However, the important distinction between current imaging and the approach we are taking here is that we formulate the problem in terms of chosen background, or reference, velocity model that we anticipate is inadequate. In doing so, the solution to the inverse problem is an infinite series: the inverse scattering series. As a multidimensional direct inversion procedure, the inverse series has the ability, in principle, to locate the sharp discontinuities using only the approximate reference velocity model (Weglein et al., 2000). In the event that the chosen reference velocity is equal to the actual velocity in the medium, then the solution to the imaging problem is linear in the data, non-linear terms in the series will be zero, and the algorithm should behave in a manner similar to a current, conventional, imaging algorithm.

The requirement in current imaging theory to have the velocity model can be illustrated using a constant-density acoustic wave equation. Considering the situation illustrated in Fig. 1.2, the wave equation valid inside and on the surface of the volume, V, is

$$\left(\nabla^2 + \frac{\omega^2}{c^2(\vec{x}\,')}\right)\psi(\vec{x}\,';\omega) = 0 \tag{1.5}$$

where c is the velocity. Predicting the wavefield in the subsurface (i.e., inside the volume, V) from measurements on the surface is the first step in a current imaging algorithm and is

the one that requires the velocity model. We write an equation for the Green function, G, that has its source located at the subsurface point $\vec{x}_p$

$$\left(\nabla^2 + \frac{\omega^2}{c^2(\vec{x}\,')}\right) G(\vec{x}\,'|\vec{x}_p;\omega) = -\delta(\vec{x}\,' - \vec{x}_p) \tag{1.6}$$

and then apply Green's Theorem to derive a wavefield prediction formula (Morse and Feshbach, 1953)

$$\psi(\vec{x}_p|\vec{x}_s\,;\omega) = \oint \left(\psi(\vec{x}\,'|\vec{x}_s\,;\omega)\frac{\partial G(\vec{x}\,'|\vec{x}_p;\omega)}{\partial n} - G(\vec{x}\,'|\vec{x}_p;\omega)\frac{\partial \psi(\vec{x}\,'|\vec{x}_s\,;\omega)}{\partial n}\right) dS\ ,\ \vec{x}\,' \in S \tag{1.7}$$

where the partial derivatives are with respect to the outward-pointing normal to the surface, $S = S_0 + S_1 + S_2$. While Eq. (1.7) is very general and applies to two-way wavefields (and can be rederived for elastic wave propagation *c.f.* Betti's Theorem), at first look, it appears somewhat demanding. For one thing, it asks for two measurements: one of the pressure field, ψ, and one of its normal derivative, $\partial\psi/\partial n$. Furthermore, it requires these values on a closed surface, S, which is not feasible in seismic exploration.

Equation (1.7) may be simplified in the following ways: (1) Assume that the radius of the cylinder goes to infinity ($R \to +\infty$). In doing so, the contributions to the surface integral from the sidewalls of the cylinder vanish (see, e.g., Wapenaar et al., 1989) leaving only S_0 and S_2. This observation is not a consequence of the Sommerfeld radiation condition, which applies only to causal wavefields (Bleistein, 1984). The consequence of collecting finite aperture data is to ignore the contribution from the surface S_1; (2) Assume that the wavefield at the upper surface, S_0 and inside the volume, V, is purely upgoing[3] so that $\psi = \psi_U$. To realize this, we should remove all downgoing waves from our data, including the direct wave, source and receiver ghosts, free surface multiples and internal multiples. We may now imagine that the waves arriving at the receivers have radiated from a secondary source – the reflectors or point scatterers – below the surface S_2. We then choose the anticausal (also known as time-reversed or advanced) Green function, $G = G^*$. This assumption and choice simultaneously removes the need for a measurement at S_2 (save perhaps some contribution from the evanescent part of the wavefield – see Stolt, 1984; Stolt and Benson, 1987; Wapenaar et al., 1989; Wapenaar, 1992); (3) Lastly, we are free to choose boundary conditions for the Green function, G^*. Equivalently, the medium and sources outside the volume, V, may be defined purely for convenience. If we choose Dirichlet boundary conditions on S_0 such that $G^{*\mathrm{D}}(\vec{x}\,' = \vec{x}_g\,|\vec{x}_p;\omega) = 0$, then we eliminate the need to measure the normal derivative of the wavefield, $\partial\psi/\partial n$, in Eq. (1.7). To realize this boundary condition on a horizontal acquisition surface, we may imagine a second impulsive source located at a point $\vec{x}_p^{\,I} = (x_p, y_p, 2z_g - z_p)$ with opposite sign to the source at $\vec{x}_p$, and a medium that is symmetric about S_0 so that $c(x', y', z_g - z') = c(x', y', z_g + z')$. Then $G^{*\mathrm{D}}$ satisfies the equation

$$\left(\nabla^2 + \frac{\omega^2}{c^2(\vec{x}\,')}\right) G^{*\mathrm{D}}(\vec{x}\,'|\vec{x}_p, \vec{x}_p^{\,I};\omega) = -\delta(\vec{x}\,' - \vec{x}_p) + \delta(\vec{x}\,' - \vec{x}_p^{\,I}) \tag{1.8}$$

[3] It may still be up- and down-going below S_2.

The resulting formula for the upgoing wavefield predicted inside the volume, V, is

$$\psi_U(\vec{x}_p;\omega) = -\iiint_{-\infty}^{+\infty} \psi_U(\vec{x}_g\,;\omega)\frac{\partial G^{*\mathrm{D}}(\vec{x}_p|\vec{x}_g\,;\omega)}{\partial z_g}d\vec{x}_g \ \text{, where } \vec{x}_g \in S_0. \tag{1.9}$$

The minus sign comes from taking the normal derivative on the upper surface, S_0, given that the z axis is defined to be positive down. We see that the wavefield at depth can be computed through a weighted sum of the data recorded at the surface. It is the weighting function $\partial G^{*\mathrm{D}}/\partial z_g$ that requires the velocity model in order to predict the wavefield in the Earth[4].

After downward continuing the receivers for each source experiment, we may invoke the principle of reciprocity and then re-apply Eq. (1.9) to downward continue all sources to the subsurface point $\vec{x}_p$. The last step in current imaging is to apply an imaging condition. If there is a reflector just below $\vec{x}_p$ (given the upgoing wave assumption) then the imaging condition returns an amplitude proportional to the strength of that reflector. If there is no reflector nearby, then the wavefield predicted at that point returns zero.

Almost universally, imaging is applied to primary seismic events and it is assumed that multiples have already been removed (or well attenuated) before the algorithm is applied. This assumption still doesn't guarantee that $\psi = \psi_U$ inside the volume, V. There are velocity models that produce turning waves and that cause the incident wave to be upgoing at the reflector, rather than downgoing. Reverse time migration (Baysal et al., 1983; McMechan, 1983; Whitmore, 1983; Esmersoy and Oristaglio, 1988) accommodates two-way wave propagation and can be applied to image primary seismic events under these conditions. In principle, reverse time migration can also accept multiple reflections in the input data (e.g., Youn and Zhou, 2001; Mittet, 2002; Jiang et al., 2005).

How different migration algorithms incorporate the velocity model through Eq. (1.9) is what differentiates time migration from depth migration. The nuances of time migration and depth migration, and the details surrounding algorithms for pre-stack or post-stack data, that accommodate velocity models $c(z), c(x,z)$ or $c(x,y,z)$, and that do or don't make limiting assumptions about wave propagation, e.g., Kirchhoff, Gaussian beam or wave-equation are all beyond the scope of this thesis, but may be found in a number of texts (e.g., Claerbout, 1985; Berkhout, 1985; Stolt and Benson, 1987; Scales, 1997). The implementation of migration algorithms receives a great deal of attention in contemporary literature, whereas the theory behind the algorithms essentially remains the same. When an adequate velocity model is available, these algorithms, given their underlying assumptions, produce good images of the subsurface. According to Gray (2001), the future of imaging research that stays close to this established theory will tend to be focused on (a) improving the amplitude of the wavefield predicted in the subsurface, (b) algorithm development for faster and higher capacity computers, and (c) handling multi-component recordings of elastic wavefields. The

[4] It can be shown that if we chose to not impose the boundary condition $G^{*\mathrm{D}}(\vec{x}\,' = \vec{x}_g\,|\vec{x}_p;\omega) = 0$, then we would, of course, derive an equivalent formula – just with the substitution $\partial G^{*\mathrm{D}}/\partial z_g = 2\partial G^{*}/\partial z_g$.

quality, accuracy and reliability of the image from current imaging algorithms is inextricably dependent on the adequacy of the velocity model.

In practice, imaging is itself one of the procedures used to estimate the velocity model. Through an iterative process, the quality of an image may be quantitatively or qualitatively measured and can be used to update the velocity model. Although critically important to current seismic imaging, a detailed discussion of these and other velocity estimation techniques is beyond the scope of this thesis. For an overview of, and references to, velocity estimation methods, see, for example, Gray et al. (2001). One of the primary motivations for this research is that, under many circumstances, especially in complex geological environments, current best-practice velocity estimation techniques are inadequate for estimating the velocity model with a high-enough degree of accuracy (e.g., Herron, 2000; Gray et al., 2001; Paffenholz et al., 2002; Glogovsky et al., 2002). There are two responses to this problem: first, to improve our ability to estimate the velocity model and, second, to derive new imaging algorithms that are less dependent on our ability to find the velocity model. The research described in this thesis is an example of the second response.

In recent years, there has been some interest in velocity-independent imaging approaches. A workshop titled "Velocity Model Independent Imaging for Complex Media" was held at the 2001 SEG Annual Meeting in San Antonio, Texas. A number of different approaches to the problem were presented at the workshop, including common focus point (Berkhout and Verschuur, 2001), common reflection stacking (Bergler et al., 2002; Mann et al., 1999), the inverse scattering series (Weglein et al., 2001), and multi-focusing analysis (Landa, 2004; Gelchinsky, 1989; Berkovitch and Gelchinsky, 1989). With the exception of the inverse series approach, these methods can be seen as generalizations of normal moveout (NMO) and stack, some of which forgo knowing the velocity model in exchange for estimates of one or more unknown parameters which are optimized to produce the "best" (e.g., most coherent) image. The inverse series is the only one of these techniques that has the potential to produce directly an image in depth, rather than an image in time. In all inverse scattering approaches (both linear and non-linear), the reference velocity yields units of depth from the data recorded in time. However, a non-linear series of equations is required to get an accurate image in depth when the actual velocity deviates from the reference velocity.

2 Objectives

This thesis is part of a long-term research project aimed at solving the problem of seismic imaging of, and inversion for, large-contrast and complex targets located beneath an unknown, or poorly defined, overburden (Weglein et al., 2003). Complex geologic environments that currently present some of the greatest challenges to exploration include subsalt, sub-basalt, and sub-karsted sediments. Estimating the velocity model in order to image beneath these types of complex overburdens can be extraordinarily difficult. The objectives of the research project are to study these problems and to propose, test and evaluate solutions with a view to developing practical algorithms. A practical algorithm is one that

provides value under real-world conditions and will become one tool in a toolbox of established processing algorithms. Naturally, we would expect algorithms that provide benefit under complex conditions to also provide value in more simple geological environments.

The objectives of this Ph.D. thesis are more narrowly defined. We are investigating the use of the inverse scattering series to image reflectors at their correct depth. In principle, the inverse series will accomplish this task using a reference velocity that may deviate from the actual velocity below the measurement surface. At this stage, in order to make the problem more tractable, we confine our analysis to the acoustic wave equation, and for a velocity that varies only in the vertical direction. We follow closely the analysis of Weglein et al. (2001) and Weglein et al. (2002), where the authors show that the first term in the inverse series images reflectors at depths dictated linearly by the reference velocity and the data's travel times and that higher order terms contain parts that serve to shift reflectors towards their true depths through Taylor series expanded about the mislocated interfaces. In this thesis, we seek to use this analysis to further our understanding of how the inverse series performs imaging, and to use the principle of task separation, originally developed for the purposes of deriving free surface and internal multiple attenuation algorithms (Weglein et al., 1997), to isolate an imaging subseries. Successful isolation of an imaging series must be followed by an analysis of its convergence properties, and testing under increasingly realistic data conditions, such as finite frequency bandlimits, additive noise, etc.

3 Strategy – the importance of starting simple

As a multi-dimensional inversion procedure, the inverse series can be readily formulated for all linear wave equations. Then why are we studying the relatively simple 1-D acoustic problem when the Earth is, at best, a 3-D elastic medium? The straightforward answer to this question is that if an algorithm shows no effectiveness for the simplest 1-D acoustic models, then we can not justify the additional labor and mathematical formalism involved in its generalization to more complex wave propagation.

Historically, the strategy employed in developing inverse scattering subseries algorithms to seismic data processing objectives has been to first consider the simplest situation in which the particular problem exists. Most often this is a 1-D normal incidence experiment in a constant-density acoustic medium. The simplest reference medium is chosen that agrees with the actual medium above the measurement surface and thereby confines the perturbation to be below the receivers. Then the inverse series is analytically computed and a subseries is sought that is responsible for achieving the specific processing task under investigation. The inverse subseries is isolated through a combination of physical intuition and experience garnered through studying the *forward* Born series which constructs the seismic wavefield using only reference propagation.

For the task of imaging, the simplest example to study is that of two reflectors where we know the velocity down to the shallowest reflector but do not know the velocity below it.

In this case, the first term in the series (computed with a homogeneous reference velocity) will correctly locate the shallowest reflector, but incorrectly locate the deeper one. Furthermore, the first term will contain internal multiples that have reverberated between the two reflectors, and the amplitudes of the events will be composed of reflection and transmission coefficients rather than actual changes in the medium property. Collectively, the higher order terms in the inverse scattering series are responsible for (1) removing internal multiples, (2) moving the deeper reflector to its correct location, and (3) inverting the amplitudes for changes in the Earth material properties. In this thesis, we are concerned with the terms that act on the mislocated deeper reflector. We seek to isolate a subseries of the inverse series that is responsible for locating reflectors in space when the actual velocity model is unknown. If this subseries algorithm demonstrates an intrinsic ability to achieve its objective for the simplest synthetic examples, then it will be reformulated and generalized so that it may be tested on multidimensional field data.

2. THE INVERSE SCATTERING SERIES AND TASK-SPECIFIC SUBSERIES

As a multidimensional direct inversion procedure, the inverse scattering series can be formulated to invert seismic reflection data directly for the Earth's material properties. Using only the measured data, the source wavelet, and a reference medium's material properties as input, the inverse series is a procedure that achieves important seismic processing objectives through combined linear and non-linear operations on the data. It serves as a general and flexible foundation for deriving seismic processing algorithms that are effective when little or no *a priori* information about the subsurface is available. In the context of this thesis, the inverse series is a good candidate procedure for deriving an algorithm that can accurately depth image seismic data in complex geological areas where the velocity model is difficult to estimate.

To address issues of divergence or slow convergence of the inverse series, an effective strategy has been to isolate subseries of the inverse series that are responsible for accomplishing specific useful tasks in seismic processing. Series algorithms for the removal of free surface multiples and the attenuation of internal multiples were presented by Weglein et al. (1997). These two multiple attenuation algorithms were successfully tested on, and are now routinely applied to, 2D and 3D field datasets. They are distinguished by the useful property of requiring no knowledge of the Earth's properties below the measurement surface. The potential of the inverse series to image and invert primaries was outlined by Weglein et al. (2000) and ideas for isolating terms that would constitute an imaging subseries were presented by Weglein et al. (2002).

Inverse series algorithms are able to achieve their objectives without subsurface information because they involve non-linear operations on the measured data. As such, they engage the data more actively and inclusively than linear algorithms, which treat the data more passively.

1 Scattering theory, the inverse series and seismic data processing

The research documented in this thesis applies inverse scattering theory to the seismic inverse problem. In scattering theory, the difference in the behavior of an incident wave in two media (referred to as the *reference* medium and the *actual* medium) is described in terms of the

difference between the physical properties of these two media (see, e.g., Taylor, 1972). The wave equations for the actual and reference wavefields (ψ and ψ_0) are expressed by

$$\mathbf{L}\psi = -A(\omega)\delta(\vec{x} - \vec{x}_s) \tag{2.1}$$
$$\mathbf{L}_0\psi_0 = -A(\omega)\delta(\vec{x} - \vec{x}_s) \tag{2.2}$$

where $\mathbf{L}$ and $\mathbf{L}_0$ are the differential operators that describe wave propagation in the actual and reference media, respectively, and $A(\omega)$ is the source wavelet as a function of angular temporal frequency. The variables $\vec{x}$ and $\vec{x}_s$ are the field point and source position vectors. The Green functions for the actual medium and the reference medium (G and G_0, respectively) satisfy

$$\mathbf{L}G = -\delta(\vec{x} - \vec{x}_s) \tag{2.3}$$
$$\mathbf{L}_0G_0 = -\delta(\vec{x} - \vec{x}_s) \tag{2.4}$$

and so $\psi = AG$ and $\psi_0 = AG_0$. The perturbation operator, $\mathbf{V}$, and the scattered wavefield, ψ_s, are defined by

$$\mathbf{V} \equiv \mathbf{L} - \mathbf{L}_0 \tag{2.5}$$
$$\psi_s \equiv \psi - \psi_0, \tag{2.6}$$

respectively. The Lippmann-Schwinger equation relates the actual and reference wavefields to the perturbation operator (or scattering potential):

$$\psi(\vec{x}\,|\vec{x}_s\,;\omega) = \psi_0(\vec{x}\,|\vec{x}_s\,;\omega) + \iiint_{-\infty}^{+\infty} G_0(\vec{x}\,|\vec{x}\,';\omega)V(\vec{x}\,';\omega)\psi(\vec{x}\,'|\vec{x}_s\,;\omega)d\vec{x}\,'. \tag{2.7}$$

This equation is not a solution for the actual wavefield, ψ, but can be successively iterated for ψ on the right-hand side resulting in the forward, or Born, series:

$$\psi = \psi_0 + \psi_1 + \psi_2 + \ldots = \sum_{n=0}^{\infty} \psi_n \tag{2.8}$$

where

$$\psi_1(\vec{x}\,|\vec{x}_s\,;\omega) = \iiint_{-\infty}^{+\infty} G_0(\vec{x}\,|\vec{x}\,';\omega)V(\vec{x}\,';\omega)\psi_0(\vec{x}\,'|\vec{x}_s\,;\omega)d\vec{x}\,' \tag{2.8a}$$

$$\psi_2(\vec{x}\,|\vec{x}_s\,;\omega) = \iiint_{-\infty}^{+\infty} G_0(\vec{x}\,|\vec{x}\,';\omega)V(\vec{x}\,';\omega) \times \iiint_{-\infty}^{+\infty} G_0(\vec{x}\,'|\vec{x}\,'';\omega)V(\vec{x}\,'';\omega)\psi_0(\vec{x}\,''|\vec{x}_s\,;\omega)d\vec{x}\,''\,d\vec{x}\,' \tag{2.8b}$$

$$\vdots$$

Clearly, the forward series is a solution for the actual wavefield in terms of the reference wavefield and the perturbation (the source wavelet, A, factors out and cancels on both

sides of the equation but is still required if constructing ψ and not G). It describes the wavefield that propagates in the *actual* medium in terms of an infinite series of propagations in a *reference* medium and interactions with the potential, V, which contains the actual and reference media properties. As a forward modelling tool, the forward series may be considered unnecessarily complicated or inefficient because to know V is to know the Earth (since references medium properties are a matter of choice), and therefore the wavefield can be straightforwardly constructed using a conventional (e.g., finite difference) modelling program that propagates waves through a known model. Nevertheless, the forward series is worth studying for a number of reasons. Convergence of the forward series is a necessary, but not sufficient, condition for convergence of the *inverse* series (Prosser, 1976). Also, understanding how the forward series constructs one wavefield through the propagation of another wavefield can offer clues as to how the inverse series processes the recorded wavefield using only reference propagation (see, e.g., Matson, 1996; Innanen, 2003; Nita et al., 2004).

The inverse scattering series is a solution for the scattering potential in terms of the scattered field on the measurement surface, $(\mathbf{\Psi} - \mathbf{\Psi}_0)_m = (\mathbf{\Psi}_s)_m = \psi_s(\vec{x}_g\,|\vec{x}_s\,;\omega)$, and reference propagation, $\mathbf{G_0}$. The inverse series can be derived by first writing $\mathbf{V}$ as the sum of constituent terms (Jost and Kohn, 1952; Moses, 1956)

$$\mathbf{V} = \mathbf{V}_1 + \mathbf{V}_2 + \mathbf{V}_3 + \ldots = \sum_{n=1}^{\infty} \mathbf{V}_n \tag{2.9}$$

where $\mathbf{V}_n$ is defined as the portion of $\mathbf{V}$ that is n^{th} order in the measured values of the scattered field, $(\mathbf{\Psi}_s)_m$. Substitution of Eq. (2.9) into the forward series (Eq. 2.8) and matching terms that are equal order in $(\mathbf{\Psi}_s)_m$ yields:

$$(\mathbf{G}_0\mathbf{V}_1\Psi_0)_m = (\mathbf{\Psi}_s)_m \tag{2.9a}$$
$$(\mathbf{G}_0\mathbf{V}_2\Psi_0)_m = -(\mathbf{G}_0\mathbf{V}_1\mathbf{G}_0\mathbf{V}_1\mathbf{\Psi}_0)_m \tag{2.9b}$$
$$(\mathbf{G}_0\mathbf{V}_3\Psi_0)_m = -(\mathbf{G}_0\mathbf{V}_1\mathbf{G}_0\mathbf{V}_1\mathbf{G}_0\mathbf{V}_1\mathbf{\Psi}_0)_m - (\mathbf{G}_0\mathbf{V}_2\mathbf{G}_0\mathbf{V}_1\mathbf{\Psi}_0)_m - (\mathbf{G}_0\mathbf{V}_1\mathbf{G}_0\mathbf{V}_2\mathbf{\Psi}_0)_m \tag{2.9c}$$
$$\vdots$$

To solve Eq. (2.9) given the source wavelet, A, one could invert Eq. (2.9a) for V_1, then substitute V_1 into Eq. (2.9b) and invert for V_2 using the same reference Green functions. Then V_1 and V_2 may be substituted into Eq. (2.9c) to solve for V_3, and so on. In this way, V is constructed order by order in the data and the inverse problem may be solved. See, for example, Weglein et al. (1981) for references to the development of the inverse series.

Equation (2.9a) should not be confused with the inverse Born approximation, which is

$$(\mathbf{G}_0\mathbf{V}\mathbf{\Psi}_0)_m \approx (\mathbf{\Psi}_s)_m. \tag{2.10}$$

The first term in the inverse series, V_1, becomes the inverse Born approximation only if we assume that $\mathbf{V_1} \approx \mathbf{V}$. In deriving the inverse series, there is no requirement that $\mathbf{G}_0 \approx \mathbf{G}$, nor that the reference medium properties are close to the actual medium properties. This

is the reason why algorithms derived from the inverse series have the potential to achieve processing objectives without *a priori* information about the Earth's material properties, and is the reason why, in principle, the inverse series can locate unknown reflectors in the subsurface without knowledge of the velocity model.

The inverse Born approximation, or linear inverse, underlies the vast majority of techniques currently employed to process primaries, e.g., normal moveout (NMO), migration/imaging, amplitude variation with angle (AVA) analysis and migration-inversion (see, e.g., Stolt and Weglein, 1985). Linear approximate inverse methods are also at the heart of medical imaging and other non-destructive testing methods. For the seismic problem, the inverse Born approximation is a reasonable approximation for primary events (i.e., assuming multiples have been removed), for precritical reflections, for small contrasts in material properties, and for a reference medium that is close to the actual medium (Clayton and Stolt, 1981). When these conditions do not apply, the inverse Born approximation may be inadequate as a basis for deriving processing algorithms.

The inverse series only exists when $\mathbf{L} \neq \mathbf{L}_0$ in which case $\mathbf{V}$ is non-zero. In the inverse series, $\mathbf{V}_1$ is defined to be the first term in an infinite series for $\mathbf{V}$ and Eq. (2.9a) is an exact equation, unlike Eq. (2.10) which is an approximation. The cumulative sum of the second and higher terms in the inverse series can be viewed as correcting $\mathbf{V}_1$ towards $\mathbf{V}$ when the series converges. The tasks of removing multiples, imaging primaries at their correct depths, and inverting for large changes in Earth properties reside in the second and higher order terms in the series. In other words, under circumstances where the inverse Born approximation is invalid or inadequate, the inverse series offers an alternative solution to the inverse problem.

The inverse scattering series is a multi-dimensional direct inversion procedure. The scattering medium's properties are directly determined from the recorded data without iterative updating of the reference medium towards the actual medium. Alternative approaches, e.g., iterative linear inversion, involve updating the reference model so that the reference wavefield, in some sense, fits the observed data (Tarantola, 1987). The inverse series is a distinctly different method from iterative linear inversion. Equations (2.9a,b,c,...) are inverted for $\mathbf{V}_1, \mathbf{V}_2, \mathbf{V}_3, \ldots$ and hence for $\mathbf{V}$ directly in terms of the measured data, $(\mathbf{\Psi}_s)_m$, and reference propagation, $\mathbf{G}_0$. Iterative linear inversion implicitly or explicitly updates the reference medium and scattered field at each iteration.

2 Series convergence, task-separation and task-specific subseries

Series algorithms naturally carry with them questions of convergence. A body of work by Prosser (1969–1992) has formerly addressed the topic of convergence of the inverse series including the existence and uniqueness of its solution. The convergence of the inverse series requires that the scattering potential be sufficiently weak to allow convergence of the forward series. However, Prosser's conditions are not easily translated into contrasts in Earth's material properties, such as actual/reference velocity contrasts.

Empirical tests of the *entire* inverse series for a simple 1-D acoustic model have suggested that it is slow to converge or that it does not converge unless reference medium properties are chosen to be very close to the actual medium properties (Jacobs, 1980; Carvalho, 1992). Based on these tests, the radius of convergence was considered to be too small for the series to be of direct practical use when no *a priori* information is supplied. Rather than abandon the inverse series, research was undertaken to isolate convergent subseries that perform individual tasks associated with inversion and that have practical value all by themselves (e.g., multiple removal). The fact that task-specific subseries can be isolated is quite remarkable and is not at all obvious. The thought that the inverse series might provide some benefit as a multiple removal procedure was suggested by Stolt and Jacobs (1980) and pursued by Carvalho et al. (1991) and Weglein et al. (1992). To find and isolate subseries requires a clear definition of the processing objective and a careful analysis of how the inverse series directly inverts seismic data. When successful, this analysis provides an understanding of how to process seismic data in the absence of *a priori* subsurface information, which leads to the development of practical and useful algorithms (Weglein et al., 2003).

Inversion of seismic data can be viewed as performing a sequence of four tasks or processing steps:

1. Removal of free-surface multiples;
2. Removal of internal multiples;
3. Positioning reflectors at their correct spacial locations (imaging); and
4. Inverting reflectivity for changes in Earth parameters (target identification).

As a direct inversion procedure, the inverse series accomplishes these tasks using only measured data, the source wavelet, and reference medium properties. It is anticipated that each of these tasks is achieved through a series – a subseries of the inverse series. Isolating and then employing subseries that perform these tasks is less ambitious than a wholesale direct inversion for Earth properties using the entire series and so convergence properties and data requirements may be more favorable. Also, by carrying out these tasks in sequential order, tasks 2–4 may benefit from the simplification that derives from a reformulation of the inverse problem to reflect the fact that some processing objectives have already been achieved. For each task, the simplest possible reference medium is chosen that allows rapid convergence of the subseries.

The strategy of task separation originally led to the development of a multi-dimensional free surface multiple removal algorithm (Carvalho, 1992). Free surface multiples are events in the data that have reflected in the subsurface, hit the free surface at least once, and travelled back into the Earth to be recorded at a later time. These events usually have large amplitudes and can obscure reflection events that have travelled further into the Earth but arrive at the same time as the multiples. The presence of multiples often precludes accurate estimation of the medium properties, such as the velocity model. The second task-specific

subseries to be isolated was one that attenuates internal multiple reflections (Araújo, 1994). Internal multiples are events that have all their downgoing reflections below the free surface. Removing all multiples from the data is a prerequisite for most imaging algorithms which expect a primaries-only wavefield as input. It is interesting to note that these subseries of the inverse series act to *remove* multiples (thereby treating them as noise) rather than to *use* them to extract information about the Earth.

Beyond multiple attenuation, Weglein et al. (2000) proposed using the inverse scattering series to perform the third and fourth inversion tasks of imaging reflectors in depth and inverting for Earth parameters, both in terms of reference medium information. The authors described a scheme for predicting the wavefield in the subsurface order by order in the wavefield measured at the surface and without knowing the velocity or any other properties of the medium below the measurement surface.

The concepts surrounding the task of depth imaging using the inverse series were set out by Weglein et al. (2002), where it was shown for a 1-D normal incidence experiment in an acoustic medium, that the imaging subseries was a Taylor series in the data linearly imaged with the reference velocity. This series shifts reflectors towards their true depths using the amplitude and residual moveout information gleaned automatically from the imaged data itself.

Zhang and Weglein (2003) generalized the task-separated formulation of Weglein et al. (2002) to a two-parameter acoustic model and demonstrated the benefit of adding the second terms to the first terms in the subseries for estimating changes in velocity and density across an interface. The accuracy of the parameter estimation clearly improved for all precritical angles of incidence. The authors have begun generalizing their work for elastic media (Zhang and Weglein, 2004a).

For the same normal incidence acoustic case studied by Weglein et al. (2002), Innanen (2003) isolated a subseries that simultaneously images and inverts for changes in the velocity. This subseries includes so-called "mixed-task" terms that invert and image concurrently. Numerical examples were presented that show good results for a suite of examples and demonstrated robustness to small amounts of random noise.

3 Characteristics of inverse scattering series algorithms

The multiple attenuation algorithms derived using the inverse series have the unique property that they expect the recorded seismic data and the source wavelet as input, but do not require the propagation velocity or any other subsurface information (Weglein et al., 1997). For marine seismic data, both the free surface and internal multiple subseries converge for a simple homogeneous acoustic reference medium – water – which has the benefit of making the algorithms more computationally efficient than if a reference medium more like the actual Earth were required. More importantly, the algorithms predict and attenuate multiples generated by actual Earth model types that are much more complicated than

the homogeneous acoustic reference medium and include heterogeneous, anisotropic, elastic and certain forms of anelastic media. This important property is referred to as "model-type independence" because the same algorithm may be applied to a large class of different Earth models to achieve the same seismic processing objective. It was shown by Weglein et al. (2003) that if a processing task can be achieved with a subseries algorithm without having to specify how the perturbation operator, $\mathbf{V}$, depends on Earth properties, then that algorithm is independent of Earth model type.

Although inverse series algorithms relieve us of requiring *a priori* knowledge about the subsurface, like all methods they are founded on a set of assumptions. Some of these assumptions are common to all wave-theoretic processing algorithms, e.g., they require adequate sampling and source/receiver aperture. Also common to many other algorithms, by adopting the strategy of task separation, it is important that tasks are completed in sequence. For example, the internal multiple attenuation algorithm must be applied after free surface multiples have been removed (or are not significant, e.g., for a shallow target in a very deep water environment). Initial analysis of the imaging series terms has considered only primary events in the input data implying that all multiples have been removed, i.e., tasks 1 and 2 have been completed. The impact of violating this assumption is discussed in Chapter 3.

An important prerequisite of all inverse scattering series algorithms is knowledge of the source wavelet. Methods for estimating the wavelet include field measurements (Ziolkowski, 1991) or direct estimations from the recorded data (e.g., Weglein et al., 2000; Guo, 2004). The free surface and internal multiple attenuation algorithms can be divided into two steps: (1) prediction of the multiples and (2) subtraction of the multiples from the data. It is the prediction step that involves non-linear operations of the data, derived from the second and higher order terms in the series. The subtraction step is, in principle, straightforward but, in practice, must be executed with care. If the source wavelet is not known, then the predicted multiples will be in error by factors of the unknown wavelet. Signal processing techniques are applied that can compensate for these amplitude and phase effects during the subtraction step (Verschuur et al., 1992; Carvalho and Weglein, 1994; Abma et al., 2002). The most widely adopted subtraction technique uses the minimum energy criterion, which designs a match filter to be applied to the predicted multiples so that, after subtraction from the data, the energy will be minimized.

The first task of free-surface multiple removal requires that the input data have the direct wave removed in order to compute the scattered field (usually this is achievable with a surgical mute). The derivation of the algorithm also requires that source and receiver ghosts are removed. While deghosting is in principle a simple process, in practice algorithms can be sensitive to the accuracy of the source and receiver depths. Recently, new approaches to deghosting have been proposed that avoid these particular stability issues (e.g., Weglein et al., 2002; Robertsson and Kragh, 2002; Zhang and Weglein, 2004b). Often the adaptive subtraction techniques are relied upon to correct for residual ghost effects as well as the unknown source wavelet.

The fact that the sources and receivers are assumed to reside in the reference medium means

that knowledge of the surface properties is required. In the case of marine exploration, water properties are, in general, adequately known. For land and ocean-bottom seismic experiments, this can add a level of complexity. Compared to most other current processing algorithms, inverse series algorithms carry additional, but achievable, prerequisites on data acquisition and *a priori* information at the surface, in exchange for little or no information about the subsurface. This is usually a welcome trade-off.

Inverse series algorithms can achieve processing objectives without the traditional requirement for *a priori* subsurface information because they are more inquisitive of the data. The non-linear property of these algorithms results in multiplicative communication between events in the measured data. For example, all deghosted primary, free surface multiple and internal multiple events in the data are used by the free surface multiple removal algorithm to predict the correct amplitude and times of all free surface multiples. The seismic processor is not required to identify or separate these subevents nor provide any information about the subsurface model. In essence, these algorithms require that the data get more involved in their own processing objectives, than do linear algorithms, which treat the data more passively. As such, inverse series algorithms *data-driven*.

For a comprehensive review of the inverse scattering series and its application to seismic exploration see Weglein et al. (2003).

3. A LEADING ORDER IMAGING SERIES FOR A LAYERED ACOUSTIC MEDIUM

Following Weglein et al. (2002), we isolate terms in the inverse series that are responsible for locating reflectors in a 1-D constant density acoustic medium. After computing three terms in the series, we recognize a pattern in the mathematical expressions for the leading order contributions to the imaging series. These terms correspond to inverse scattering diagrams with a particular geometric configuration. Recognizing this pattern allows us to write down a formula that will predict any term without having to explicitly and laboriously isolate it from the inverse series. By extension, we may then write the formula for a leading order imaging series.

A closed form of the leading order imaging series is shown to exist and is used to analyze the convergence properties of the series algorithm. The leading order imaging series converges for any finite contrast between actual and reference velocities, and for finite maximum frequency in the data. The rate of convergence is greater for lower maximum frequency, smaller contrasts between the actual and reference velocities, and for angles of incidence closer to normal.

The leading order imaging series is an approximation to the full depth imaging potential of the inverse series in that its coefficients are leading order in the data. The first term in the series images reflectors at the depths dictated by the reference velocity (chosen to be constant in this case) and the data's travel times. The remaining terms use the data's amplitudes and travel times as well as the reference velocity to shift the reflectors closer to their correct location in depth.

Analytic examples demonstrate that, for moderate contrasts between the actual and reference medium, the leading order imaging series significantly improves the predicted depths of the reflectors at precritical angles, effectively acting to flatten the image gathers. We derive a condition under which the leading order imaging series improves the predicted depth of a reflector over linear imaging with the velocity. The impact of internal multiples is analyzed.

1 A 3-D experiment over a laterally invariant acoustic medium

We consider a constant density acoustic medium with point sources and receivers located at $\vec{x}_s = (x_s, y_s, z_s)$ and $\vec{x}_g = (x_g, y_g, z_g)$, respectively. Wave propagation in this medium can be

characterized by the wave equation

$$\left(\nabla^2 + \frac{\omega^2}{c^2(z)}\right)\psi(\vec{x}\,|\vec{x}_s;\omega) = -A(\omega)\delta(\vec{x}-\vec{x}_s) \tag{3.1}$$

where ψ is the pressure field, A is the source wavelet, c is the propagation velocity and ω is the angular temporal frequency. The field point, $\vec{x} = (x, y, z)$ is any point inside or on the surface of the volume defined in Fig. 1.2. This derivation of the prestack leading order imaging series is restricted to a medium that varies only in the z direction. For the first steps in its generalization to a 2-D earth, see Liu et al. (2004). ψ_0 is the pressure wavefield due to the same source, A, in the reference medium which is chosen to be a wholespace with velocity, c_0:

$$\left(\nabla^2 + \frac{\omega^2}{c_0^2}\right)\psi_0(\vec{x}\,|\vec{x}_s;\omega) = -A(\omega)\delta(\vec{x}-\vec{x}_s). \tag{3.2}$$

From Eq. (2.5), the scattering potential is

$$V = k_0^2\alpha. \tag{3.3}$$

where $k_0 = \omega/c_0$ and α is the velocity perturbation, a dimensionless parameter that relates the actual velocity, c, to the constant reference velocity, c_0, such that

$$\frac{1}{c^2(z)} = \frac{1}{c_0^2}\left[1+\alpha\,(z)\right]. \tag{3.4}$$

For this acoustic problem, the goal of inversion is to solve for α which can be written as an infinite series (after Eq. 2.9):

$$\alpha = \alpha_1 + \alpha_2 + \alpha_3 + \ldots = \sum_{n=1}^{\infty}\alpha_n \tag{3.5}$$

where α_1, the first term in the series for α, is linearly related to the scattered field on the measurement surface, $(\Psi_s)_m = (\Psi - \Psi_0)_m = \psi_s(\vec{x}_g\,|\vec{x}_s\,;\omega)$. The second term, α_2, is quadratic in $(\Psi_s)_m$, the third term, α_3, is cubic and so on.

After using the inverse series (Eqs. 3.5 and 3.3 with 2.9a,b,...) to solve for α, we could then use Eq. (3.4) to solve for the unknown velocity, $c(z)$. However, the objective here is in fact not to solve for the medium parameters (in this case just c), but to solve directly for the *location* at which the perturbation, α, changes. This is the problem of imaging in a medium whose velocity is not known before or after the imaging procedure.

2 Isolation of a leading order imaging series

2.1 The first term, α_1, and its degree of freedom

The inverse scattering series takes the measured values of the scattered field as input. For a homogeneous reference medium that agrees with the actual medium above the measurement

surface, the reference wavefield, ψ_0, is simply the direct wave – the wave that travels directly from the source to the receiver. Therefore, to calculate $(\Psi_s)_m$, we need to subtract the direct wave from the measured total field, $(\Psi)_m$. Deconvolving the source wavelet, we define the data $D = (\Psi_s)_m/A$, and then D is related to α_1 by (see Eq. 2.9a)

$$D\left(\vec{x}_g|\vec{x}_s;\omega\right) = \int_{-\infty}^{+\infty} G_0\left(\vec{x}_g|\vec{x}';\omega\right) k_0^2 \alpha_1\left(z'\right) G_0\left(\vec{x}'|\vec{x}_s;\omega\right) d\vec{x}' \tag{3.6}$$

where G_0 is the causal Green function satisfying the wave equation in the reference medium (and is related to the reference wavefield by $G_0 = \psi_0/A$). The solution for α_1 in cylindrical coordinates is (see Appendix A)

$$\alpha_1(-2q_g) = 2\pi \frac{-4q_g^2}{k_0^2} e^{iq_g(z_g+z_s)} \int_0^{\infty} D(r;\omega) J_0(k_r r) r dr \tag{3.7}$$

where the vertical and horizontal wavenumbers, q_g and k_r, respectively, are related by

$$q_g = k_0 \sqrt{1 - \frac{k_r^2}{k_0^2}}. \tag{3.8}$$

$J_0(k_r r)$ is a zero order Bessel function of the first kind that arises due to the azimuthal symmetry and is

$$J_0(k_r r) = \frac{1}{2\pi} \int_0^{2\pi} e^{ik_r r cos\phi} d\phi. \tag{3.9}$$

Figure 3.1 illustrates the relationship between the horizontal cartesian offset coordinates (x, y) and the cylindrical coordinates (r, ϕ).

The fact that the solution for α_1 is over-determined is evident in Eq. (3.7): whereas α_1 is only a function of q_g, the right-hand side can be written as a function of two independent variables, e.g., (q_g, ω) or (k_r, ω). Inverse Fourier transforming both sides of Eq. (3.7) gives

$$\alpha_1(z) = -8 \int_{-\infty}^{+\infty} \frac{q_g^2}{k_0^2} e^{-iq_g(2z-(z_g+z_s))} \int_0^{\infty} D(r;\omega) J_0(k_r r) r dr dq_g. \tag{3.10}$$

Considering fixed angles of incidence, θ_0, leads to a number of different estimates of $\alpha_1(z)$. Fixing θ_0 is the same as fixing horizontal and vertical slownesses, p and ζ_0, respectively, where

$$p \doteq \frac{\sin\theta_0}{c_0} \text{ and } \zeta_0 \doteq \frac{\cos\theta_0}{c_0}.$$

Note that p and ζ_0 are functions of the constant reference velocity and, as such, may be referred to as *reference* slownesses. We have chosen to omit the subscript "0" after p for brevity and because, in a 1-D medium, horizontal slowness is constant in each layer. Keeping

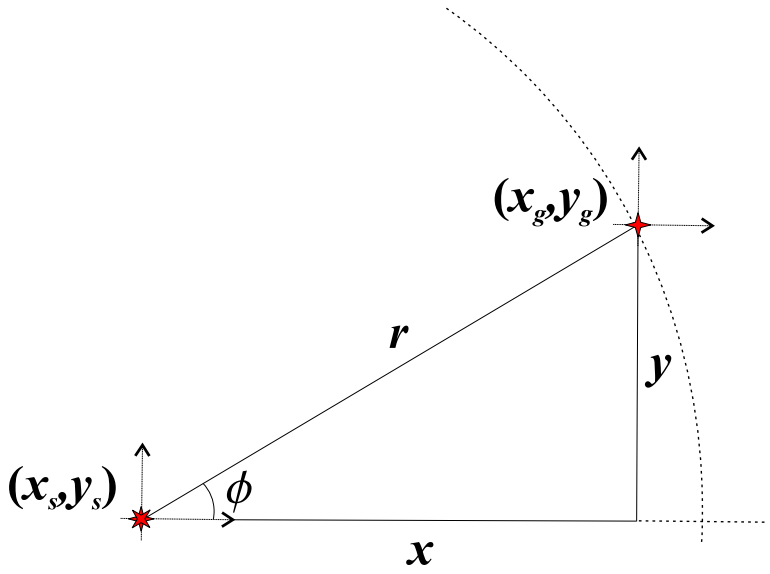

Fig. 3.1: Plan view showing the relationship between the horizontal cartesian and cylindrical coordinates. r is the source-receiver offset in the horizontal plane and ϕ is the azimuth. For a 1-D medium, the data are invariant in azimuth.

the subscript "0" after ζ highlights the fact that the inverse series terms are computed using only a (in this case constant) reference slowness whereas, in the inverse problem, the actual vertical slowness, $\zeta(z)$, is an unknown function of depth. With θ_0, p and ζ_0 fixed, q_g is still allowed to vary through the variation in ω since $q_g = \omega\zeta_0$. Therefore, to perform that integral, we proceed by changing variables from q_g to ω (and substituting $k_r = \omega p$):

$$\alpha_1(z,p) = -\,8\zeta_0 \cos^2\theta_0 \int_{-\infty}^{+\infty} e^{-i\omega\zeta_0(2z-(z_g+z_s))} \int_0^{\infty} D(r;\omega) J_0(\omega p r) r\,dr\,d\omega. \tag{3.11}$$

By considering fixed θ_0 we were able to move $q_g^2/k_0^2 = \cos^2\theta_0$ outside of the integral. Then $\alpha_1(z,p)$ denotes estimates of α_1 for fixed p values which, for a 1-D medium, describes fixed angles (θ_0) at which the constituent plane waves leave the source and arrive at the receivers. Defining the vertical time $\tau \doteq \zeta_0\,(2z - (z_g + z_s))$ and performing the inverse temporal Fourier transform of the data $D(r;\omega)$, Eq. (3.11) becomes

$$\alpha_1(\tau,p) = -\,8\zeta_0 \cos^2\theta_0 \int_0^{2\pi} \int_0^{\infty} D(r;\tau - pr\cos\phi) r\,dr\,d\phi. \tag{3.12}$$

Changing back to cartesian coordinates yields

$$\alpha_1(\tau,p) = -\,8\zeta_0 \cos^2\theta_0 \int_{-\infty}^{+\infty} \int_{-\infty}^{+\infty} D(x,y;\tau - px)\,dx\,dy \tag{3.13}$$

which is recognizable as a scaled slant stack of the recorded data (see, e.g., Treitel et al., 1982). Both Eqs. (3.12) and (3.13) are derived in Appendix A. In cartesian coordinates, the solution for α_1 requires sums in the x and y directions, whereas in cylindrical coordinates, as a result of the symmetry of a laterally invariant medium, these integrals are replaceable by integrals over ϕ and r (Eq. 3.12) or ω and r (Eq. 3.11).

An alternative approach to handling the degree of freedom in Eq. (3.10) is to hold ω fixed and integrate over angle, θ_0, or vertical slowness $\zeta_0 = \cos\theta_0/c_0 = q_g/\omega$. This parameterization will result in different estimates of α_1 for constant ω values (see also the discussion in Chapter 4).

2.2 Task separation in the second term

The integral equation for the second term in the inverse series for this acoustic problem is (from Eq. 2.9b)

$$\int_{-\infty}^{+\infty} G_0\left(\vec{x}_g|\vec{x}';\omega\right) k_0^2\alpha_2(z')G_0\left(\vec{x}'|\vec{x}_s;\omega\right) d\vec{x}' = \\ -\int_{-\infty}^{+\infty} d\vec{x}'\, G_0\left(\vec{x}_g|\vec{x}';\omega\right) k_0^2\alpha_1(z') \int_{-\infty}^{+\infty} d\vec{x}''\, G_0\left(\vec{x}'|\vec{x}'';\omega\right) k_0^2\alpha_1(z'')G_0\left(\vec{x}''|\vec{x}_s;\omega\right). \tag{3.14}$$

The solution is detailed in Appendix B where α_2 as a function of vertical wavenumber is shown to be separable into the sum of two parts (see Fig. 3.2):

$$\alpha_2(-2q_g) = \int_{-\infty}^{+\infty} dz' e^{2iq_g z'} \frac{k_0^2}{2q_g^2} \left(\alpha_1^2(z') + \int_0^{z'} dz'' \alpha_1(z'') \frac{d\alpha_1(z')}{dz'} \right). \tag{3.15}$$

As is the case for α_1, there is a degree of freedom in Eq. (3.15) that results in a choice of which variable to hold constant, and which to integrate over in the construction of $\alpha_2(z)$. For consistency, we choose to keep p constant, in which case performing the inverse Fourier transform of Eq. (3.15) gives

$$\alpha_2(z,p) = \frac{1}{2\cos^2\theta_0} \left(\alpha_1^2(z,p) + \left[\int_0^z \alpha_1(z',p)dz' \right] \frac{\partial\alpha_1(z,p)}{\partial z} \right). \tag{3.16}$$

The separation of the second term in the inverse series (Eq. 3.16) into the sum $\alpha_{21} + \alpha_{22}$ (defined below) is an example of task separation. As explained by Weglein et al. (2002) for the normal incidence case, these two terms have distinctly different roles in the inversion for α. The first piece

$$\alpha_{21}(z,p) = \frac{1}{2\cos^2\theta_0}\alpha_1^2(z,p) \tag{3.17}$$

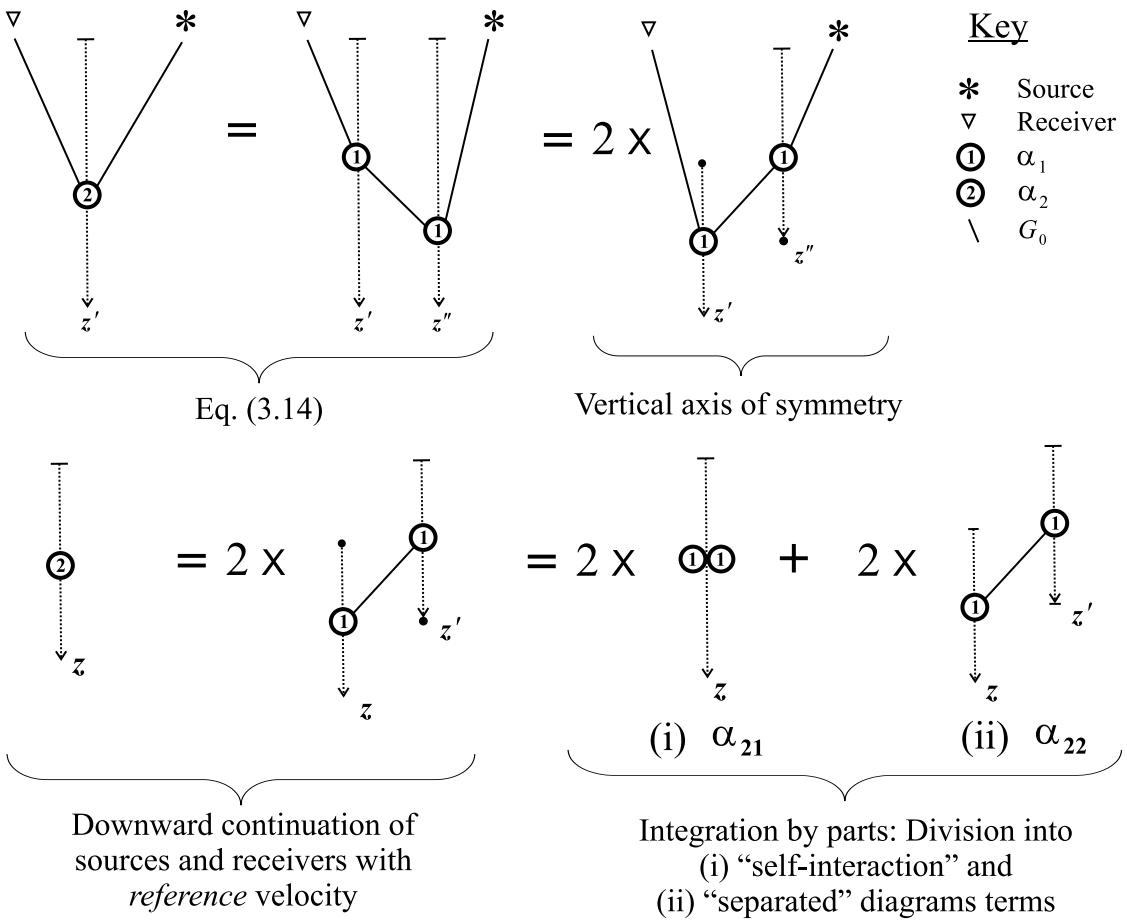

Fig. 3.2: *Diagrammatic representation of the solution for α_2 given in Appendix B. The second term has been divided into "self-interaction" and "separated" diagram contributions. The "•" symbol is used to illustrate that "self-interaction" is admitted, whereas the "–" signifies that "self-interaction" is excluded.*

is the portion of α_2 that acts to correct the amplitude (and *only* the amplitude) of α_1 towards α whereas the second piece

$$\alpha_{22}(z,p) = \frac{1}{2\cos^2\theta_0}\left[\int_0^z \alpha_1(z',p)dz'\right]\frac{\partial\alpha_1(z,p)}{\partial z} \tag{3.18}$$

is the first non-linear term in the subseries that shifts the mislocated interfaces in α_1 closer to their true depths. We can justify the assertion that α_{22} is an imaging-related term by considering a situation where the reference velocity agrees with the actual velocity model down to a single reflector, in which case the first term, α_1, should correctly locate the reflector and hence the problem of imaging does not exist beyond the first term. In this case, we would expect the non-linear imaging terms to be zero[1]. For a single interface at depth z_a, with a

[1] Strictly speaking, the *sum* of all the non-linear imaging terms should be zero. For the sake of efficiency,

reflection coefficient, R_{01}, the data are (e.g., Ewing et al., 1957)

$$\begin{aligned} D(r;\omega) &= \frac{i\omega}{4\pi}\int_0^\infty \frac{R_{01}(p)}{\zeta_0} e^{i\omega\zeta_0(2z_a - z_s - z_g)} J_0(\omega p r) p dp \\ &= \frac{-1}{4\pi}\int_0^\infty \frac{R_{01}(k_r/\omega)}{i\omega\zeta_0} e^{i\omega\zeta_0(2z_a - z_s - z_g)} J_0(k_r r) k_r dk_r \end{aligned} \tag{3.19}$$

which we substitute into the formula for α_1 (Eq. 3.11):

$$\begin{aligned} \alpha_1(z,p) =& -8\zeta_0 \cos^2\theta_0 \int_{-\infty}^{+\infty} e^{-i\omega\zeta_0(2z - z_g - z_s)} \left(\frac{-1}{4\pi} \frac{R_{01}(p)}{i\omega\zeta_0} e^{i\omega\zeta_0(2z_a - z_s - z_g)} \right) d\omega \\ =& \frac{2}{\pi}\cos^2\theta_0 R_{01}(p) \int_{-\infty}^{+\infty} \left(\frac{e^{-2i\omega\zeta_0(z - z_a)}}{i\omega} \right) d\omega \\ =& \frac{2}{\pi}\cos^2\theta_0 R_{01}(p)(-2\zeta_0) \int_{-\infty}^{z} dz' \int_{-\infty}^{+\infty} e^{-2i\omega\zeta_0(z' - z_a)} d\omega \\ =& \frac{2}{\pi}\cos^2\theta_0 R_{01}(p)(-2\zeta_0) \int_{-\infty}^{z} dz' \frac{2\pi\delta(z' - z_a)}{2\zeta_0} \\ =& -4\cos^2\theta_0 R_{01}(p) H(z - z_a). \end{aligned} \tag{3.20}$$

When the model consists of just a single reflector, and because the reference medium agrees with the actual medium above that reflector, then α_1 will correctly locate the interface at $z = z_a$. However, the inversion for α is still a non-linear problem that requires higher order terms in the series. Equation (3.20) is the first order approximation to the amplitude of $\alpha(z,p)$, which is derived algebraically in Appendix C for comparison.

Since the first term has predicted the correct depth of the reflector, we would expect that any and all portions of the inverse series beyond the first term that are responsible for *imaging* should vanish when presented with these data as input. Proceeding to the second term, Eq. (3.17) yields

$$\alpha_{21}(z,p) = 8\cos^2\theta_0 R_{01}^2(p) H(z - z_a) \tag{3.21}$$

which produces the second term in the series for the amplitude of α (compare with Eq. C.8). Meanwhile Eq. (3.18) for this example gives

$$\alpha_{22}(z,p) = 8\cos^2\theta_0 R_{01}^2(p) \underline{(z - z_a) H(z - z_a) \delta(z - z_a)} = 0. \tag{3.22}$$

The product $(z - z_a) \times \delta(z - z_a)$ is zero and so α_{22} is zero in this single interface example[2]. This result is an indication that α_{22} is an imaging term (i.e., associated with task 3) that

we hope that all individual non-linear imaging terms are zero and that the subseries doesn't compute non-zero terms that it subsequently erases. Fortunately, it turns out that when the first term is adequate, then all non-linear imaging terms are zero.

[2] The product of the Heaviside and delta functions is undefined at $z = z_a$ so how we evaluate α_{22} is important. In practice, for bandlimited data, there is no ambiguity. However, in this case, we could replace the upper limit of the integral in Eq. (3.18) with $z - \epsilon$, where ϵ is a small positive number, and let $\epsilon \to 0$ after integrating.

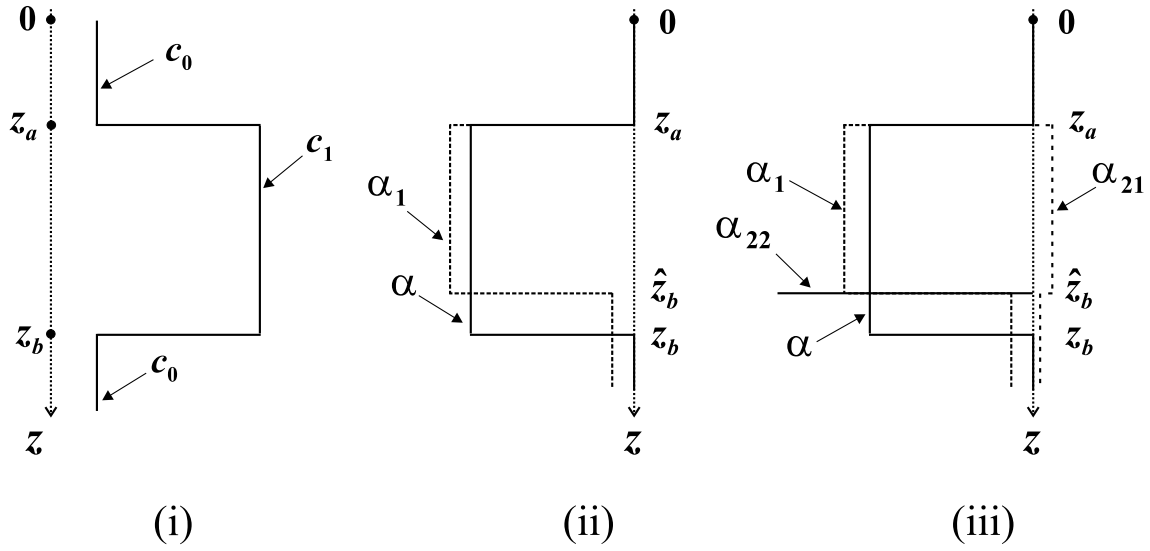

Fig. 3.3: *A two reflector example: (i) Velocity model; (ii) α and the first term in the series, α_1; (iii) The superposition of α_{21} and α_{22}. All inverse quantities are displayed for the same constant p.*

is concerned with correctly positioning the interfaces in α, whereas α_{21} is the parameter estimation term (task 4) that is concerned with solving for the correct amplitude of α between its interfaces.

To strengthen our argument that α_{22} is an imaging-related term, we imagine the simplest example in which a reflector is mislocated by the constant reference velocity and show, in that case, this term is non-zero. For a velocity profile $c_0 - c_1 - c_0$, where the two interfaces are located at z_a and z_b (see Fig. 3.3i), then ignoring internal multiples, the data consist of two primary reflections:

$$D(r;\omega) = \frac{i\omega}{4\pi}\int_0^\infty \frac{R_{01}(p) + \hat{R}_{12}(p)e^{i\omega\zeta_1 2z_b}}{\zeta_0} e^{i\omega\zeta_0(2z_a - z_s - z_g)} J_0(\omega pr) p dp \tag{3.23}$$

where $\hat{R}_{12}$ is the amplitude of the deeper primary event and ζ_1 is the vertical slowness in the layer. Following the same steps as before, we find[3]

$$\alpha_1(z,p) = -4\cos^2\theta_0 \left[R_{01}(p)H(z-z_a) + \hat{R}_{12}(p)H(z-\hat{z}_b)\right] \tag{3.24}$$

$$\alpha_{21}(z,p) = 8\cos^2\theta_0 \left[R_{01}^2(p)H(z-z_a) + \left(\hat{R}_{12}^2(p) + 2R_{01}(p)\hat{R}_{12}(p)\right)H(z-\hat{z}_b)\right] \tag{3.25}$$

$$\alpha_{22}(z,p) = 8\cos^2\theta_0 R_{01}(p)\hat{R}_{12}(p)(z-z_a)H(z-z_a)\delta(z-\hat{z}_b) \tag{3.26}$$

[3] We have made use of the identity $H^2(\cdot) \equiv H(\cdot)$ in Eq. (3.25).

as depicted in Fig. 3.3 where $\hat{z}_b$ is the incorrect depth at which the constant reference velocity images the deeper reflector:

$$\hat{z}_b = z_a + (z_b - z_a)\frac{\zeta_1}{\zeta_0}. \tag{3.27}$$

Although not explicitly noted in Eqs. (3.24–3.26), $\hat{z}_b$ is a function of the reference angle θ_0 or p. In conventional or current imaging, this is observed as residual moveout. We see that α_{22} in this example is definitely not zero. In fact, it is singular precisely at the mislocated interface depth $z = \hat{z}_b$.

In this section, we have separated the second term in the inverse series into two parts and shown that one of these parts exists (as a singular function) when there is a mislocated reflector but is zero when the reflector is correctly located. This piece of the second term, α_{22}, corresponds to a separated inverse scattering diagram. In the next section, we turn to the third term in the inverse series, isolate the imaging term that is analogous to α_{22} and postulate the form of an imaging subseries.

2.3 Task separation in the third term and a postulated imaging subseries

The solution for α_3 can be broken into several pieces, details of which are given in Appendix D. The separation, also discussed by Shaw et al. (2003) for the normal incidence case, corresponds to combinations of self-interaction and separated inverse scattering diagrams. The normal incidence analysis is straightforwardly generalizable to non-normal incidence (i.e., for prestack data) when the horizontal slowness, p, is held constant. In summary, we have

$$\alpha_3(z,p) = \alpha_{31}(z,p) + \alpha_{32}(z,p) + \alpha_{33}(z,p) + \alpha_{34}(z,p) + \alpha_{35}(z,p) \tag{3.28}$$

where

$$\begin{aligned}
\alpha_{31}(z,p) =& \frac{3}{16\cos^4\theta_0}\alpha_1^3(z,p) \\
\alpha_{32}(z,p) =& \frac{1}{8\cos^4\theta_0}\left[\int_0^z \alpha_1(z',p)dz'\right]^2 \frac{\partial^2\alpha_1(z,p)}{\partial z^2} \\
\alpha_{33}(z,p) =& \frac{-1}{8\cos^4\theta_0}\left[\int_0^z \alpha_1^2(z',p)dz'\right] \frac{\partial\alpha_1(z,p)}{\partial z} \\
\alpha_{34}(z,p) =& \frac{3}{4\cos^4\theta_0}\alpha_1(z)\left[\int_0^z \alpha_1(z',p)dz'\right] \frac{\partial\alpha_1(z,p)}{\partial z} \\
\alpha_{35}(z,p) =& \frac{-1}{16\cos^4\theta_0}\int_0^z\int_0^z \frac{\partial\alpha_1(z',p)}{\partial z'}\frac{\partial\alpha_1(z'',p)}{\partial z''}\alpha_1(z''+z'-z,p)dz'dz'' = \alpha_3^{\mathrm{IM}}(z,p)
\end{aligned}$$

The last term $\alpha_{35}(z,p)$ has been renamed $\alpha_3^{\mathrm{IM}}(z,p)$ in recognition of its role in the elimination of *internal multiples* which begins in the third term of the inverse series (Araújo, 1994).

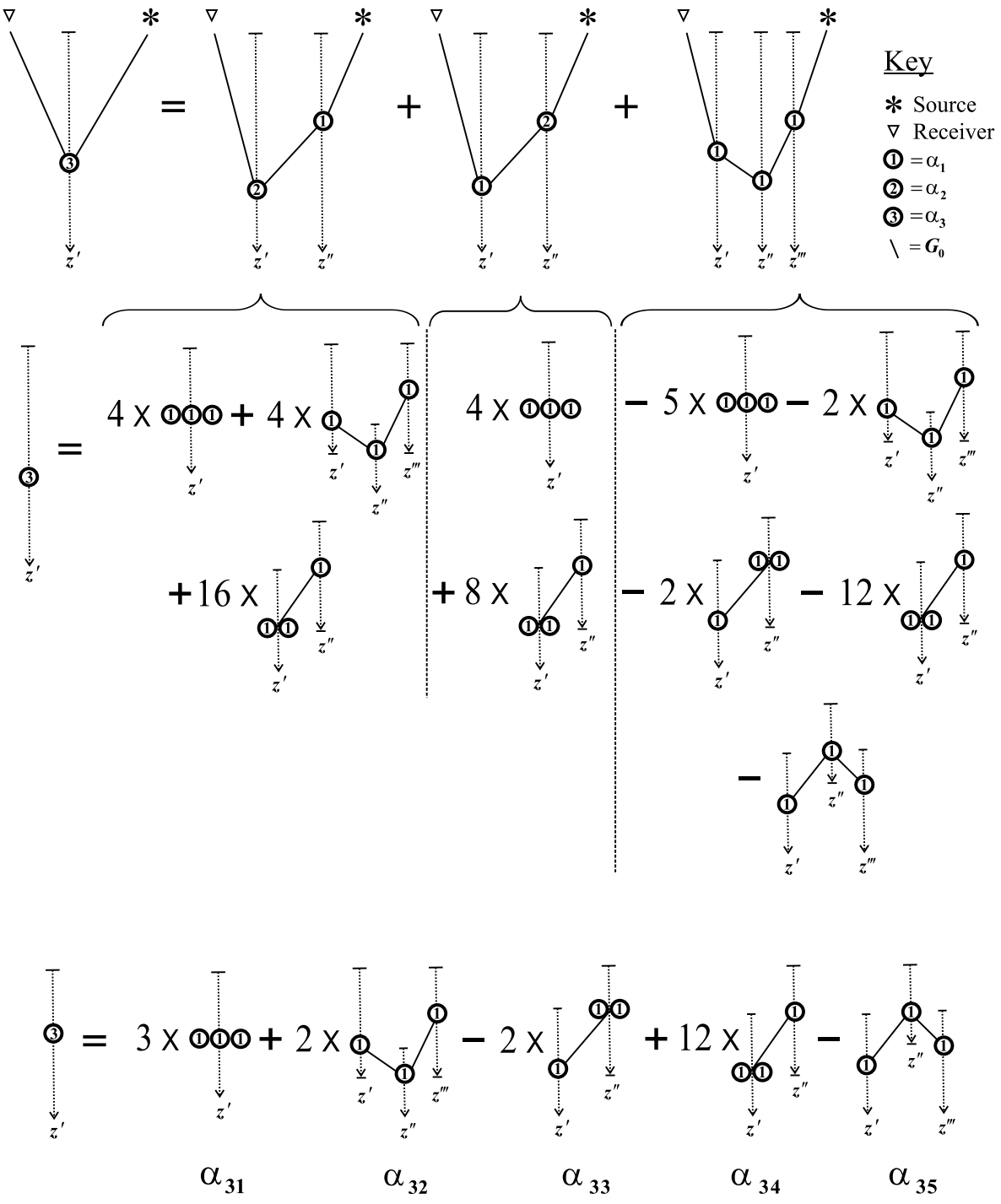

Fig. 3.4: Inverse scattering diagrams corresponding to the separation of terms in α_3. The mathematical derivations are provided in Appendix D.

Figure 3.4 illustrates diagrammatically the separation of terms in α_3. Notice the structural similarities between α_{21} and α_{31}: they correspond to purely self-interaction diagrams that are second and third order in the data, respectively. Considering again the single interface example introduced in the previous section (Eq. 3.20) where we found that

$$\alpha_{21}(z,p) = 8\cos^2\theta_0 R_{01}^2(p) H(z-z_a), \tag{3.29}$$

for the same example, we now have

$$\alpha_{31}(z,p) = -12\cos^2\theta_0 R_{01}^3(p) H(z-z_a) \tag{3.30}$$

which is recognizable as the third term in the series for the amplitude of α at a single interface (see Appendix C).

Notice also the similarities between terms α_{22} and α_{32}: they correspond to *purely* separated inverse scattering diagrams (i.e., they are void of any self-interaction component) and have a single reflection-like upward scattering point. Inspection of this second piece of the third term shows that, for a single interface,

$$\alpha_{32}(z,p) = -8\cos^2\theta_0 R_{01}^2(p)\hat{R}_{12}(p)\underline{(z-z_a)^2} H(z-z_a)\underline{\delta'(z-z_a)} = 0 \tag{3.31}$$

where δ' represents the derivative of the delta function with respect to z. We see that when the first term has correctly located the reflector, then $\alpha_{32} = 0$, just as with α_{22} (Eq. 3.22). This analysis suggests that α_{22} and α_{32} are both imaging-related terms because they "disappear" when the reference velocity has correctly located the reflector. Similar arguments can be made for the remaining terms in α_3, but for now we focus on the specific role that α_{22} and α_{32} play in imaging reflectors that have been mislocated in α_1.

Weglein et al. (2001) showed that the task of locating reflectors is accomplished through a Taylor series expanded about each mislocated reflector in α_1. The Taylor series for a Heaviside function $f(z) = H(z-z_b)$ expanded about $\hat{z}_b$ may be written

$$\begin{aligned} f(z) &= \sum_{n=0}^{\infty} \frac{(z_b-\hat{z}_b)^n}{n!} \left.\frac{\partial^n f(z)}{\partial z^n}\right|_{z=\hat{z}_b} \\ &= f(z)|_{z=\hat{z}_b} + (z_b-\hat{z}_b)\left.\frac{\partial f(z)}{\partial z}\right|_{z=\hat{z}_b} + \frac{(z_b-\hat{z}_b)^2}{2}\left.\frac{\partial^2 f(z)}{\partial z^2}\right|_{z=\hat{z}_b} + \dots \\ &= H(z-\hat{z}_b) + (z_b-\hat{z}_b)\delta(z-\hat{z}_b) + \frac{(z_b-\hat{z}_b)^2}{2}\delta'(z-\hat{z}_b) + \dots \end{aligned} \tag{3.32}$$

This equation demonstrates how an interface can be constructed at the correct depth, z_b, through a sum of singular functions centered at the incorrect depth, $\hat{z}_b$, and suggests a role for the delta function and its derivative in Eqs. (3.26) and (3.31), respectively. Notice that the coefficients in the Taylor series in Eq. (3.32) are functions of the actual depth, z_b, which is unknown in the inverse problem. From the formula for the reflection coefficient at an interface (Eq. C.3), we know that

$$\frac{\zeta_0}{\zeta_1} = \frac{1+R_{01}(p)}{1-R_{01}(p)} = 1 + 2R_{01}(p) + 2R_{01}^2(p) + 2R_{01}^3(p) + \dots \ , \ |R_{01}| < 1 \tag{3.33}$$

and combining Eq. (3.33) with Eq. (3.27), we have

$$(z_b - \hat{z}_b) = 2(\hat{z}_b - z_a)\left[R_{01}(p) + R_{01}^2(p) + R_{01}^3(p) + \ldots\right] \ , |R_{01}| < 1 \tag{3.34}$$

which illustrates that we can write the shift of the deeper reflector from the wrong depth to its correct depth as an infinite series in the angle-dependent reflection coefficient at the shallower reflector. Substituting this expression into the Taylor series (Eq. 3.32) produces

$$\begin{aligned} H(z - z_b) =& H(z - \hat{z}_b) + 2(\hat{z}_b - z_a)[R_{01}(p) + R_{01}^2(p) + \ldots]\delta(z - \hat{z}_b) \\ &+ 2(\hat{z}_b - z_a)^2[R_{01}^2(p) + 2R_{01}^3(p) + \ldots]\delta'(z - \hat{z}_b) \\ &+ \ldots \end{aligned} \tag{3.35}$$

Equation (3.35) demonstrates how the interface at the unknown depth, z_b, can be predicted through an infinite series in the amplitude of the shallower reflector and the pseudo-depths of both reflectors (z_a and $\hat{z}_b$) given by the reference velocity. This is a *cascaded* series in that the coefficients of the Taylor series are themselves geometric series.

We return to the two-reflector example discussed in the last section (Eqs. 3.23–3.26). Now we have,

$$\alpha_{32}(z, p) = -8\cos^2\theta_0 R_{01}^2(p)\hat{R}_{12}(p)(z - z_a)^2 H(z - z_a)\delta'(z - \hat{z}_b). \tag{3.36}$$

Summing the three terms that we have hypothesized play a role in imaging, we find

$$\begin{aligned} &\alpha_1(z, p) + \alpha_{22}(z, p) + \alpha_{32}(z, p) \\ &\quad = -4\cos^2\theta_0 \Big[R_{01}(p)H(z - z_a) + \hat{R}_{12}(p)\Big\{\underline{H(z - \hat{z}_b)} + \underline{2(\hat{z}_b - z_a)R_{01}(p)\delta(z - \hat{z}_b)} \\ &\qquad\qquad + \underline{2(\hat{z}_b - z_a)^2 R_{01}^2(p)\delta'(z - \hat{z}_b)}\Big\}\Big] \end{aligned} \tag{3.37}$$

where the underlined terms are seen to be a reproduction of the first three terms in the Taylor series of Eq. (3.35) to *leading order* in R_{01}. From this analysis, it appears that the sum $\alpha_1 + \alpha_{22} + \alpha_{32}$ are leading order approximations to the series that shifts the mislocated deeper reflector towards its true depth. Therefore, we infer that the leading order imaging series (LOIS) is

$$\begin{aligned} \alpha^{\text{LOIS}}(z, p) =& \alpha_1(z, p) + \alpha_{22}(z, p) + \alpha_{32}(z, p) + \ldots \\ =& \alpha_1(z, p) + \frac{1}{2\cos^2\theta_0}\left[\int_0^z \alpha_1(z', p)dz'\right]\frac{\partial\alpha_1(z, p)}{\partial z} \\ &+ \frac{1}{8\cos^4\theta_0}\left[\int_0^z \alpha_1(z', p)dz'\right]^2\frac{\partial^2\alpha_1(z, p)}{\partial z^2} + \ldots \\ =& \sum_{n=0}^{\infty}\frac{(1/2)^n}{n!\cos^{2n}\theta_0}\left[\int_0^z \alpha_1(z', p)dz'\right]^n\frac{\partial^n\alpha_1(z, p)}{\partial z^n} \end{aligned} \tag{3.38}$$

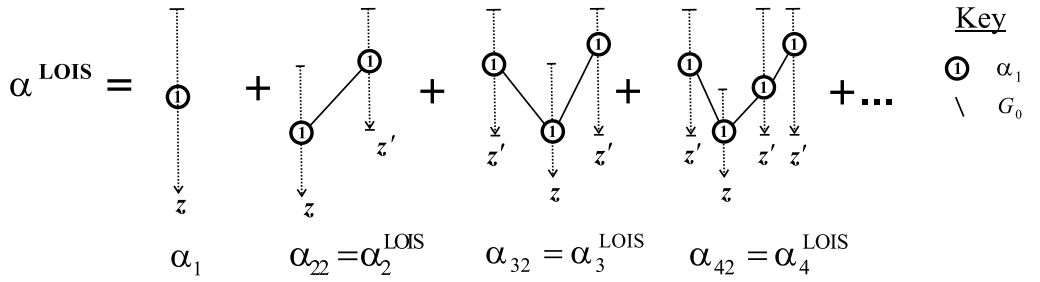

Fig. 3.5: *Inverse scattering diagrams corresponding to leading order imaging contributions from the first three terms of the inverse series.*

where $\alpha_1(z,p)$ is given by Eq. (3.11). The conjecture that Eq. (3.38) is a leading order imaging series is based on: (a) that it correctly predicts the inverse series terms α_1, α_{22} and α_{32} which have been found to mirror an imaging Taylor series for a known analytic example. The non-linear terms mirror the pattern of separated diagrams that have a single reflection-like scattering point at their deepest position (see Fig. 3.5); and (b) that it also correctly predicts the leading order contributions to the Taylor series in Eq. (3.35) up to *and beyond* the third term, for that analytic example. Any term in this series may be calculated using the formula

$$\alpha_{n+1}^{\text{LOIS}}(z,p) = \frac{(1/2)^n}{n!\cos^{2n}\theta_0}\left[\int_0^z \alpha_1(z',p)dz'\right]^n \frac{\partial^n \alpha_1(z,p)}{\partial z^n}\ ,\ n=0,1,2,\ldots \tag{3.39}$$

Analysis of the second term in the series gave us clues as to which terms are responsible for imaging, and which terms were concerned with amplitude inversion. We found that the self-interaction diagram contribution affected only amplitude inversion, whereas the separated diagram contribution appeared to play a role in imaging. These lessons were carried through to the third term in the series where it was found that the separated diagram term with a single reflection-like scattering point produced a very similar mathematical expression to its analogue in the second term. The evaluation of these terms for an analytic example lead to the conclusion that these separated diagram terms constitute the leading order approximations to the imaging series.

3 A closed form of the leading order imaging series and an analysis of convergence properties

If we substitute the Fourier transform

$$\frac{\partial^n \alpha_1(z,p)}{\partial z^n} = \frac{1}{2\pi}\int_{-\infty}^{+\infty}(ik_z)^n \alpha_1(k_z,p)e^{ik_z z}dk_z$$

into Eq. (3.38), where k_z is the Fourier conjugate variable to z, we have

$$\alpha^{\text{LOIS}}(z,p) = \frac{1}{2\pi}\int_{-\infty}^{+\infty}\alpha_1(k_z,p)\sum_{n=0}^{\infty}\frac{1}{n!}\left[\frac{ik_z}{2\cos^2\theta_0}\int_0^z\alpha_1(z',p)dz'\right]^n e^{ik_z z}dk_z \tag{3.40}$$

$$= \frac{1}{2\pi}\int_{-\infty}^{+\infty}\alpha_1(k_z,p)e^{ik_z\left(z+\left[\frac{1}{2\cos^2\theta_0}\int_0^z\alpha_1(z',p)dz'\right]\right)}dk_z. \tag{3.41}$$

The power series

$$\sum_{n=0}^{\infty}\frac{1}{n!}\left[\frac{ik_z}{2\cos^2\theta_0}\int_0^z\alpha_1(z',p)dz'\right]^n = \exp\left[-ik_z/(2\cos^2\theta_0)\int_0^z\alpha_1(z',p)dz'\right] \tag{3.42}$$

is recognized in Eq. (3.40) to arrive at Eq. (3.41). Now substitute

$$\alpha_1(k_z,p) = \int_{-\infty}^{+\infty}\alpha_1(z'',p)e^{-ik_z z''}dz''$$

into Eq. (3.41):

$$\begin{aligned}\alpha^{\text{LOIS}}(z,p) =& \frac{1}{2\pi}\int_{-\infty}^{+\infty}dz''\alpha_1(z'',p)\int_{-\infty}^{+\infty}dk_z e^{ik_z\left(z-z''+\left[\frac{1}{2\cos^2\theta_0}\int_0^z\alpha_1(z',p)dz'\right]\right)}\\ =& \frac{1}{2\pi}\int_{-\infty}^{+\infty}dz''\alpha_1(z'',p)2\pi\delta\left(z-z''+\left[\frac{1}{2\cos^2\theta_0}\int_0^z\alpha_1(z',p)dz'\right]\right)\\ =& \alpha_1\left(z+\Delta,p\right)\end{aligned} \tag{3.43}$$

where

$$\Delta(z) = \frac{1}{2\cos^2\theta_0}\int_0^z\alpha_1(z',p)dz'. \tag{3.44}$$

This closed form of the leading order imaging series and was first derived by Keys (2002) for the normal incidence case. The prestack leading order imaging series for a point source in a laterally invariant acoustic medium can be implemented by slant-stacking (or τ-p transforming) the data, weighting each p trace by the factor $-8\zeta_0\cos^2\theta_0$, and then operating on each trace with the formula provided in Eq. (3.43). When $p = 0$, Eqs. (3.38) and (3.43) reduce to the normal incidence algorithms given by Shaw et al. (2003)[4]. The leading order imaging series can be visualized as a squeeze/stretch of the data "conventionally imaged" with the reference velocity. As such, it has the flavor of a residual migration in that it is improving the location of reflectors that were mislocated by the reference velocity in the first term.

Besides the fact that it efficiently encapsulates an infinite number of terms through a straightforward manipulation of the depth variable in the first term, the closed form also allows us to study the convergence properties of the leading order imaging series. Since we have seen that the power series for e^x (Eq. 3.42) is the engine behind the leading order imaging series, we can conclude the following:

[4] The alternate definition of α in Shaw et al. (2003) produces a minus sign difference.

1. Conditions for convergence:
   (a) Finite $\int_0^z \alpha_1(z')dz'$. For finite contrasts between the actual and reference velocities, and because we are integrating to a finite depth, z, then this condition will be satisfied.
   (b) Finite k_z. As long as the maximum frequency (ω) in the data is finite, then k_z will be finite. It is difficult to imagine when this condition will not be satisfied.
2. Rate of convergence:
   (a) The leading order imaging series converges faster for smaller values of the integral $\int_0^z \alpha_1(z')dz'$. This indicates that a reference velocity closer to the actual velocity will improve the rate of convergence. In particular, the series cares about the cumulative error in the velocity down to the output point, z.
   (b) Smaller values of k_z will aid the rate of convergence. In practice, this implies that a higher resolution image will take longer to converge.
   (c) It will converge faster for small incident angles, θ_0. This is the angle at the surface, not the angle at depth although the two are related via Snell's Law to the velocity model. It should be noted that $k_z \sim \frac{\omega}{c_0}\cos\theta_0$ which means that the net dependence is proportional to $1/\cos\theta_0$ rather than $1/\cos^2\theta_0$.

As long as the convergence criteria hold, we can use the closed form of the leading order imaging series in which case the rate of convergence is of little consequence.

4 Evaluation of the leading order imaging series shift

Consider a reflector that is located at depth z_R. It is imaged at depth $\hat{z}_R$ by the constant reference velocity and at depth $\hat{z}_R^{\text{LOIS}}$ by the leading order imaging series (see Fig. 3.6). We would like to know how good an approximation $\hat{z}_R^{\text{LOIS}}$ is to z_R and, more importantly, whether $\hat{z}_R^{\text{LOIS}}$ is an improvement over $\hat{z}_R$. From the travel time equation, the two-way vertical time to this reflector is

$$\tau(z_R) = 2\int_0^{z_R} \zeta(z')dz' \tag{3.45}$$

where, for simplicity, we assume that the sources and receivers are located at $z_s = z_g = 0$. Linear imaging with the constant reference velocity will predict its depth at

$$\begin{aligned}\hat{z}_R =& \frac{\tau(z_R)}{2\zeta_0} \\ =& \frac{1}{\zeta_0}\int_0^{z_R} \zeta(z')dz'.\end{aligned} \tag{3.46}$$

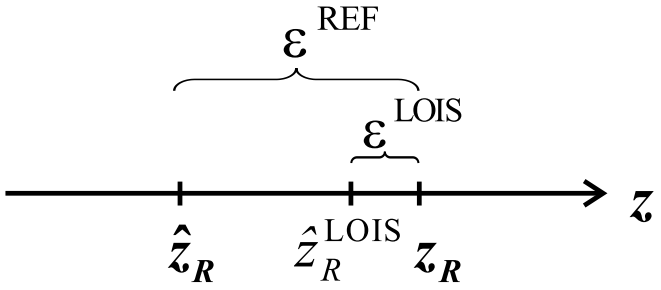

Fig. 3.6: *Errors in the predicted depths. z_R is a reflector's true depth, $\hat{z}_R$ is the depth predicted by the reference velocity in the first term, and $\hat{z}_R^{LOIS}$ is the depth predicted by the leading order imaging series.*

This is its position in α_1. Only if the actual slowness happens to be ζ_0, will $\hat{z}_R = z_R$. Given the information in α_1, the leading order imaging series will reposition the reflector at

$$\hat{z}_R^{\mathrm{LOIS}} = \hat{z}_R - \frac{1}{2\cos^2\theta_0}\int_0^{\hat{z}_R} \alpha_1(z')dz'. \tag{3.47}$$

We would like to know whether $\hat{z}_R^{\mathrm{LOIS}}$ is, in general, closer to z_R than $\hat{z}_R$ is, i.e., under what conditions the leading order imaging series is an improvement over current imaging methods that use an inadequate reference velocity. From the definition of α (Eq. 3.4),

$$\begin{aligned}\zeta(z) =& \zeta_0 \sqrt[+]{1+\alpha(z)} \\ =& \zeta_0\left(1+\frac{1}{2}\alpha(z)-\frac{1}{8}\alpha^2(z)+\ldots\right).\end{aligned} \tag{3.48}$$

If we substitute this equation into Eq. (3.46), we find that the error in the depth predicted by the first term is

$$\varepsilon^{\mathrm{REF}} = \hat{z}_R - z_R = \int_0^{z_R}\frac{\zeta(z')-\zeta_0}{\zeta_0}dz' = \int_0^{z_R}\left(\frac{1}{2}\alpha(z')-\frac{1}{8}\alpha^2(z')+\ldots\right)dz' \tag{3.49}$$

which, when substituted into Eq. (3.47), gives the error in the depth predicted by α^{LOIS} :

$$\varepsilon^{\mathrm{LOIS}} = \hat{z}_R^{\mathrm{LOIS}} - z_R = \int_0^{z_R}\left(\frac{1}{2}\alpha(z')-\frac{1}{8}\alpha^2(z')+\ldots\right)dz' - \frac{1}{2\cos^2\theta_0}\int_0^{\hat{z}_R}\alpha_1(z')dz'.$$

Both $\varepsilon^{\mathrm{REF}}$ and $\varepsilon^{\mathrm{LOIS}}$ will be smaller when the integral of α is smaller, which will be the case when the actual velocity model is closer to the chosen reference velocity. The leading order imaging series is an improvement over a linear imaging algorithm when

$$|\varepsilon^{\mathrm{LOIS}}| < |\varepsilon^{\mathrm{REF}}| \tag{3.50}$$

i.e., when

$$\left|\int_0^{z_R}\left(\frac{1}{2}\alpha(z')-\frac{1}{8}\alpha^2(z')+\ldots\right)dz'-\frac{1}{2\cos^2\theta_0}\int_0^{\hat{z}_R}\alpha_1(z')dz'\right| < \left|\int_0^{z_R}\left(\frac{1}{2}\alpha(z')-\frac{1}{8}\alpha^2(z')+\ldots\right)dz'\right|$$

or in terms of slownesses, this condition can be written (using Eq. 3.49)

$$\left|\int_0^{z_R}\frac{\zeta(z')-\zeta_0}{\zeta_0}dz'-\frac{1}{2\cos^2\theta_0}\int_0^{\hat{z}_R}\alpha_1(z')dz'\right| < \left|\int_0^{z_R}\frac{\zeta(z')-\zeta_0}{\zeta_0}dz'\right|.$$

We can rearrange this inequality via the following manipulations

$$\begin{aligned} |A-B| &< |A| \\ \left|A\left(1-\frac{B}{A}\right)\right| &< |A| \\ -1 < \left(1-\frac{B}{A}\right) &< 1 \\ 0 < \left(\frac{B}{A}\right) &< 2 \end{aligned} \tag{3.51}$$

where

$$A = \hat{z}_R - z_R = \varepsilon^{\mathrm{REF}} \text{ (see Eq. 3.49)}$$
$$\text{and } B = \hat{z}_R - \hat{z}_R^{\mathrm{LOIS}} = \frac{1}{2\cos^2\theta_0}\int_0^{\hat{z}_R}\alpha_1(z')dz'.$$

If the condition in Eq. (3.51) can be satisfied, then the leading order imaging series will predict a depth that is more accurate than current imaging with the reference velocity. For the simple example of two reflectors, we can show that the condition will be satisfied. We consider a two-reflector model where the vertical slowness profile is (see Fig. 3.7)

$$\zeta(z) = \zeta_0(z) + (\zeta_1-\zeta_0)H(z-z_a) + [\zeta_2-(\zeta_1-\zeta_0)]\,H(z-z_b).$$

Then for this example

$$\begin{aligned} A &= \int_0^{z_b}\left(\frac{\zeta(z')-\zeta_0}{\zeta_0}\right)dz' = \frac{\zeta_1-\zeta_0}{\zeta_0}(z_b-z_a) \\ B &= \frac{1}{2\cos^2\theta_0}\int_0^{\hat{z}_b}\alpha_1(z')dz' = \frac{1}{2\cos^2\theta_0}\left(-4\cos^2\theta_0\frac{\zeta_0-\zeta_1}{\zeta_0+\zeta_1}(\hat{z}_b-z_a)\right) \\ &= -2\left(\frac{\zeta_1}{\zeta_0}\frac{(\zeta_0-\zeta_1)}{(\zeta_0+\zeta_1)}(z_b-z_a)\right) \end{aligned}$$

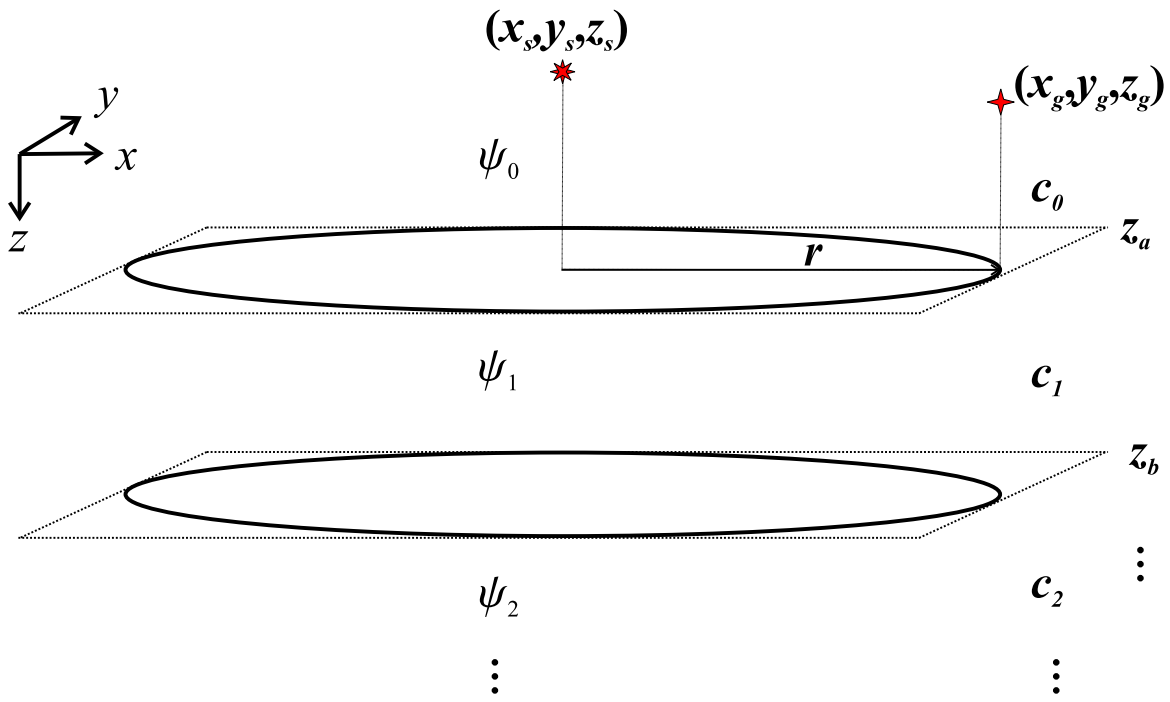

Fig. 3.7: *A multi-layer 1-D constant density acoustic model. In the absence of a free surface, all reflected waves at the receiver are upgoing.*

which, upon substitution into Eq. (3.51), gives

$$0 < \frac{2\zeta_1}{\zeta_0 + \zeta_1} < 2.$$

This result tells us that the downgoing transmission coefficient at the upper interface satisfies the condition necessary to show that the leading order imaging series improves the predicted depth of the second interface *independent* of (a) the depths of the two interfaces, or (b) the actual velocity below the first interface.

5 More analytic examples

5.1 Analytic examples with three interfaces

Analysis of the imaging subseries becomes more interesting for three or more reflectors because of the effect of transmission loss in the overburden. Consider a model that consists of three horizontal interfaces at depths z_a, z_b and z_c and a discontinuous velocity profile $c(z)$ as depicted in Fig. 3.7. The wavefield in the upper halfspace, ψ_0, consists of an incident field, ψ_i, and a reflected field, ψ_r. The measured reflected wavefield can be derived by decomposing

the incident field into a sum of plane waves (the Sommerfeld integral) and then matching boundary conditions at each interface (see, e.g., Ewing et al., 1957; Aki and Richards, 2002). The result is

$$\psi_r(r;\omega) = \frac{i\omega}{4\pi}\int_0^\infty \frac{\left(R_{01} + \hat{R}_{12}e^{2i\omega\zeta_1(z_b-z_a)} + \hat{R}_{23}e^{2i\omega[\zeta_1(z_b-z_a)+\zeta_2(z_c-z_b)]} + \dots\right)}{\zeta_0} \times e^{i\omega\zeta_0(2z_a-z_s-z_g)}J_0(\omega pr)pdp \quad (3.52)$$

where the reflection and transmission coefficients are functions of angle and are given by

$$R_{jk} = \frac{\zeta_j - \zeta_k}{\zeta_j + \zeta_k} \qquad j = 0,1,2,3; k = j+1 \quad (3.53)$$

$$T_{jk} = 1 - \frac{\zeta_j - \zeta_k}{\zeta_j + \zeta_k} = 1 - R_{jk} \qquad j = 0,1,2,3; k = j+1. \quad (3.54)$$

We have further defined the amplitudes $\hat{R}_{12} = T_{01}R_{12}T_{10}$ and $\hat{R}_{23} = T_{01}T_{12}R_{23}T_{21}T_{10}$. The vertical slownesses are functions of the incident angles in each layer:

$$\zeta_j = \frac{\cos\theta_j}{c_j} \ , \ \ j = 0,1,2,\dots \quad (3.55)$$

The "+ . . ." in Eq. (3.52) are the internal multiple reflections in the data. For now, an internal multiple removal algorithm, a subseries that begins in the third term of the inverse series, is assumed to have been applied before the imaging subseries. This results in a new effective data and a new effective α_1 that contain only primary reflection events. This step is part of the strategy of inverse series task separation described by Weglein et al. (2003). For the two reflector examples studied earlier, the internal multiples were of no consequence since the imaging series only uses information recorded earlier than the primary event being imaged, which excluded the multiples. In the next section, we will study the effect of a residual first order internal multiple that arrives before the deepest primary being imaged.

Reverting to the symbol D for data that contain only primary reflections, and changing the integration variable from p to k_r, Eq. (3.52) becomes

$$D(r;\omega) = \int_0^\infty \frac{\left(R_{01} + \hat{R}_{12}e^{2i\omega\zeta_1(z_b-z_a)} + \hat{R}_{23}e^{2i\omega[\zeta_1(z_b-z_a)+\zeta_2(z_c-z_b)]}\right)}{-4\pi i\omega\zeta_0} \times e^{i\omega\zeta_0(2z_a-z_s-z_g)}J_0(k_r r)k_r dk_r. \quad (3.56)$$

Performing a linear inversion of the data (Eq. 3.11), the first term in the series for $\alpha(z)$ for

this three-reflector example can be written:

$$\begin{aligned}\alpha_1(z,p) =& -8\zeta_0\cos^2\theta_0\int_{-\infty}^{+\infty} e^{-i\omega\zeta_0(2z-(z_g+z_s))}\int_0^{\infty} D(r;\omega)J_0(k_r r)r\,dr\,d\omega \\ =& 8\cos^2\theta_0\int_{-\infty}^{+\infty}\frac{R_{01}+\hat{R}_{12}e^{2i\omega\zeta_1(z_b-z_a)}+\hat{R}_{23}e^{2i\omega[\zeta_1(z_b-z_a)+\zeta_2(z_c-z_b)]}}{4\pi i\omega\zeta_0}e^{-2i\omega\zeta_0(z-z_a)}d\omega \\ =& -4\cos^2\theta_0\Big[R_{01}H\left(z-z_a\right)+\left(R_{01}+\hat{R}_{12}\right)H\left(z-\hat{z}_b\right) \\ &+\left(R_{01}+\hat{R}_{12}+\hat{R}_{23}\right)H\left(z-\hat{z}_c\right)\Big] \quad (3.57)\end{aligned}$$

where the dependence of both the amplitudes *and* the predicted depths on p is implicit. The shallowest reflector is correctly located at z_a (since the velocity down to z_a was correct) but the deeper reflectors are mislocated at depths

$$\hat{z}_b = z_a + (z_b - z_a)\frac{\zeta_1}{\zeta_0} \quad (3.58)$$

$$\text{and } \hat{z}_c = \hat{z}_b + (z_c - z_b)\frac{\zeta_2}{\zeta_0}. \quad (3.59)$$

Inserting Eq. (3.57) into the leading order imaging series will result in a shift of the two mislocated interfaces to depths

$$\hat{z}_b^{\text{LOIS}} = \hat{z}_b + 2(\hat{z}_b - z_a)R_{01} \quad (3.60)$$

$$\hat{z}_c^{\text{LOIS}} = \hat{z}_c + 2(\hat{z}_b - z_a)R_{01} + 2(\hat{z}_c - \hat{z}_b)(R_{01}+\hat{R}_{12}). \quad (3.61)$$

We have already seen that Eq. (3.60) is the approximation to z_b that is leading order in R_{01} (see Eq. 3.34). We can show that Eq. (3.61) is the approximation to z_c that is leading order in the amplitudes of the scattered field. Equations (3.58) and (3.59) can be combined to give

$$z_c = z_a + (\hat{z}_b - z_a)\frac{\zeta_0}{\zeta_1} + (\hat{z}_c - \hat{z}_b)\frac{\zeta_0}{\zeta_2} \quad (3.62)$$

and then the slowness ratios can be expanded as series in the reflection coefficients where (see also Eq. 3.33)

$$\begin{aligned}\frac{\zeta_0}{\zeta_1} &= \frac{1+R_{01}}{1-R_{01}} = 1 + 2R_{01} + 2R_{01}^2 + 2R_{01}^3 + \ldots\ , |R_{01}| < 1 \\ \frac{\zeta_0}{\zeta_2} &= \left(\frac{1+R_{01}}{1-R_{01}}\right)\left(\frac{1+R_{12}}{1-R_{12}}\right) \\ &= 1 + 2R_{01} + 2R_{12} + 2R_{01}^2 + 2R_{12}^2 + 4R_{01}R_{12} + \ldots\ , |R_{01}| < 1, |R_{12}| < 1. \quad (3.63)\end{aligned}$$

Substituting these expressions into Eq. (3.62) gives

$$\begin{aligned}z_c = \hat{z}_c &+ 2\left(\hat{z}_b - z_a\right)\left[R_{01} + R_{01}^2 + R_{01}^3 + \ldots\right] \\ &+ 2\left(\hat{z}_c - \hat{z}_b\right)\left[R_{01} + R_{12} + R_{01}^2 + R_{12}^2 + 2R_{01}R_{12}\right. \\ &\left. + R_{01}^3 + R_{12}^3 + 2R_{01}R_{12}^2 + 2R_{01}^2R_{12} + \ldots\right] \quad (3.64)\end{aligned}$$

The shift calculated by the leading order imaging series (Eq. 3.61) is an approximation to the series in Eq. 3.64 to leading order in the data's amplitudes. The approximation reduces to

$$(\hat{z}_b - z_a)R_{01} + (\hat{z}_c - \hat{z}_b)(R_{01} + \hat{R}_{12}) \approx (\hat{z}_b - z_a)\left[R_{01} + R_{01}^2 + R_{01}^3 + \ldots\right] + (\hat{z}_c - \hat{z}_b)\left[R_{01} + R_{12} + R_{01}^2 + R_{12}^2 + 2R_{01}R_{12} + \ldots\right] \tag{3.65}$$

where we observe that leading order in the amplitudes of the scattered field, in general, implies non-linearity in the reflection coefficients:

$$\hat{R}_{12} = T_{01}R_{12}T_{10} = R_{12} + R_{01}^2 R_{12}. \tag{3.66}$$

The leading order approximation to the shift of the reflector at $\hat{z}_c$ contains contributions that are linear and cubic in the reflection coefficients. For deeper reflectors, these contributions will be of increasingly higher order due to the transmission coefficients in the measured scattered field. It is to be expected leading order approximation will deteriorate for deeper reflectors due to the fact that the shift is a function of approximations (truncated geometric series) at all shallower reflectors. Higher order imaging terms are expected to improve the approximation and will be explored in Chapter 5.

Figures 3.8 and 3.9 illustrate the results for two choices of model parameters given in Table 3.1. In the first example, the layer velocity $c_1 > c_0$ and in the second example, $c_1 < c_0$ by the same amount (roughly 13%). As a result, the first term in the series "under-corrects" the deeper reflectors in Fig. 3.8 and "over-corrects" them in Fig. 3.9. In both cases, the leading order imaging series (computed analytically) shifts the mislocated interfaces closer to their true depths. It is interesting to note that, in the second example, α^{LOIS} positions the reflectors a small distance *shallower* than their actual depths, whereas the first term placed them a much greater distance *deeper*. Therefore, the sign of the depth error can change. The leading order imaging series has the effect of flattening image gathers closer to their true depths than a current linear imaging algorithm using the reference velocity.

In the next section we will study the impact of violating the assumption that internal multiples have been removed.

	Layer velocities (m/sec)			Interface depths (m)		
	c_0	c_1	c_2	z_a	z_b	z_c
Fig. 3.8	1500	1700	1800	100	140	170
Fig. 3.9	1500	1300	1600	100	140	170

Tab. 3.1: Model parameters corresponding to the results in Figs. 3.8 and 3.9.

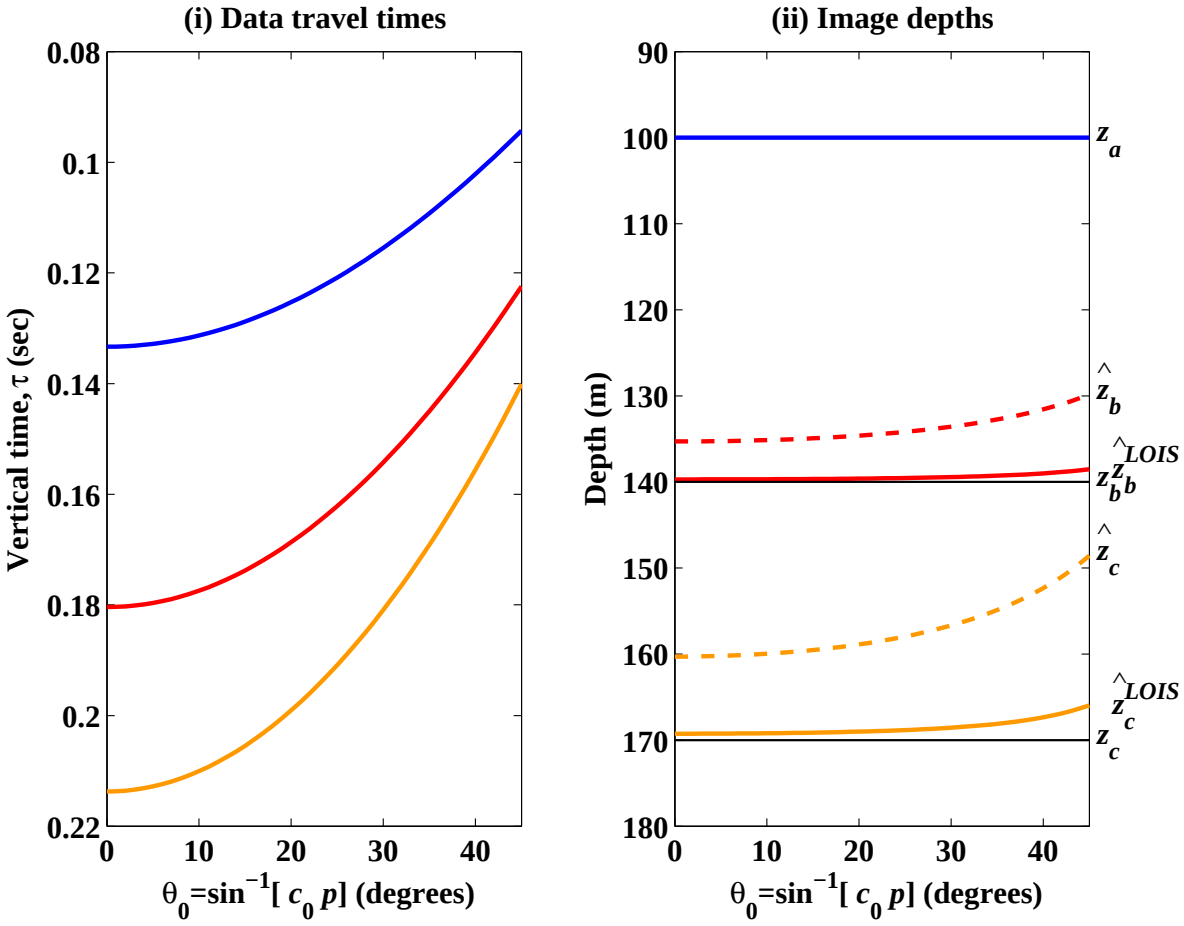

Fig. 3.8: (i) Travel time curves for three primaries. (ii) Depths predicted by the first term, z_a, $\hat{z}_b$ and $\hat{z}_c$, and the leading order imaging series, z_a, $\hat{z}_b^{LOIS}$ and $\hat{z}_c^{LOIS}$. Model parameters are given in Table 3.1.

5.2 The impact of internal multiples on the leading order imaging series

The strategy of isolating task-specific subseries of the inverse series that achieve important seismic processing objectives has proven to be a successful one (Weglein et al., 2003). As part of this strategy, subseries algorithms are applied in sequence using the output from a preceding algorithm as input to the current one. While progress is being made in extending the inverse scattering internal multiple attenuation algorithm (Weglein et al., 1997) towards an internal multiple removal algorithm (Ramirez and Weglein, 2005), the current high-water mark in multiple attenuation when the Earth model is unknown is that free surface multiples can be removed and internal multiples can be well-attenuated for a large class of models.

The scattered field that includes three primary reflectors and a first order internal multiple

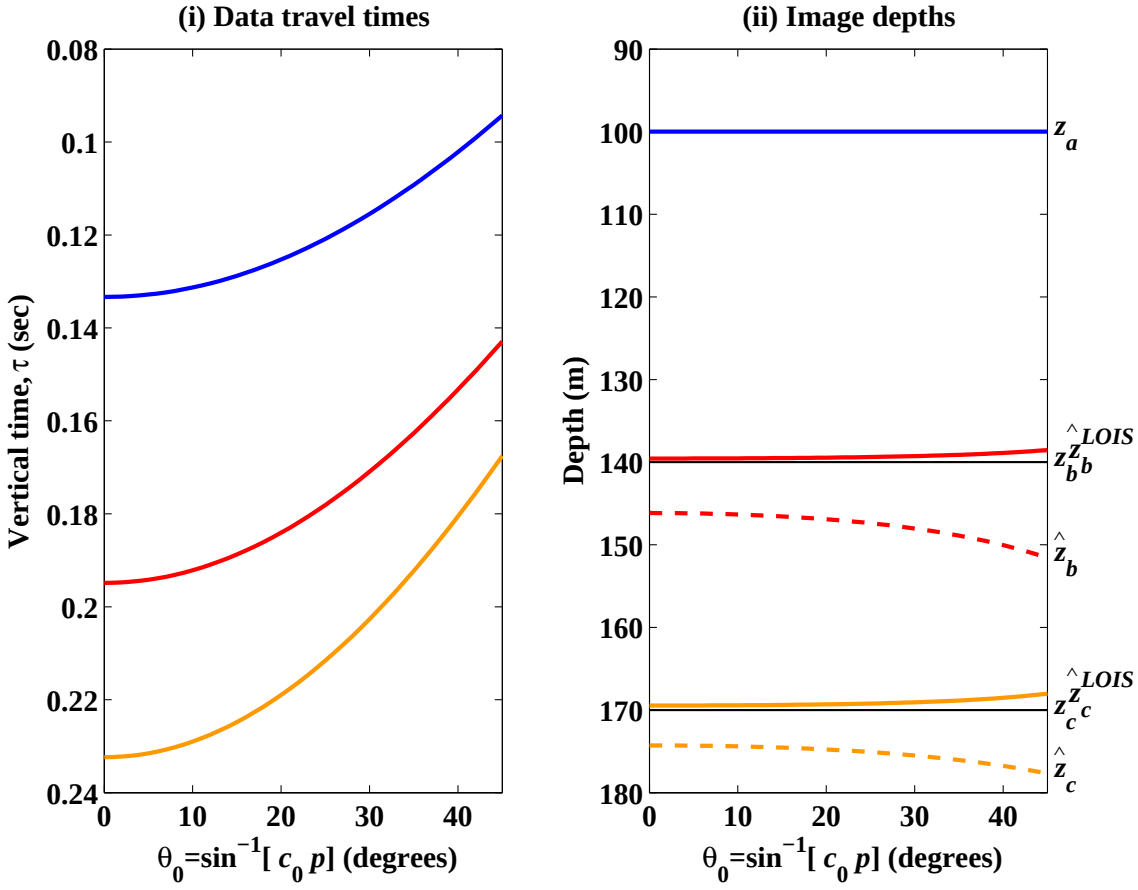

Fig. 3.9: (i) Travel time curves for three primaries. (ii) Depths predicted by the first term, z_a, $\hat{z}_b$ and $\hat{z}_c$, and the leading order imaging series, z_a, $\hat{z}_b^{LOIS}$ and $\hat{z}_c^{LOIS}$. Model parameters are given in Table 3.1.

that has reverberated in the first layer can be written analytically as

$$D(r;\omega) = \frac{i\omega}{4\pi}\int_0^\infty \left(\frac{R_{01} + \hat{R}_{12}e^{2i\omega\zeta_1(z_b-z_a)} + \hat{R}_{\rm IM}e^{4i\omega\zeta_1(z_b-z_a)}}{\zeta_0} + \frac{\hat{R}_{23}e^{2i\omega[\zeta_1(z_b-z_a)+\zeta_2(z_c-z_b)]}}{\zeta_0} \right) e^{i\omega\zeta_0(2z_a-z_s-z_g)} J_0(\omega pr) p dp. \quad (3.67)$$

The amplitude of the internal multiple is

$$\hat{R}_{\rm IM}(p) = T_{01}R_{12}R_{10}R_{12}T_{10} = -T_{01}R_{12}^2R_{01}T_{10} \quad (3.68)$$

which, after application of the inverse scattering internal multiple attenuation algorithm is reduced to (Weglein and Matson, 1998)

$$\hat{R}_{\rm IM}(p) = -T_{01}R_{12}^2R_{01}T_{10}(1 - T_{01}T_{10}) \quad (3.69)$$

For this example, the first term in the series is

$$\begin{aligned}\alpha_1(z,p) = &-4\cos^2\theta_0\Big[R_{01}H\left(z-z_a\right)+\left(R_{01}+\hat{R}_{12}\right)H\left(z-\hat{z}_b\right)\\ &+\left(R_{01}+\hat{R}_{12}+\hat{R}_{\mathrm{IM}}\right)H\left(z-\hat{z}_{\mathrm{IM}}\right)+\left(R_{01}+\hat{R}_{12}+\hat{R}_{\mathrm{IM}}+\hat{R}_{23}\right)H\left(z-\hat{z}_c\right)\Big]\end{aligned} \tag{3.70}$$

where $\hat{z}_{\mathrm{IM}}$ is the depth that the internal multiple is imaged at. The impact of residual multiples on the imaging series is two-fold. First, the multiples themselves will be imaged by the series and, second, they will impact the distance that events below them (or that arrive later in time) are shifted by the imaging series. In the following examples, we illustrate the latter effect only.

Figures 3.10 and 3.11 show the results of the leading order imaging series for the two specific models described in Table 3.2 and in the presence of a first order multiple that has reverberated between the interfaces at z_a and z_b.

	Layer velocities (m/sec)			Interface depths (m)		
	c_0	c_1	c_2	z_a	z_b	z_c
Fig. 3.10	1500	2000	1900	100	125	170
Fig. 3.11	1500	2000	2120	100	125	220

Tab. 3.2: Model parameters corresponding to the results in Figs. 3.10 and 3.11 in which the impact on the leading order imaging series of a first order internal multiple is analyzed.

It is interesting to note that in Fig. 3.10, the impact of the internal multiple is actually to improve the predicted depth of the reflector whereas in Fig. 3.11 the opposite is true. This implies that the effect of residual internal multiples on the leading order imaging series is not predictable without knowing the model, and therefore the strategy to remove multiples before applying this algorithm is a prudent one.

5.3 Further Discussion

The analytic results of the prestack leading order imaging series have highlighted a number of interesting characteristics of the algorithm. Given a choice of how to handle the degree of freedom afforded by the source-receiver offset in the seismic experiment, we chose to keep the angle of incidence in the reference medium (θ_0 or $p = p_0$) constant and let ω vary. This allowed for a straightforward generalization of the normal incidence case to non-normal incidence.

For the acoustic examples considered here, the first term in the imaging series more accurately locates reflectors at small incident angles. This is because the decomposed plane

waves at larger angles spend proportionally longer times in the layers with the wrong velocity. However, the magnitude of the amplitudes at larger angles is greater, which generally assists the non-linear terms of the leading order imaging series in shifting the reflectors the required distance to their actual locations. This larger "effective contrast" at higher angles (its AVA property) highlights the fact that the imaging subseries is leading order in the data's amplitudes and that higher order imaging terms may be required for larger contrasts between actual and reference media properties.

The leading order approximation is better at small angles and is the reason why the leading order imaging series leaves a small amount of residual moveout more noticeable at the higher angles. Data at larger angles of incidence will benefit more from the higher order terms currently being left out. On the other hand, the rate of convergence of the series form of the algorithm will benefit from the fact that the maximum k_z is smaller at large angles (since $k_z \sim k_0 \cos\theta_0$). For higher contrasts, or when greater accuracy is desired, then higher order imaging terms are required that go beyond the leading order terms identified and analyzed here.

6 Summary and Conclusions

The imaging series for a single parameter acoustic medium is a Taylor series for the difference of two Heaviside functions expanded about the depth of each mislocated interface. The prestack form of a leading order imaging series has been isolated whose coefficients are the products of a scalar with the integral of α_1 to increasingly higher powers. The integral of α_1 sends residual moveout and amplitude information from reflectors in the overburden to all mislocated deeper reflectors, thereby establishing a "communication between events" that acts to the correct the depths of the reflectors. The leading order imaging subseries has favorable convergence properties and also has a closed form that straightforwardly encapsulates an infinite number of terms.

The leading order imaging series has been formulated for constant angles of incidence over a 1D layered medium and has been analyzed for several analytic examples. A condition was derived that, when satisfied, shows the leading order imaging series will improve upon the depths predicted by the constant reference velocity.

Results of the analytic examples illustrate the improvement in the predicted depths of the reflectors that are mislocated by current depth imaging algorithms (and that correspond to the first term in the series). The effect of the leading order imaging series can be visualized as correcting the residual moveout of common image gathers that are imaged with the homogeneous reference velocity. The impact of residual internal multiples was shown by example to depend on the model and therefore, in general, it is best to remove multiples before applying the imaging algorithm.

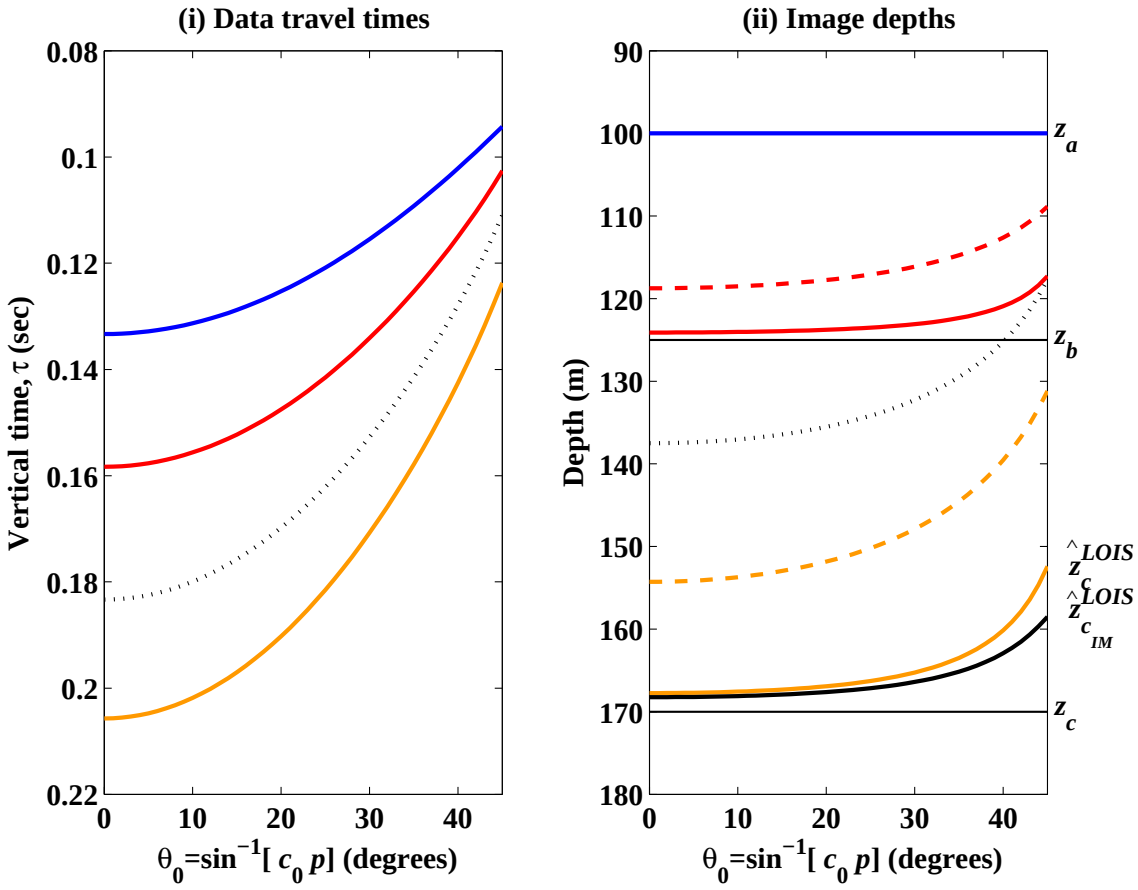

Fig. 3.10: *(i) Travel time curves for three primaries and a first order internal multiple. (ii) Depths predicted by the first term, z_a, $\hat{z}_b$ and $\hat{z}_c$, and the leading order imaging series, z_a, $\hat{z}_b^{LOIS}$ and $\hat{z}_c^{LOIS}$ (all with the same colors and line styles as in Figs. 3.8 and 3.9). The depth $\hat{z}_{c_{IM}}^{LOIS}$ is the depth of the interface at z_c predicted by the leading order imaging series in the presence of the internal multiple. Model parameters are given in Table 3.2. In this case, $\hat{z}_{c_{IM}}^{LOIS}$ is an improvement over $\hat{z}_c^{LOIS}$.*

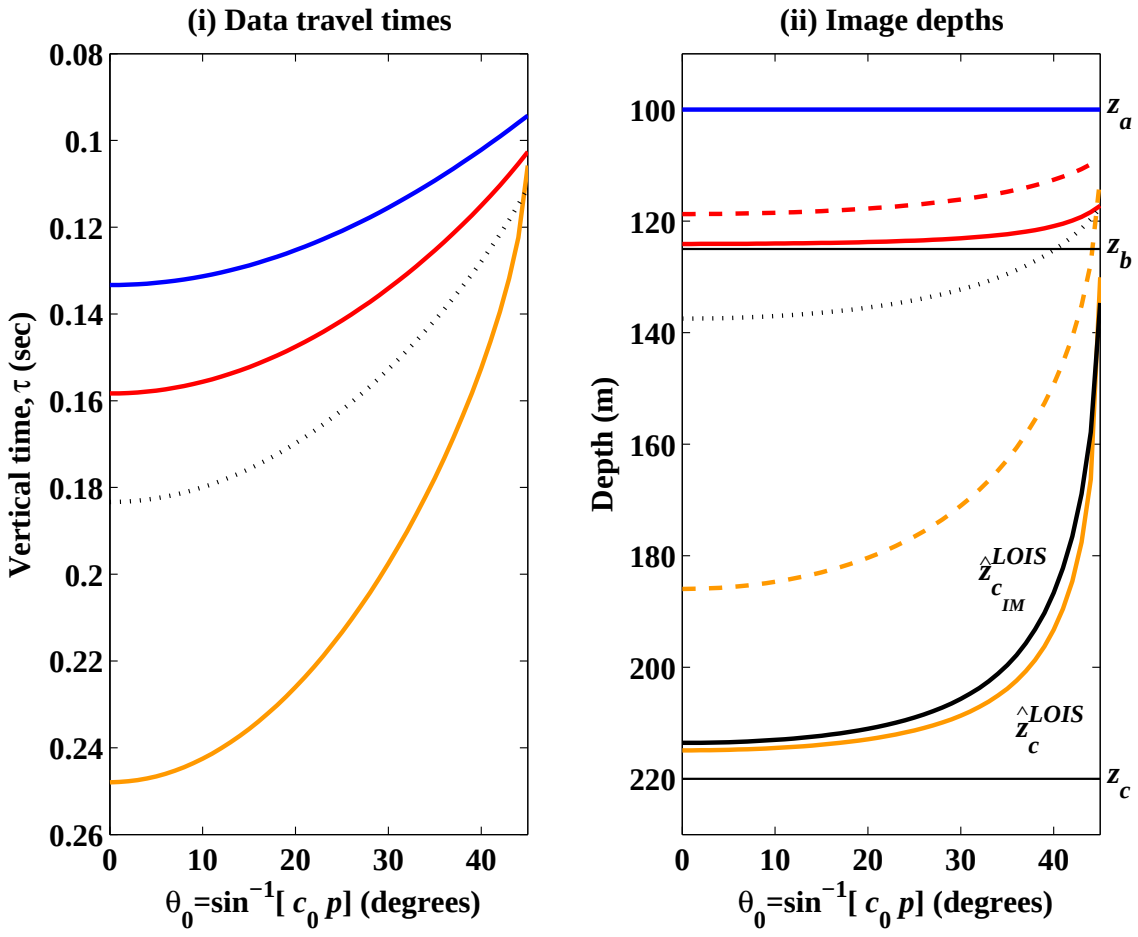

Fig. 3.11: *(i) Travel time curves for three primaries and a first order internal multiple. (ii) Depths predicted by the first term, z_a, $\hat{z}_b$ and $\hat{z}_c$, and the leading order imaging series, z_a, $\hat{z}_b^{LOIS}$ and $\hat{z}_c^{LOIS}$. The depth $\hat{z}_{c_{IM}}^{LOIS}$ is the depth of the interface at z_c predicted by the leading order imaging series in the presence of the internal multiple. Model parameters are given in Table 3.2. In this case, $\hat{z}_{c_{IM}}^{LOIS}$ is* not *an improvement over $\hat{z}_c^{LOIS}$, which is predicted in the absence of internal multiples.*

4. NUMERICAL EXAMPLES OF A LEADING ORDER IMAGING SERIES AND AN ANALYSIS FOR BANDLIMITED INPUT DATA

A subseries of the inverse series has been isolated and has been shown analytically for a suite of interval velocity models to improve the depths of reflectors compared with a linear imaging algorithm using the reference velocity. The next step is to systematically analyze this leading order imaging series under progressively more realistic conditions with the objective of developing it into an algorithm ready for field data application.

We test the 1D prestack acoustic leading order imaging series for a variety of velocity models and bandlimited synthetic datasets. One of our primary objectives is to analyze its performance under conditions when the input data are missing low frequencies. It is demonstrated that, while it benefits from low frequency information, the leading order imaging series retains effectiveness even when zero and some low frequency information are absent. Its effectiveness is enhanced with offset data where the conjugate to depth, $k_z = 2(\omega/c_0)\cos\theta_0$, allows for a lower minimum k_z away from normal incidence and for the same temporal frequency bandwidth.

The relationship between the leading order imaging series and low frequency information is analyzed by examining the imaging series' integral with respect to depth of the first term, α_1. It is shown that the fidelity of the construction of the first term in the low k_z band is important. The integration limits of the integral in the algorithm are not from $-\infty$ to $+\infty$ and so the imaging series does not call strictly for the zero frequency component of the data. We demonstrate using numerical reflectivity data examples that, even when missing zero and low temporal frequency information, the leading order imaging series can improve the predicted depth of reflectors over current imaging with the reference velocity. Greater effectiveness is achieved when lower frequency information is present, which merits the study of existing and new spectral extrapolation techniques and is in alignment with the current trend to acquisition systems that record lower frequency data.

1 Introduction

The development of inverse scattering series algorithms for seismic data processing begins with the isolation of a subseries that accomplishes a specific task, for example, free surface

multiple removal, internal multiple attenuation or depth imaging (Weglein et al., 2003). Once a candidate subseries has been identified for the simplest earth and acquisition models, it is systematically analyzed under progressively more realistic conditions, with the objective being to develop an algorithm ready for field data application.

The imaging series is a subseries of the inverse scattering series, a direct multidimensional inversion procedure, and is non-linear in the measured wavefield. Other non-linear inverse methods (e.g., Tarantola, 1987) have been found to fail in practice because field data are always bandlimited, and missing low frequencies precludes a successful updating of the reference model towards the actual model. One important distinction between the inverse scattering series and iterative linear inversion is that, with the inverse series, the reference model is never updated. Every term in the inverse series is computed through an inversion that requires only the recorded dataset and the original reference medium properties. Furthermore, the inverse subseries and task separation approach (see Chapter 3), which inverts seismic data one step at a time, is in contrast to iterative linear inversion, which uses the total wavefield to directly invert for earth properties at once. This important difference makes any one of the inverse series algorithms less ambitious than a procedure that attempts a wholesale direct inversion for earth parameters from the recorded data.

Despite significant differences between the inverse scattering subseries procedure and other non-linear inversion methods, it might be expected that at least one of the subseries algorithms would benefit from low frequency information. After all, they achieve seismic processing objectives without subsurface information by engaging the data more actively than algorithms that expect accurate *a priori* details about the medium. If the algorithms expect more from the data, then it is reasonable to imagine that at least one of them might benefit from a broad frequency spectrum. According to the convolutional model, a single frequency component from the source will experience the medium in a manner described by a linear differential operator before it is recorded at the receiver. The convolutional model applies to even the most complex absorptive elastic wave equations currently employed to describe wave propagation. However, direct inversion of even the simplest single-parameter acoustic wave equation using the inverse scattering series requires multiplicative communication between different frequencies. This is also a characteristic of the leading order imaging series.

The leading order imaging series has been shown analytically in Chapter 3 to image reflectors closer to their correct spatial location than a linear depth imaging algorithm using the same reference velocity. It does so without solving for the actual velocity model. In this chapter, we continue evaluating the prestack leading order imaging series with a succession of numerical examples. The synthetic datasets are necessarily frequency bandlimited which is also the situation with data acquired in the field. It was also shown in Chapter 3 that the leading order imaging series will not converge for infinite k_z (vertical wavenumber), and it was commented that the temporal band-limit of recorded seismic data will naturally satisfy this convergence criterion. In this chapter, we numerically demonstrate convergence of the leading order imaging series for a variety of normal and non-normal incidence 1-D acoustic synthetic datasets, and for different high- and low-frequency apertures.

One of our primary objectives is to analyze the role of low frequency information in the leading order imaging series and, specifically, to answer the question of whether it retains any benefit when low frequency information is absent from the data. We utilize the 1-D prestack form of the algorithm which more closely represent the actual seismic experiment than a normal incidence algorithm because the source-receiver offset leads to a lower vertical wavenumber, k_z. The issue of missing low frequency in non-linear inversion is more usefully thought of in terms of missing low k_z, rather than missing low temporal frequency, ω.

We begin by studying bandlimited numerical examples that contain zero and low frequencies and then progress to examples that are missing information from the low end of the frequency spectrum.

2 Numerical examples

2.1 Numerical examples at normal incidence

We consider again the simplest imaging problem of two reflectors in a constant density acoustic medium with no free surface. The two interfaces are defined by the following parameters (see the model depicted in Fig. 3.7):

Layer velocities (m/sec)		Interface depths (m)	
c_0	1500		
c_1	1650	z_a	100
c_2	1510	z_b	140

Tab. 4.1: *Model parameters corresponding to the results in Figs. 4.1, 4.2 and 4.3.*

The source wavelet is designed to be zero phase with an amplitude $A(\omega) = 1$ in the frequency band $0 \leq f \leq 125$ Hz where $\omega = 2\pi f$. The $p = 0$ (normal incidence) component of the data are displayed in the left-hand panel of Fig. 4.1 as a function of vertical travel time, τ. In accordance with the strategy of task separation, there are no multiple reflections in these input data. The remaining panels show the results of the first six terms in the leading order imaging series computed using Eq. (3.39). The second term is recognizable as a weighted sinc function – a bandlimited version of the delta function in Eq. (3.26) – centered at the reference velocity depth, $\hat{z}_b$. Increasingly higher order derivatives of the sinc function in the higher order terms are alternately antisymmetric and symmetric about $\hat{z}_b$. The amplitudes of the non-linear terms in this example are seen to diminish gradually with successive terms. In Fig. 4.2, the cumulative sums of these first six terms are displayed. For this model, the leading order imaging series is observed to converge after approximately six terms and the mislocated interface has been shifted from the reference depth, $\hat{z}_b$, in α_1 closer to the actual depth, z_b, in α^{LOIS}. Summing more terms in the leading order imaging series for this example does not further correct the depth because the seventh and higher order terms are too small.

Figure 4.3 compares the result of summing the first six terms in the series algorithm with computing the closed form (Eq. 3.43). The two results are observed to be very similar although the computation of the closed form is much simpler to implement and faster to execute than the series formula. Furthermore, implementation of the series formula involves taking high-order derivatives which can raise certain practical issues (see, e.g., Corrêa et al., 2002). Performing accurate and stable numerical derivatives is not required by the closed form algorithm. To avoid issues related to numerical implementation, the closed form will be used for the analysis of the leading order imaging series in the remainder of this chapter.

Figure 4.3 shows clearly that the leading order imaging series does not alter the amplitude of α_1 and that it only moves the mislocated interface. This is because terms that correct the amplitude of α_1 towards α are excluded. Therefore, the result of applying α^{LOIS} is to have an α_1-like quantity with its interfaces more accurately located than in α_1. Since we don't know α before or after computing α^{LOIS}, we are unable to find the actual velocity by this procedure. This is a fascinating property of direct inversion: the method can achieve certain inversion objectives without knowing the medium properties before, during or after application of the algorithm.

Figure 4.4 illustrates the results of the closed form algorithm on a four layer model described by the following values (see Fig. 3.7):

Layer velocities (m/sec)		Interface depths (m)	
c_0	1500	z_a	100
c_1	1650	z_b	150
c_2	1550	z_c	200
c_3	1600	z_d	300
c_4	1550	z_e	400

Tab. 4.2: Model parameters corresponding to the results in Fig. 4.4.

The input data were synthesized for the same bandlimited source as in the previous example. To a high degree of accuracy, the leading order imaging series has well-positioned the interfaces at their correct depths.

2.2 Pre-stack numerical examples

We test the prestack leading order imaging series on data synthesized using an acoustic reflectivity algorithm (see, e.g., Kennett, 1983) and select the option to synthesize a point source exploding in a three dimensional space. The velocity varies only in the z-direction and density is held constant. The data are synthesized in the τ-p domain and can be considered to have been generated from an experiment with infinite spatial aperture. The source wavelet is designed to be a bandlimited delta function with a frequency spectrum $A(2\pi f)$ where $f_{\min} \leq f \leq f_{\max}$.

First, two specific cases are considered: one representing the situation where the reference velocity is slower than the actual velocity, and one where the reference velocity is faster. In the former example, the velocities are $c_0 = 1500$ m/s, $c_1 = 1650$ m/s and $c_2 = 1500$ m/s, and so the critical angle for a downgoing plane wave at the first interface is 65°. In the latter example, the velocities are $c_0 = 1500$ m/s, $c_1 = 1350$ m/s and $c_2 = 1500$ m/s, and there is no critical reflection at the first interface. The depths of the two interfaces in both examples are $z_a = 1000$ m and $z_b = 1075$ m.

Figure 4.5 shows the reflectivity data for the two models. In both cases, the minimum and maximum source frequencies are $f_{\min} = 0.25$ Hz and $f_{\max} = 62.5$ Hz, respectively. We choose to display the result as "spike-like" data, rather than "box-like" α_1, by taking the derivative of the result with respect to z. This is done because it is easier to view the shifting of reflectors when displayed in "spike-like" form. Figure 4.6 shows the results of imaging the data in Fig. 4.5 using the constant reference velocity, c_0. The mislocated reflector exhibits residual moveout when imaged with the first term in the series (left). The leading order imaging series (right) improves the depth at all angles and acts to "flatten" the imaged reflector. As expected from the analysis of the leading order approximation in Chapter 3, a small amount of residual moveout remains.

Figure 4.7 shows the velocity profile and synthetic data for a six-layer model. Using the same source wavelet ($0.25 \leq f \leq 62.5$ Hz), the imaging results are compared in Fig. 4.8. The leading order imaging series improves the location of all the reflectors mislocated by the first term. The remaining errors in the predicted depths would presumably be corrected by higher order imaging terms (see Chapter 5). A small cumulative error in depth noticeable in Fig. 4.8 is attributed primarily to the fact that the integral of the data in the overburden necessarily includes transmission coefficients that introduce small errors in the shifts (as discussed in Chapter 3).

We have demonstrated the effectiveness of the leading order imaging series on synthetic data for a variety of 1-D models. In all the examples so far, the input data contained information down to relatively low frequency ($f_{\min} = 0.25$ Hz). From Eq. (3.43), it is clear that the shift of each interface is proportional to the integral of α_1 above the reflector being imaged. This integral captures amplitude and residual moveout information in the overburden of each reflector and emphasizes α_1 at low k_z values over α_1 at high k_z values (because it is a division by k_z in the Fourier domain). The fidelity of α_1 and its integral will have a direct impact on the performance of the imaging series. In the next section, we take a closer look at the role of low frequencies in α_1 and in the leading order imaging series.

3 The role of low frequency information in the leading order imaging series

For the medium in which Eq. (3.1) describes acoustic wave propagation, and a velocity perturbation, α, defined by Eq. (3.4), the leading order imaging series can be written as an

infinite sum of operations on the first term:

$$\alpha^{\text{LOIS}}(z,p) = \sum_{n=0}^{\infty} \underbrace{\frac{(1/2)^n}{n!\cos^{2n}\theta_0}}_{\substack{\text{Angle-dependent}\\ \text{scalar}}} \times \underbrace{\left(\int_0^z \alpha_1(z',p)dz'\right)^n}_{\substack{\text{Emphasizes low}\\ \text{frequency}}} \times \underbrace{\frac{\partial^n \alpha_1(z,p)}{\partial z^n}}_{\substack{\text{Emphasizes high}\\ \text{frequency}}} \tag{4.1}$$

where we have labelled the parts of the algorithm according to their effect on the frequency spectrum of α^{LOIS}. The closed form solution is

$$\alpha^{\text{LOIS}}(z,p) = \alpha_1(z+\Delta,p) \tag{4.2}$$

where

$$\Delta(z) = \underbrace{1/(2\cos^2\theta_0)}_{\substack{\text{Angle-dependent}\\ \text{scalar}}} \underbrace{\int_0^z \alpha_1(z',p)dz'}_{\substack{\text{Emphasizes low}\\ \text{frequency}}} \tag{4.3}$$

which retains the series algorithm's emphasis of the low frequency information in α_1 but has cast out the high-frequency derivatives which were summed in Eq. (3.42). In other words, the dependence of the leading order imaging series on the integral of α_1 is present in both its series and closed forms.

It is important to remember that Eqs. (4.1) and (4.2) reflect a particular choice of parameterization that arose due to the degree of freedom in the data (see Chapter 3). The first term, α_1, is computed directly from the data via (Eq. 3.11):

$$\alpha_1(z,p) = -8\zeta_0\cos^2\theta_0 \int_{-\infty}^{+\infty} e^{-i\omega\zeta_0(2z-(z_g+z_s))} \int_0^{\infty} D(r;\omega)J_0(\omega pr)rdrd\omega \tag{4.4}$$

where the dispersion relationship is (see Fig. 4.9)

$$k_z = -2\frac{\omega}{c_0}\sqrt{1-\frac{k_r^2c_0^2}{\omega^2}} = -2\omega\zeta_0 = -2\frac{\omega}{c_0}\cos\theta_0. \tag{4.5}$$

The choice of constant-p (or constant-θ_0) is illustrated in Fig. 4.10. In practice, data are acquired with both temporally- and spatially-limited apertures: we record for a finite amount of time, it is logistically difficult to record zero or very small offsets, we can only record a finite maximum offset, and conventional 3D surveys have limited crossline aperture or source-receiver azimuth.

To keep the current discussion to the effect of missing low temporal frequency, it is assumed that the source-receiver offset aperture $r = 0 \to \infty$. Therefore, the integral of the data over r in Eq. (4.4) is assumed to be accurately computable. In the event that source-receiver offset is limited, methods exist to compute the finite aperture integrals (e.g., Stolt and Benson,

1987). The minimum k_z in α_1 is a function of the reference angle of incidence and the minimum source frequency:

$$(k_z)_{\min} = \frac{(\omega)_{\min}}{c_0} \cos\theta_0. \tag{4.6}$$

An alternative approach to handling the degree of freedom in the data (see, e.g., Eq. 3.10) is to keep ω fixed and integrate over angle or the reference vertical slowness, ζ_0. This parameterization (illustrated in Fig. 4.11) will result in different estimates of $\alpha_1(z)$ for constant ω values. Throughout this thesis, we have chosen to hold p fixed.

The emphasis of low frequencies in the leading order imaging series is really an emphasis of the vertical wavenumber, k_z. There is more than one way to compute $\alpha_1(k_z)$. For example, to compute $\alpha_1(k_z = 0)$, we can either set $\omega = 0$ or $k_r = \omega/c_0$. Since $k_z = -2k_0 \cos\theta_0$, then $k_z \to 0$ when $\theta_0 \to 90°$. In other words, large angles of incidence can construct α_1 at low k_z values.

The issue of missing low frequency is considered in the context of the source wavelet being frequency bandlimited. Therefore, as a consequence of the convolutional model, the recorded data will have finite aperture in frequency as depicted in Fig. 4.12. The two integrals of the data in Eq. (4.4) call for infinite apertures in angular temporal frequency and offset (ω and r, respectively). Although the Bessel function contains an integral over azimuth, it is not a function of the data. To compute α_1 as a function of vertical time, τ, these are replaceable by integrals of the data over azimuth, ϕ, and offset (Eq. 3.12) or, in cartesian coordinates, x and y (Eq. 3.13).

3.1 The effect of missing low frequency information at normal incidence

For the general two-reflector analytic example in Chapter 3, and given all temporal frequencies, $\alpha_1(z, p)$ consists of two Heaviside functions, one for each reflector:

$$\alpha_1(z,p) = 4\cos^2\theta_0 \left[R_{01}(p) H\left(z - z_a\right) + \hat{R}_{12}(p) H\left(z - z_{b'}\right) \right]. \tag{4.7}$$

We proceed by first considering the special case of normal incidence, i.e., $\theta_0 = p = 0$. The effect on $\alpha_1(z, p)$ when the ω spectrum is bandlimited is to produce k_z-bandlimited Heaviside functions[1]. This is illustrated in Fig. 4.13 for a particular model (c_0=1500 m/sec, c_1=1650 m/sec, c_2=1510 m/sec, z_a=1000 m, $z_{b'}$=1075 m) and a range of different minimum frequencies ($f_{\min} = \omega_{\min}/2\pi = 0$, 1, 2, 3 Hz). Plotted beside each $\alpha_1(z, \theta_0 = 0)$ is its integral, which is an indication of how the leading order imaging series shift will be affected by missing low frequency information.

As low frequency information is erased from the input data, the integral of α_1 deviates from its analytically computed values for infinite bandwidth. This error will impact the shift

computed by the leading order imaging series as shown in Fig. 4.14. Even though the data contain no information below 1 Hz, the second interface still shifts towards the correct depth z_b because the integral of α_1 is a fair approximation to the exact value computed with infinite bandwidth. As a result of the error in the integral for $z \leq z_a$, the reflector that was correctly imaged at z_a by α_1, is shifted slightly to a shallower depth.

The results in Fig. 4.14 can be significantly improved by recognizing that the area under the α_1 curve for $z < z_a$ is largely responsible for the error in the integral of α_1 at $z > z_a$ (see Fig. 4.13). It is known *a priori* that the perturbation $\alpha(z < z_a) = 0$ (and, by extension, $\alpha_1(z < z_a) = 0$) because the reference medium agrees with the actual medium at the measurement surface. It is not physically possible for the perturbation to be non-zero before the onset of the recorded reflectivity. This effect of missing low frequency can be straightforwardly rectified: rather than integrate from the measurement surface through an α_1 that is obviously in error, we choose to begin computing the integral at some small distance ϵ above the first reflector whose location is well-defined. We can further improve the integral of α_1, and impose a known condition, by fixing the value of the perturbation at $\alpha_1(z_a - \epsilon)$ to be zero and shifting all values of α_1 for $z > z_a - \epsilon$ by the value at $z_a - \epsilon$. Figure 4.15 illustrates the significant improvement in α_1 and its integral when making this simple correction. Implementing this causality-like condition in the leading order imaging series gives

$$\hat{\alpha}^{\text{LOIS}}(z,p) = \alpha_1\left(z + \hat{\Delta}, p\right). \tag{4.8}$$

where

$$\hat{\Delta} = \frac{1}{2\cos^2\theta_0}\left(\int_{z_a-\epsilon}^{z} \alpha_1(z',p)dz' - \alpha_1(z_a-\epsilon,p)\right) \tag{4.9}$$

In all subsequent examples, we implement the leading order imaging series by imposing the condition that the perturbation must be zero before the onset of the scattered field. Then, for the same example as in Fig. 4.14, Fig. 4.16 shows the improvement in the result of the leading order imaging series when provided with this new integral of α_1.

Figures 4.17–4.19

[1] The identity $H^n(\cdot) \equiv H(\cdot)$ (see, e.g., Eq. 3.31) is only valid for full bandwidth Heaviside functions but is avoided in the closed form.

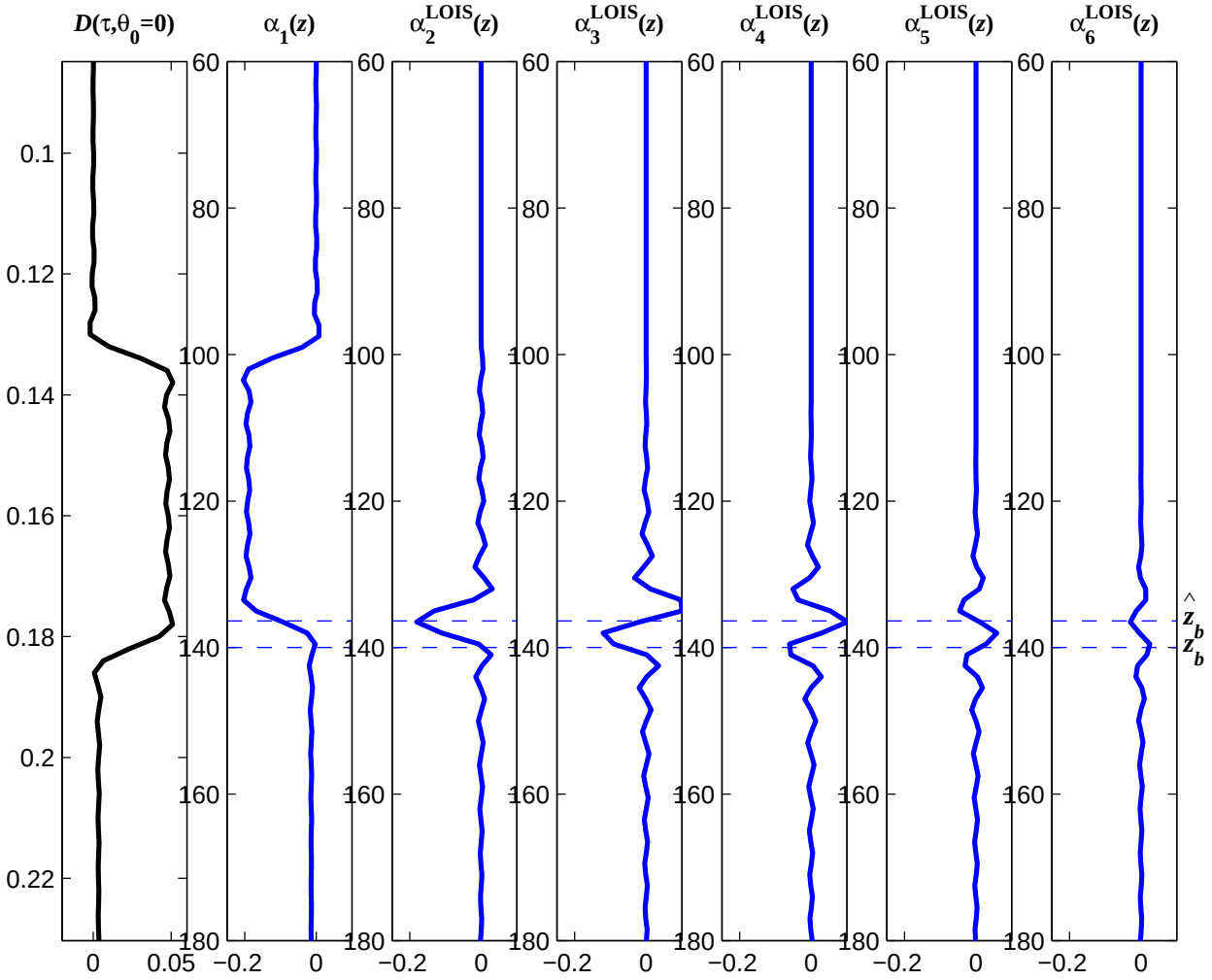

Fig. 4.1: *The normal incidence component of the data, $D(\tau, \theta_0 = p = 0)$, and the first six terms in the leading order imaging series for a two-interface model. After summing six terms, the deeper interface has shifted from $\hat{z}_b$ towards z_b.*

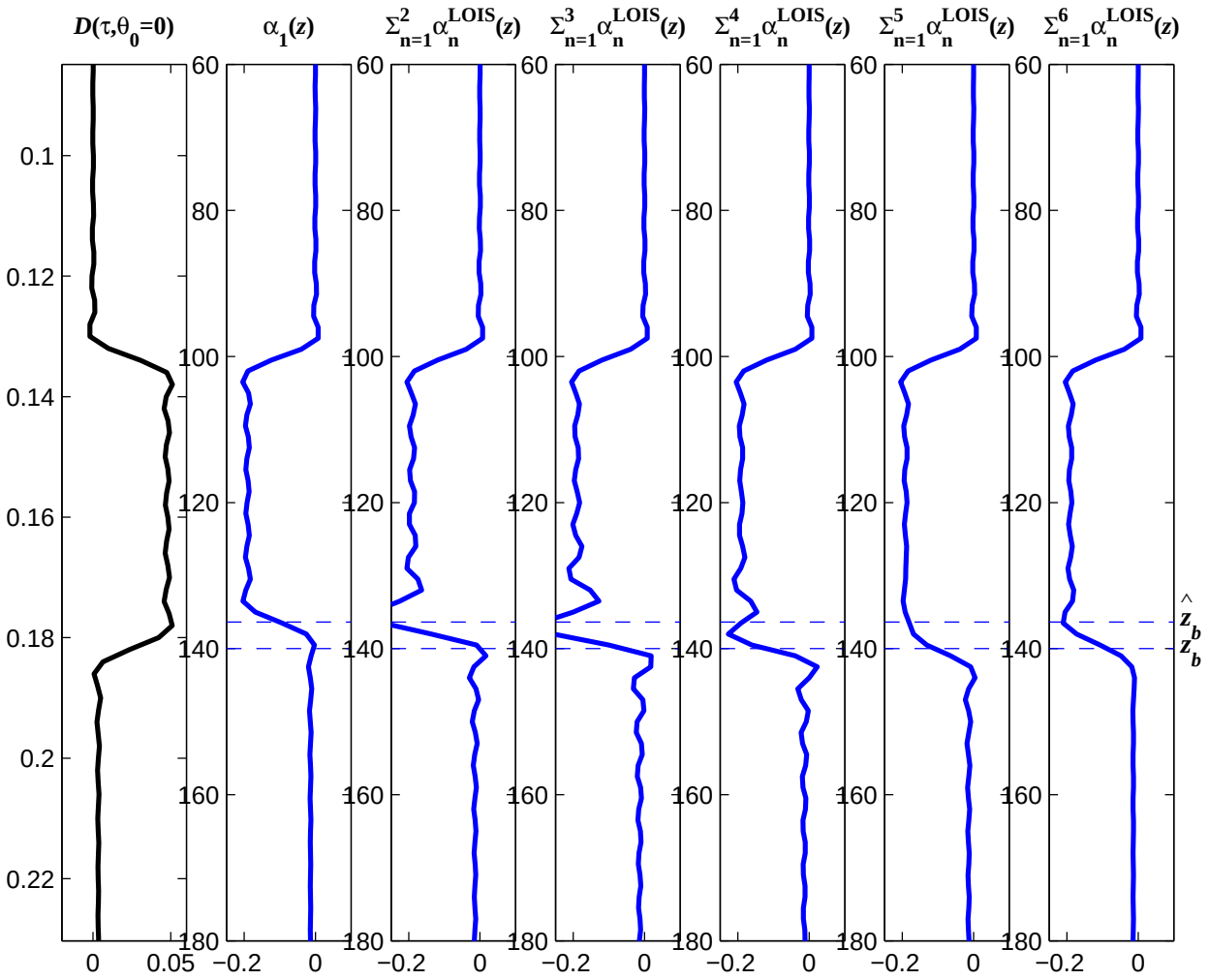

Fig. 4.2: The normal incidence component of the data, $D(\tau, \theta_0 = p = 0)$, and the cumulative sums of the first six terms in the leading order imaging series for a two-interface model.

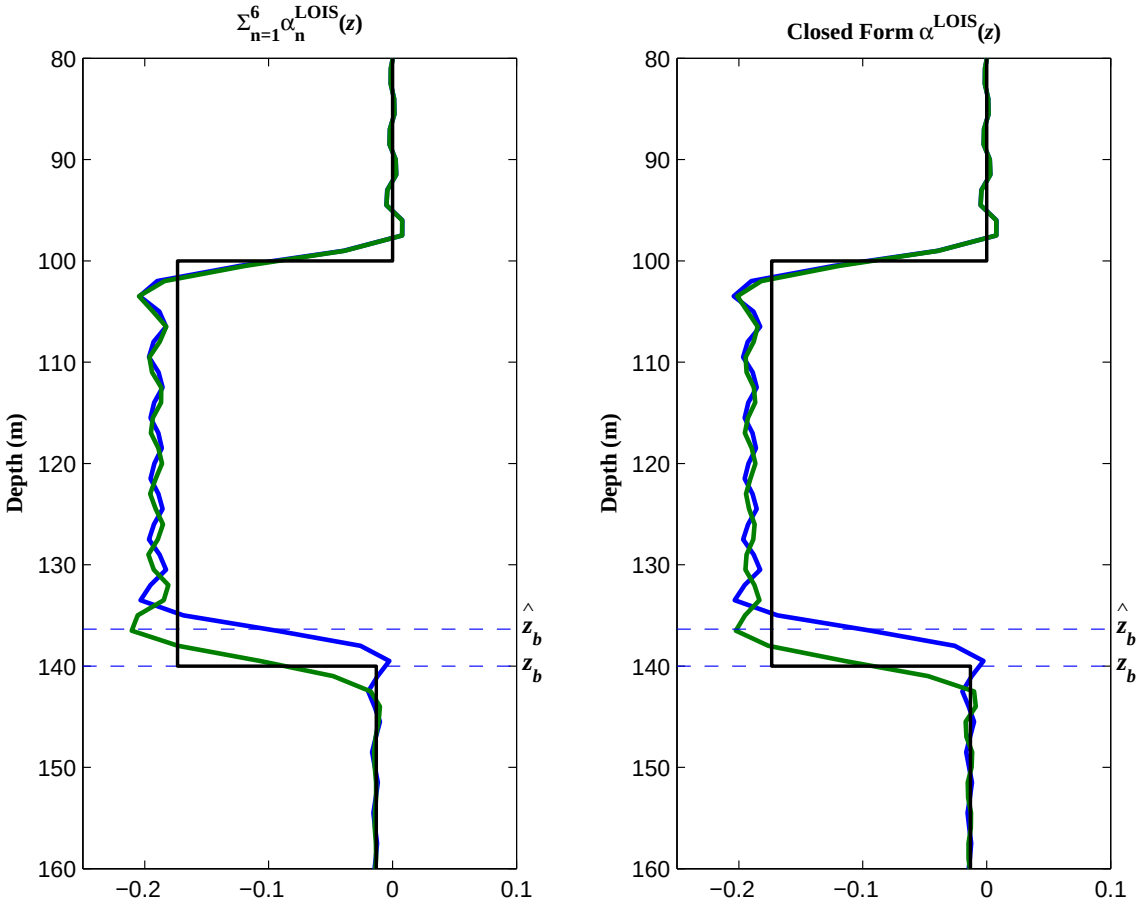

Fig. 4.3: *A comparison of summing the first six terms in the leading order imaging series (left) versus computing the closed form (right). The thin line is the full-bandwidth α and the blue line is α_1. The green line is the leading order imaging series, α^{LOIS} computed two different ways.*

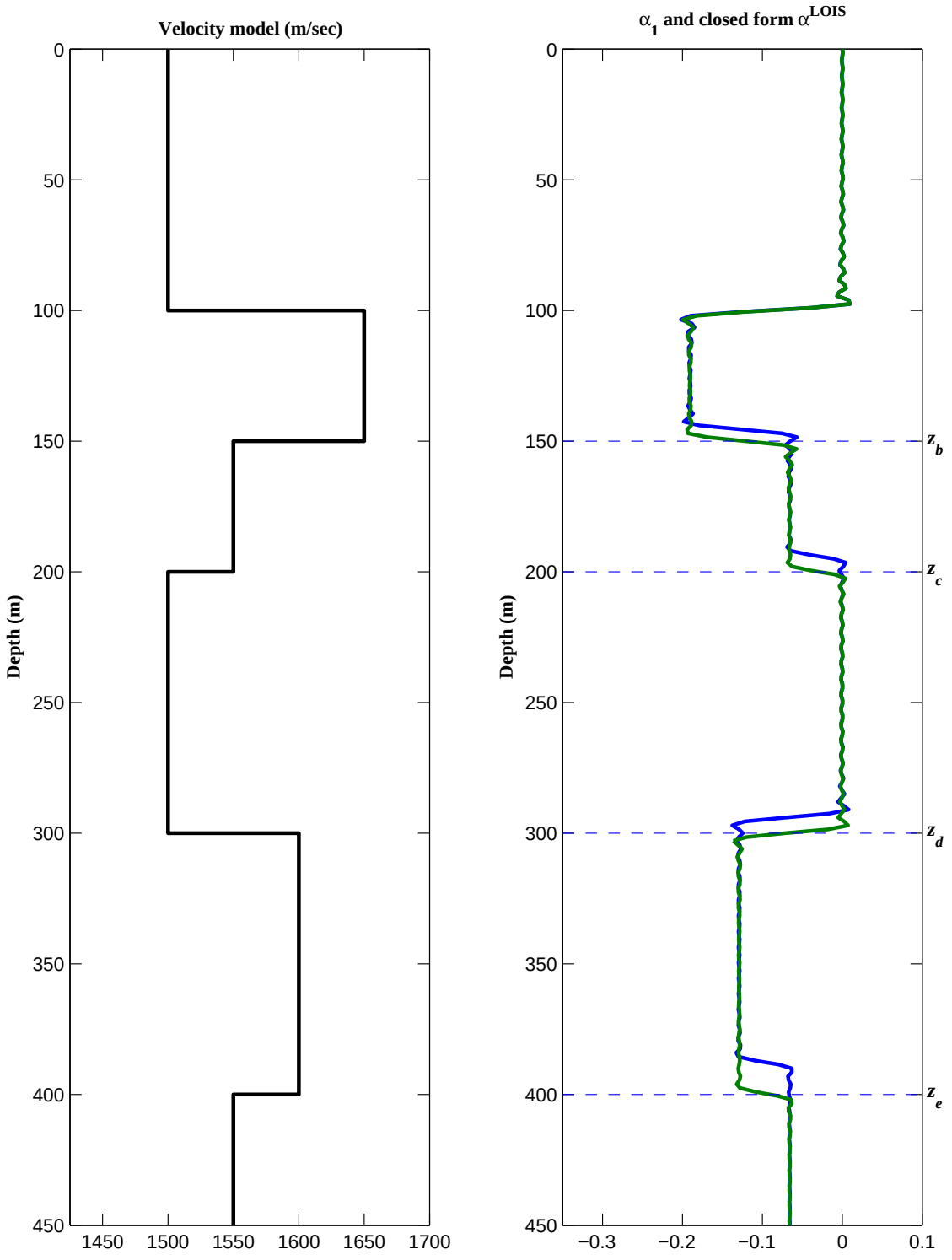

Fig. 4.4: A four-layer velocity model (left) and the closed form leading order imaging series (green, right) compared with the first term (blue, right).

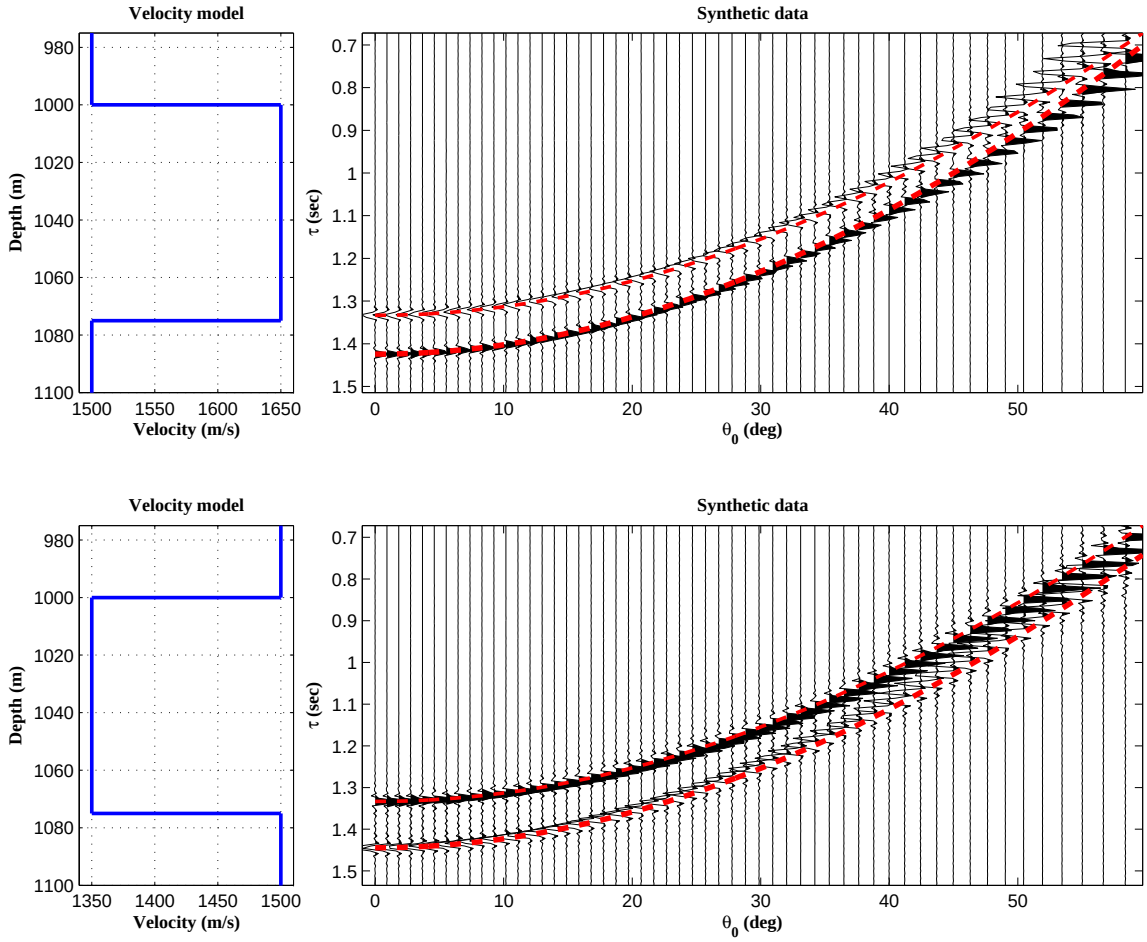

Fig. 4.5: Velocity model and synthetic reflectivity data in the τ-p domain for two specific two-interface examples. The time derivatives of the data are displayed and the polarity is consistent with the wave equation (Eq. 3.1). The red lines overlying the seismic data are the analytically computed τ values for each reflector.

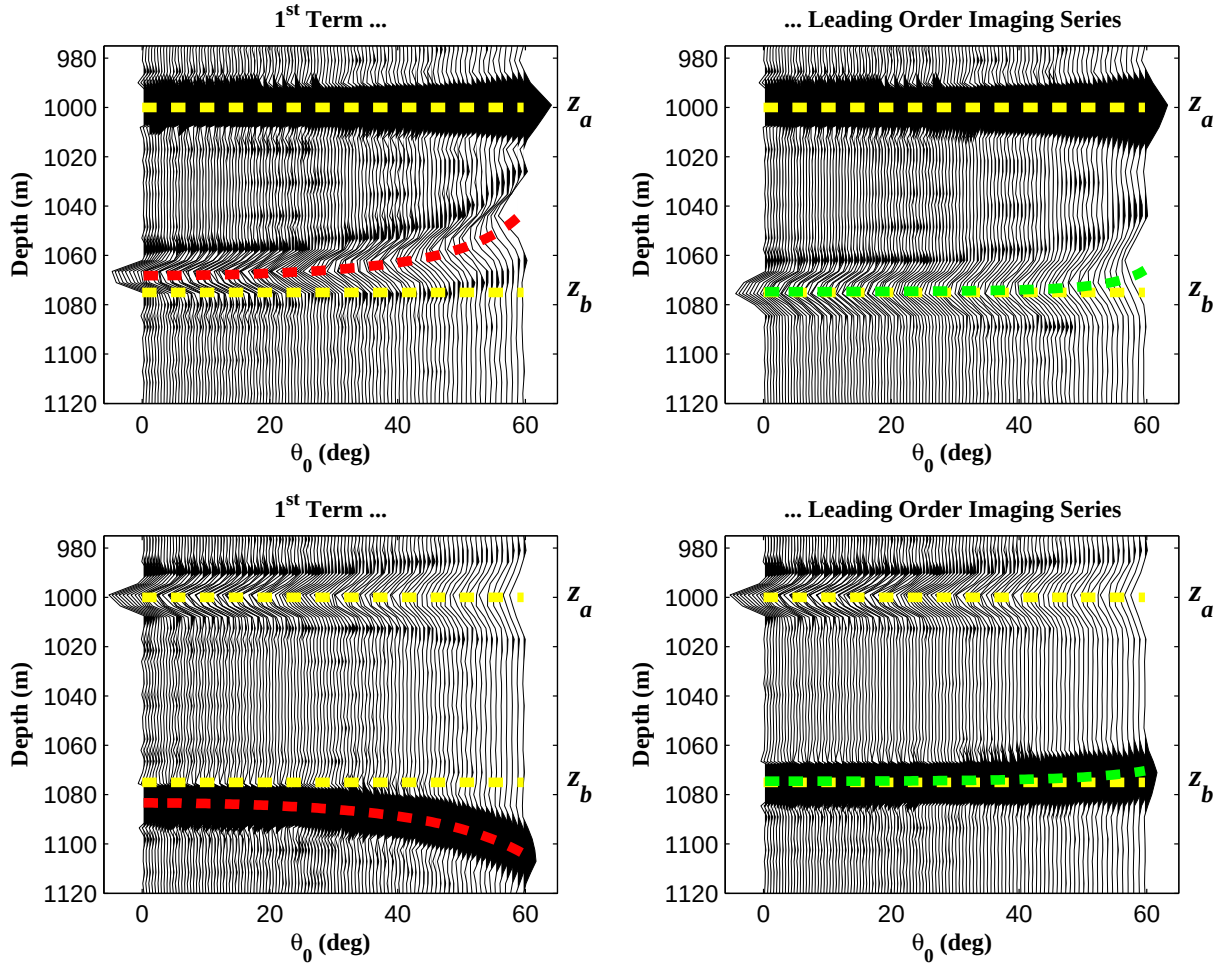

Fig. 4.6: *Results of imaging the two datasets in Fig. 4.5. At top is the example where the velocity increased, and at bottom is the example where the velocity decreased. On the left is the first term in the series: the result of an imaging algorithm that is linear in the data. On the right is the result of the leading order imaging series. The derivatives with respect to depth of α^{LOIS} are displayed. The yellow lines are the actual depths of the two reflectors. The red and green lines are the predicted depths computed analytically using Eqs. (3.58) and (3.60), respectively.*

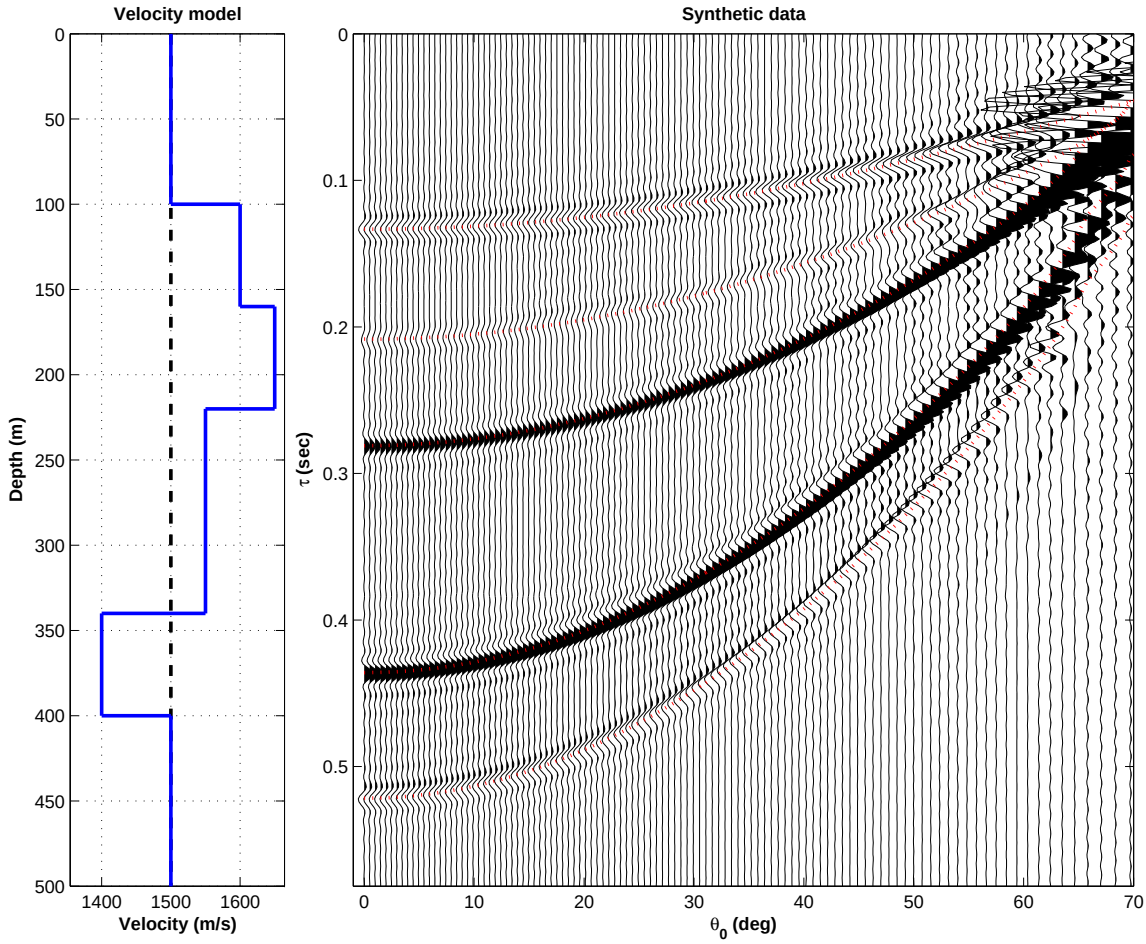

Fig. 4.7: *Velocity profile and synthetic reflectivity data in the τ-p domain for a six-layer model. The time derivatives of the data are displayed. The red lines overlying the seismic data are the analytically computed τ values for each reflector.*

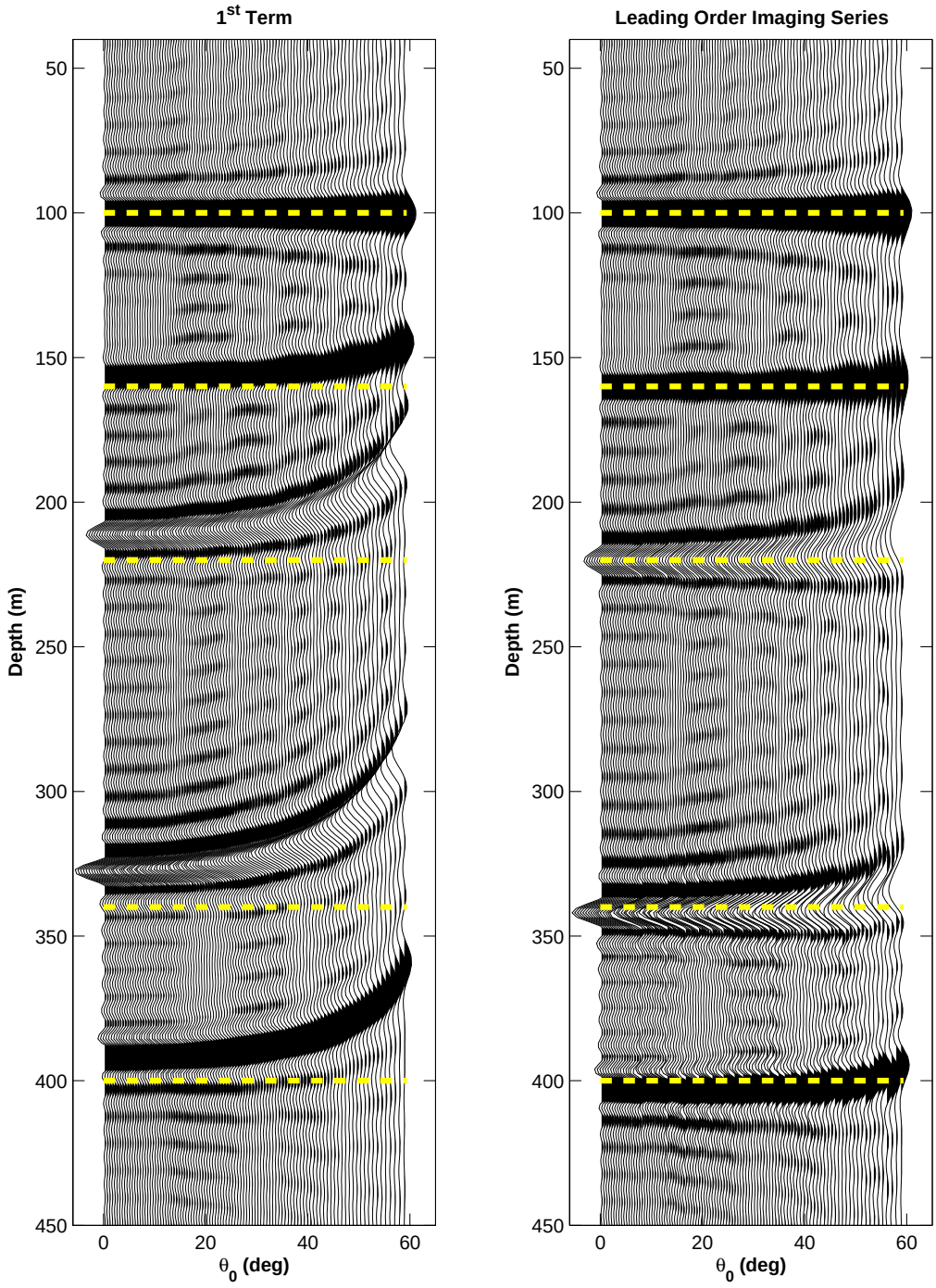

Fig. 4.8: Results of imaging the data in Fig. 4.7. On the left is the first term in the series: the result of an imaging algorithm that is linear in the data. On the right is the result of the leading order imaging series. The yellow lines are the actual depths of the reflectors.

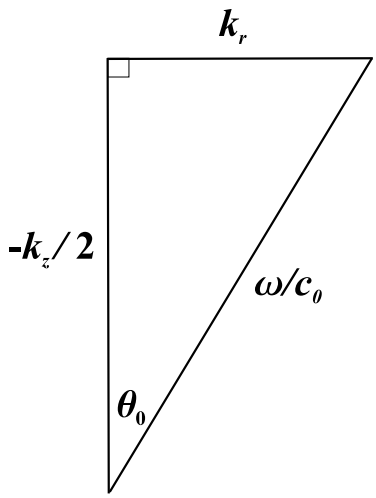

Fig. 4.9: *The dispersion relationship between the vertical and horizontal wavenumbers and temporal frequency.*

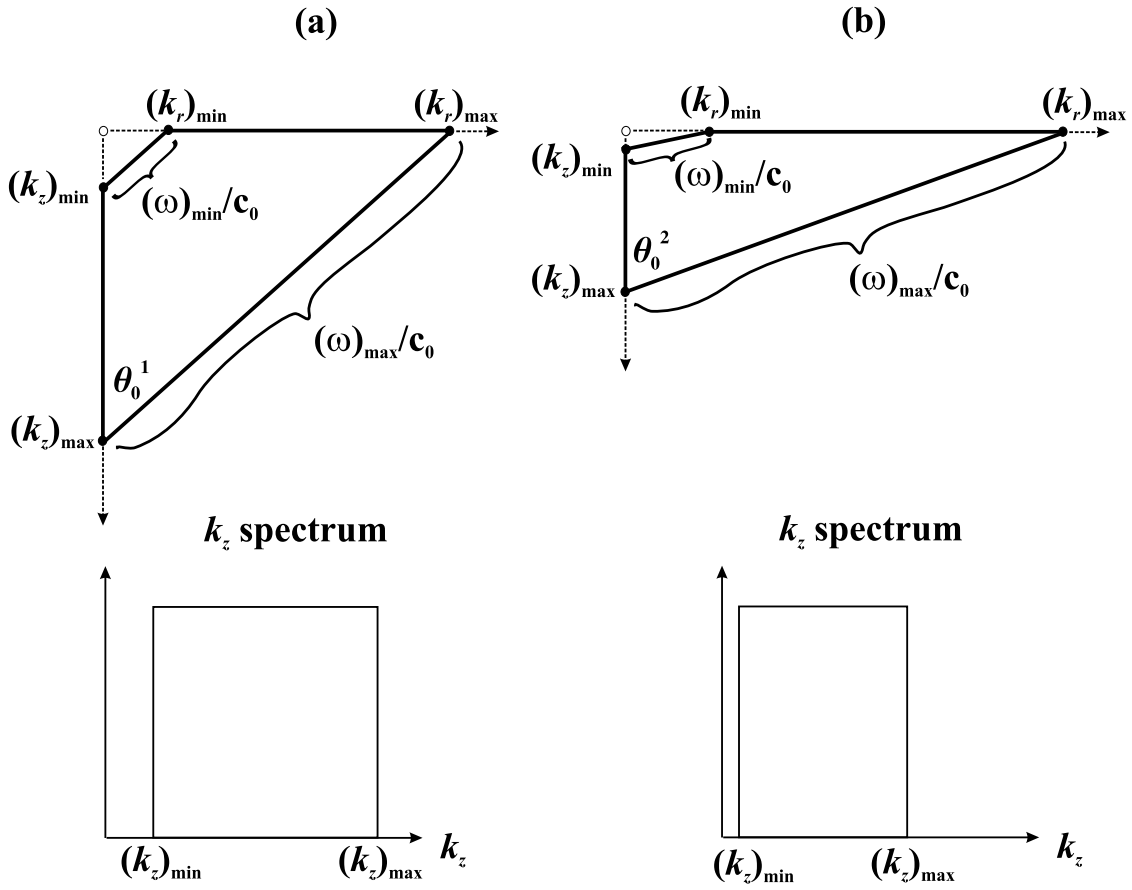

Fig. 4.10: The constraints imposed by bandlimited ω for two different angles of incidence, θ_0^1 and θ_0^2. Both $(k_z)_{min}$ and $(k_z)_{max}$ will be smaller for larger angles.

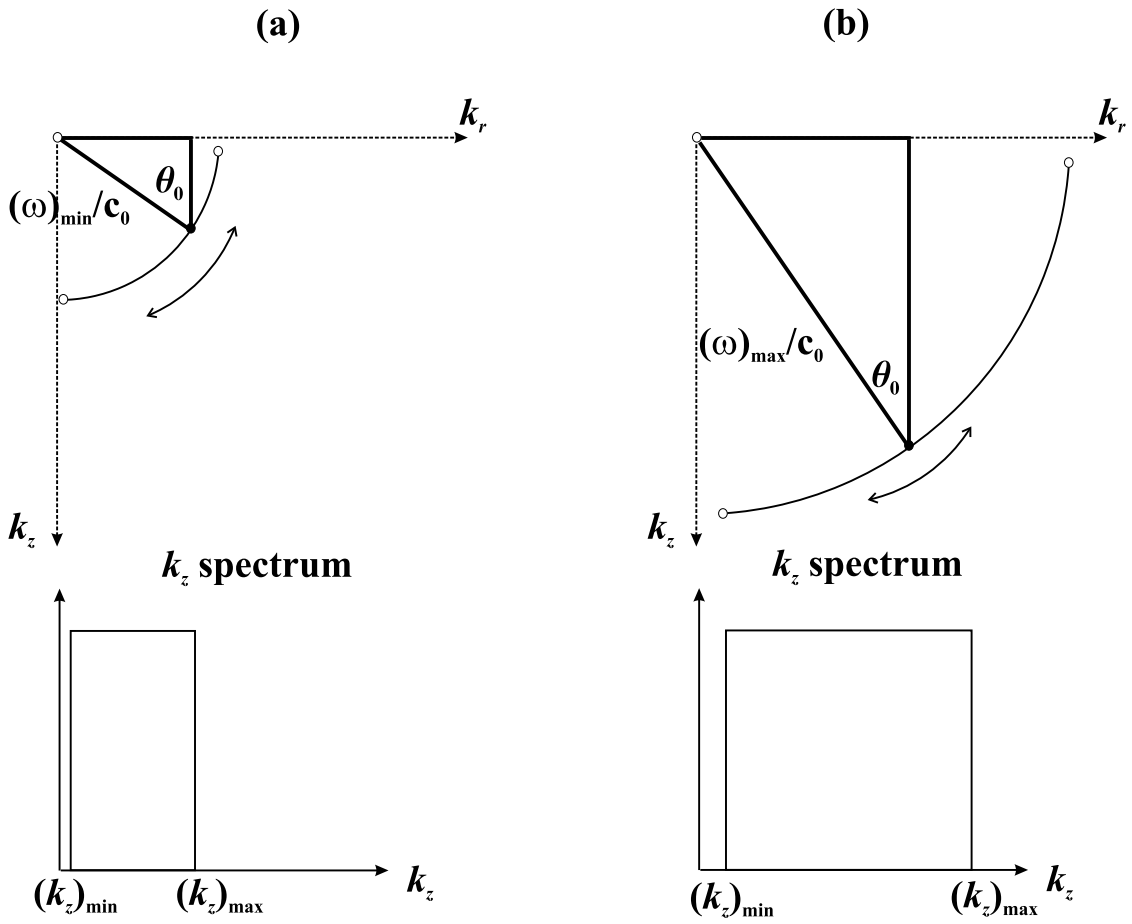

Fig. 4.11: *The constraints imposed by bandlimited ω on the bandwidth of k_z when integrating over angle. On the left is the k_z spectrum constrained by the minimum frequency of the source, $(\omega)_{min}$, and on the right is the k_z spectrum constrained by the maximum frequency of the source, $(\omega)_{max}$. This constant-frequency parametrization is an alternative to the one illustrated in Fig. 4.10.*

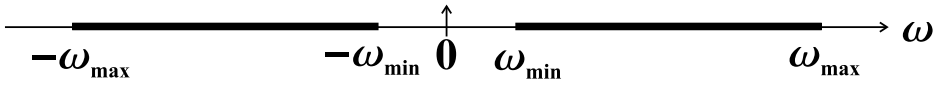

Fig. 4.12: *In practice, ω will be bandlimited between ω_{min} and ω_{max}.*

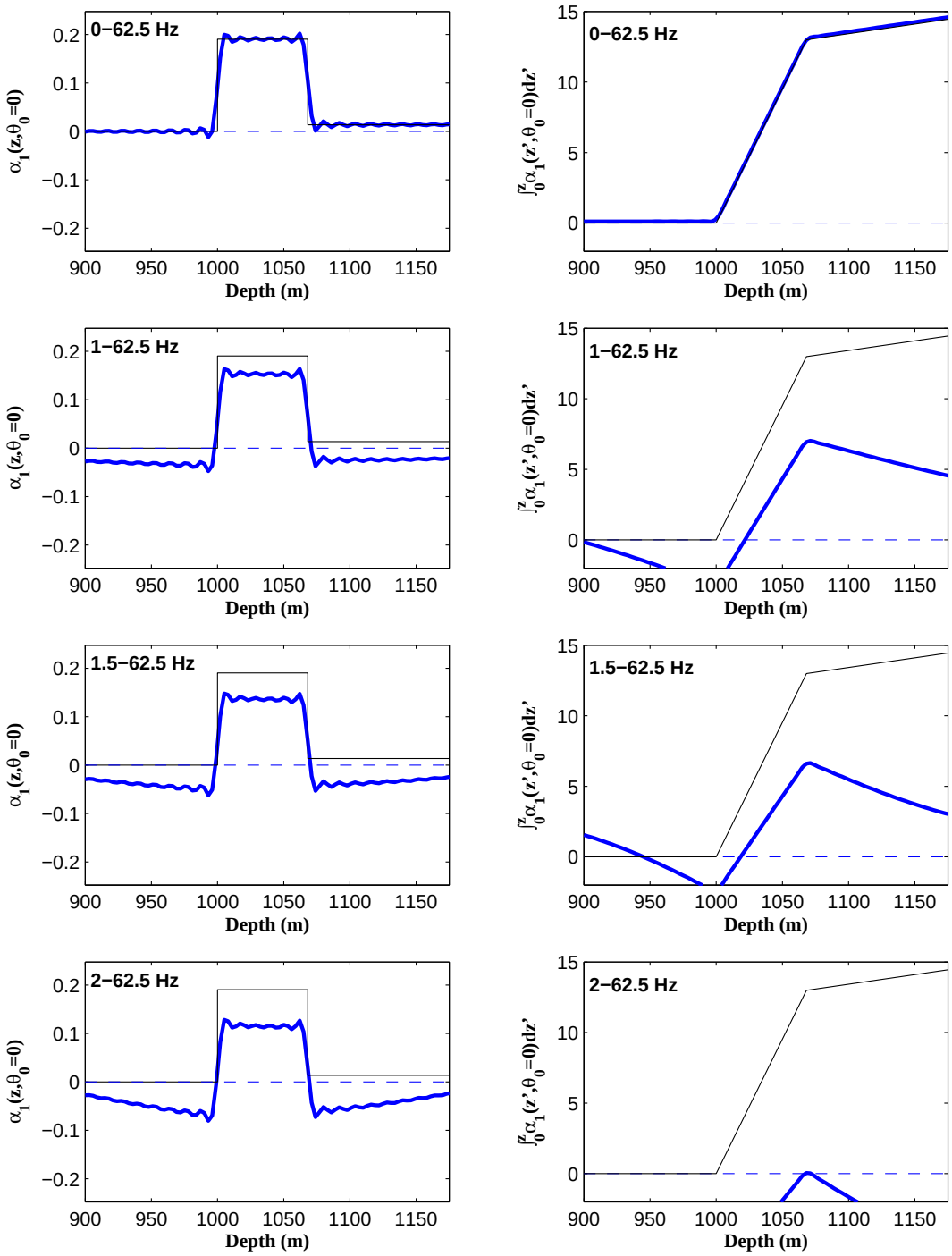

Fig. 4.13: *The effect of missing low frequencies on $\alpha_1(z)$ (left) and its integral (right). The thin black lines are analytically computed values of α_1 and its integral for infinite bandwidth. The thick blue lines are the numerically computed values for bandlimited input data.*

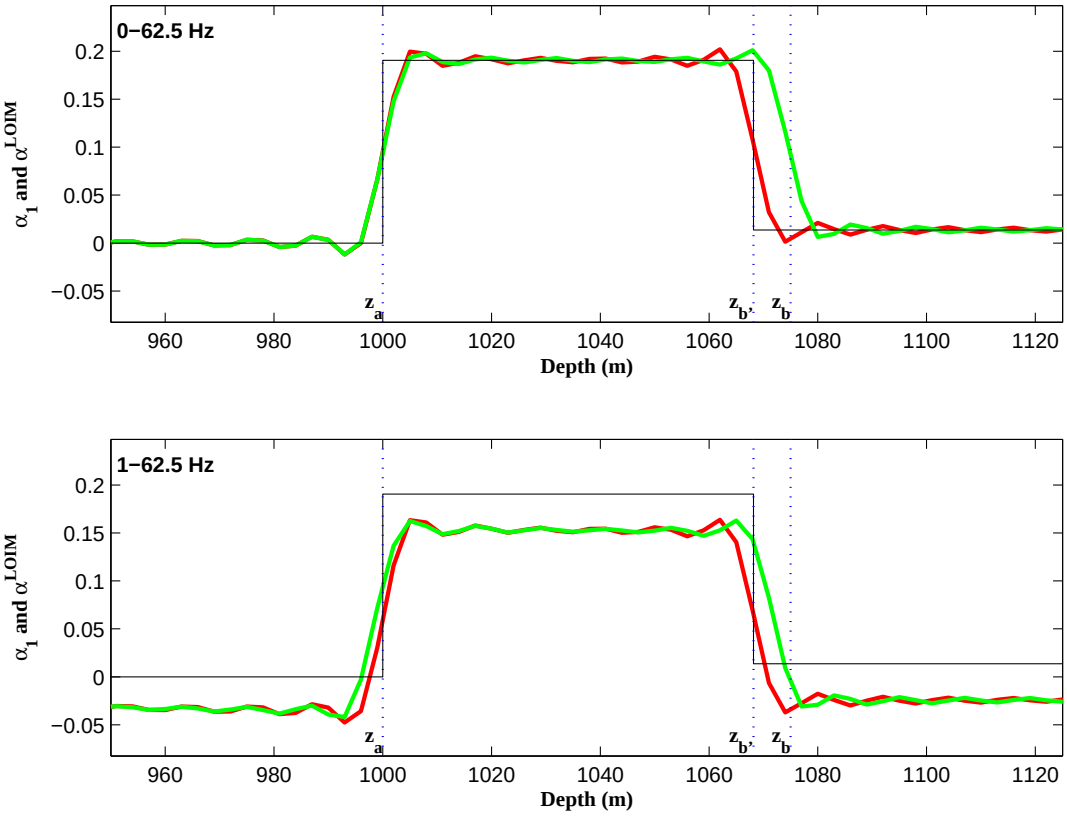

Fig. 4.14: The effect of missing low frequencies on $\alpha_1(z)$ (in red) and $\alpha^{LOIS}(z)$ (in green). Despite not having any information below 1 Hz, the second interface still shifts towards the correct depth z_b. There is a small error at the first interface which can be eradicated by changing the integration limits (Fig. 4.16).

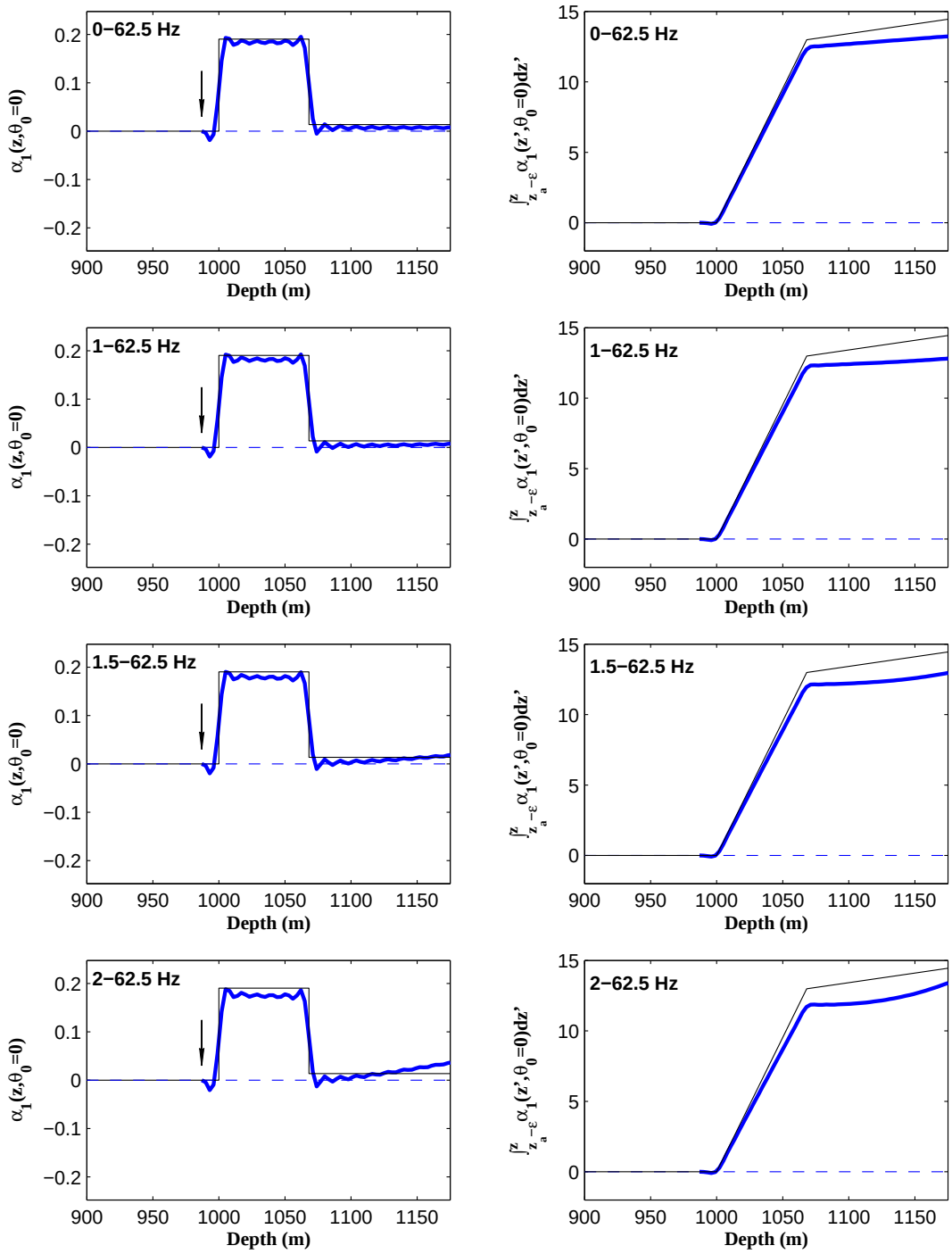

Fig. 4.15: *The effect of missing low frequencies on $\alpha_1(z)$ and its integral when changing the integration limits from $\int_0^z$ to $\int_{z_a-\epsilon}^z$. Compared with Fig. 4.13, the results are significantly better when constraining the perturbation.*

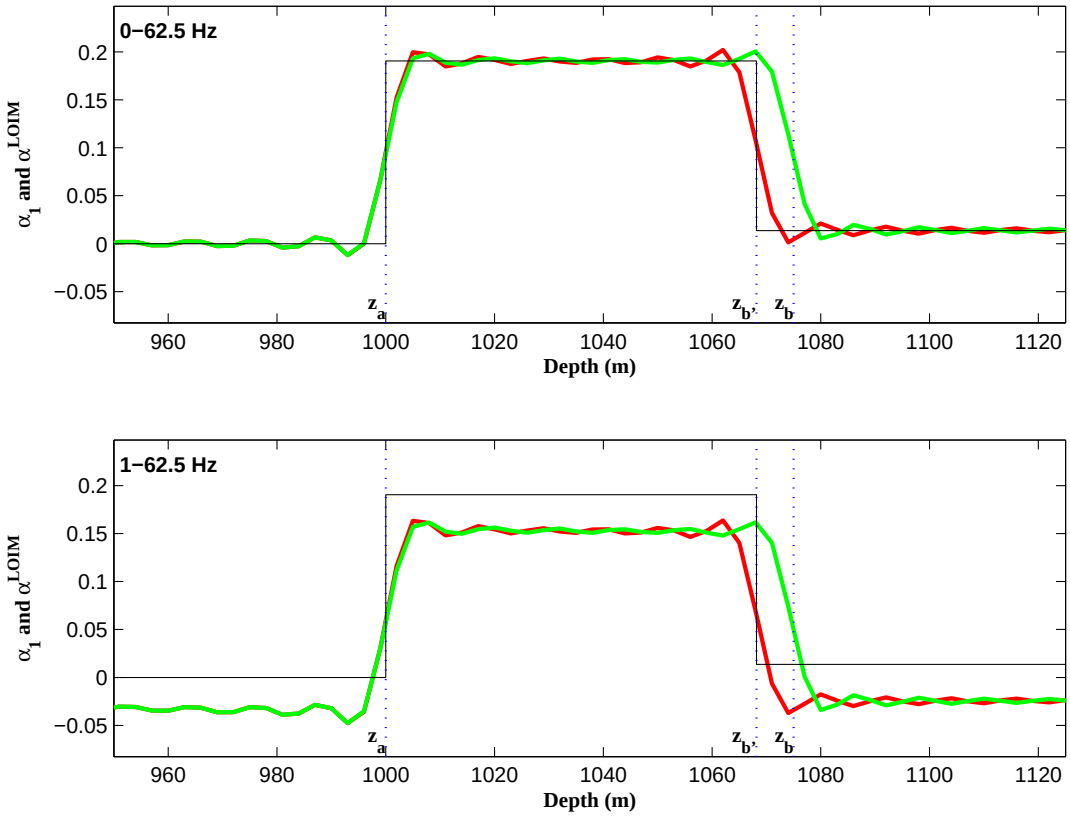

Fig. 4.16: *By truncating the integral from* $\int_0^z$ *to* $\int_{z_a-\epsilon}^z$, *the major effect of missing low frequencies on* $\alpha^{LOIS}(z)$ *(in green) is greatly mitigated. In comparison with Fig. 4.14, the mislocated reflector has been accurately located by the imaging series.*

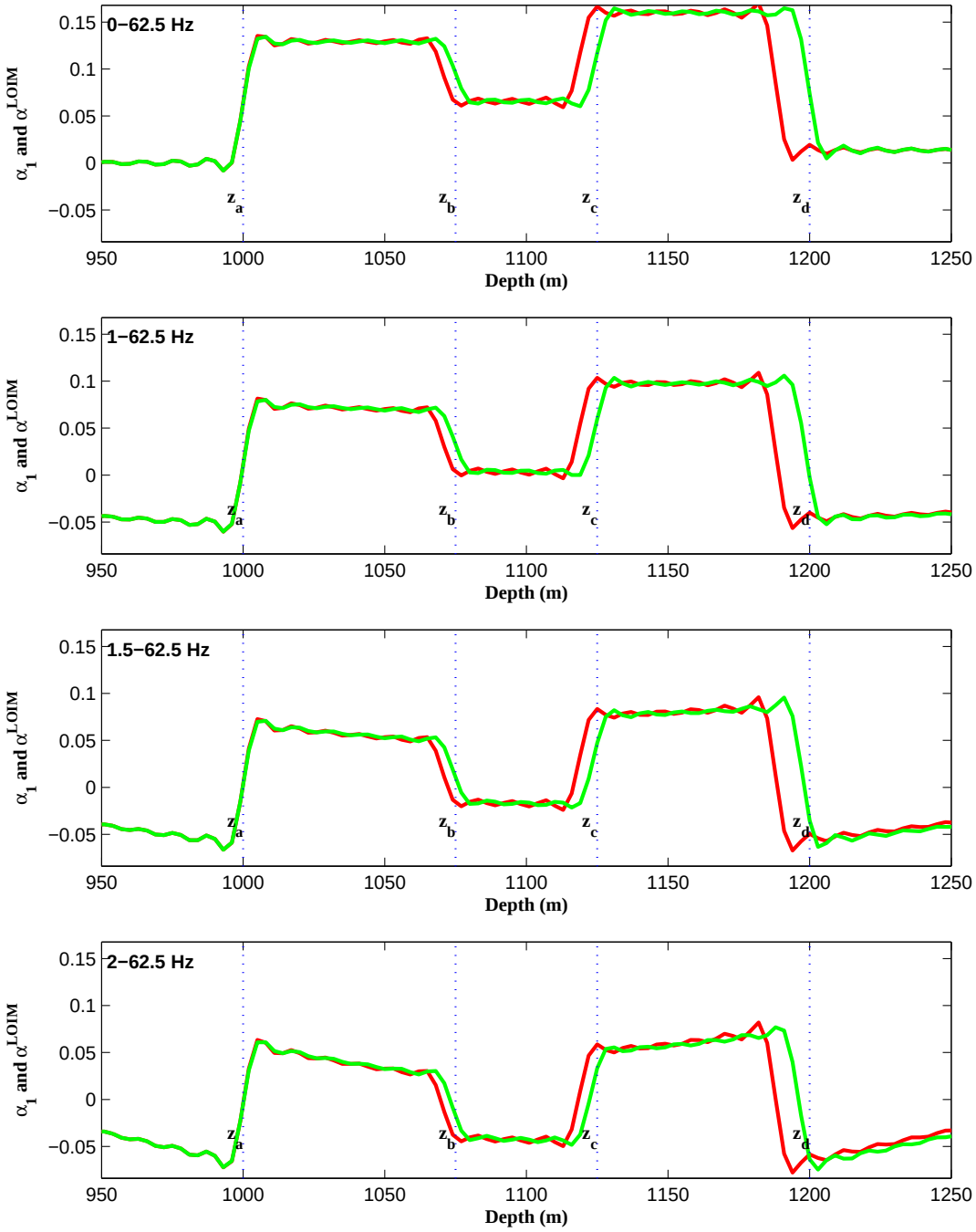

Fig. 4.17: A five-layer model comparing α_1 (in red) with α^{LOIS} (in green) for $\theta_0 = 0$ and different low frequency limits. The mislocated reflectors shift towards their true depths.

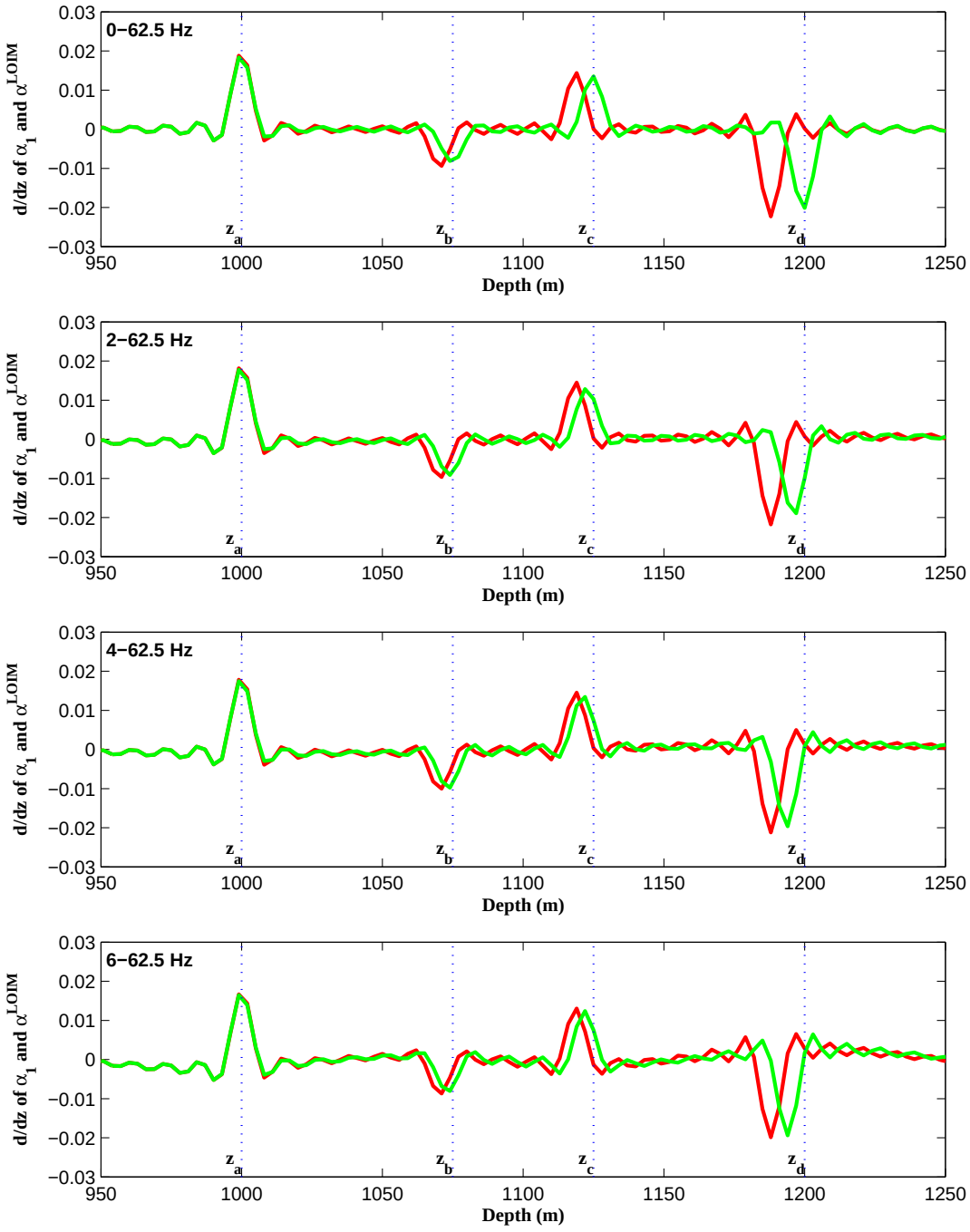

Fig. 4.18: A five-layer model comparing the derivatives with respect to z of α_1 (in red) and α^{LOIS} (in green) for $\theta_0 = 0$ and different low frequency limits. The mislocated reflectors shift towards their true depths.

show results of the leading order imaging series for a five-layer model (c_0=1500 m/sec, c_1=1600 m/sec, c_2=1550 m/sec, c_3=1625 m/sec, c_4=1510 m/sec, z_a=1000 m, z_b=1075 m, z_c=1125 m, z_d=1200 m) and a range of missing low frequencies up to 8 Hz. Figure 4.18 shows the same information as Fig. 4.17 except the derivatives with respect to z are displayed in order to more clearly identify the location of the reflectors. As demonstrated in Fig. 4.19, even after removing all information below 8 Hz (in this example), the leading order imaging series shows an improvement in the location of all reflectors. However, the accuracies of the predicted depths are better when more low frequency information is present.

Reducing the contrast between the actual and reference media is akin to having a reference velocity model that is a better estimate of the actual velocity. The effect will be apparent in the first term, α_1, because reducing the difference in the velocities means that the reflectors will be imaged closer to their true depths even before the non-linear terms are computed. This is illustrated Fig. 4.20 where the velocity contrasts of the model in the top panel (labelled "Highest contrast") have been increased by 50% over those in the middle panel (labelled "Middle contrast") which are 50% greater than those in the bottom panel (labelled "Lowest contrast"). In each case, the lower frequency limit is 4 Hz and the *proportional* correction to the depths of the mislocated reflectors is approximately the same. Therefore, an increase in contrast would seem to not be more sensitive to missing low frequencies. The obvious benefit of lower contrasts, however, is that the closer the reference velocity is to the actual velocity, the better the leading order approximation is in the imaging series *and* the faster the series algorithm will converge. This observation regarding contrast and low frequency content is relevant to the next step in our analysis, which is to consider higher angles of incidence, where the effective contrast is greater.

3.2 The effect of missing low frequency information at higher angles of incidence

As illustrated in Fig. 4.10, the degree of freedom afforded by the seismic experiment's source-receiver offset leads to a lower minimum vertical wavenumber, $(k_z)_{\min}$, in the construction of α_1 for higher angles of incidence through the relationship in Eq. (4.6)

$$(k_z)_{\min} = \frac{(\omega)_{\min}}{c_0} \cos\left[(\theta_0)_{\max}\right]. \tag{4.10}$$

There are two factors that affect the amplitude of $\alpha_1(z,p)$ as a function of angle. The first is data-driven: the magnitude of the data's amplitudes (for these acoustic models) will tend to increase with angle. The second is algorithm-driven: the computation of α_1 involves a multiplication by $\cos^2\theta_0$. The net result, illustrated in Fig. 4.21 for the first interface (where there is no transmission loss in the recorded data), is that the amplitude of $\alpha_1(z,p)$ will tend to vary only gradually with angle. However, the leading order imaging series undoes the first term's algorithmic angle dependent scalar, $\cos^2\theta_0$, because higher angles of incidence will tend to have more residual moveout that needs to be corrected (Fig. 4.22). It is the larger magnitudes of the amplitudes with higher angles (Fig. 4.21) that set about correcting the greater error in depth (Fig. 4.22) through the imaging series algorithm.

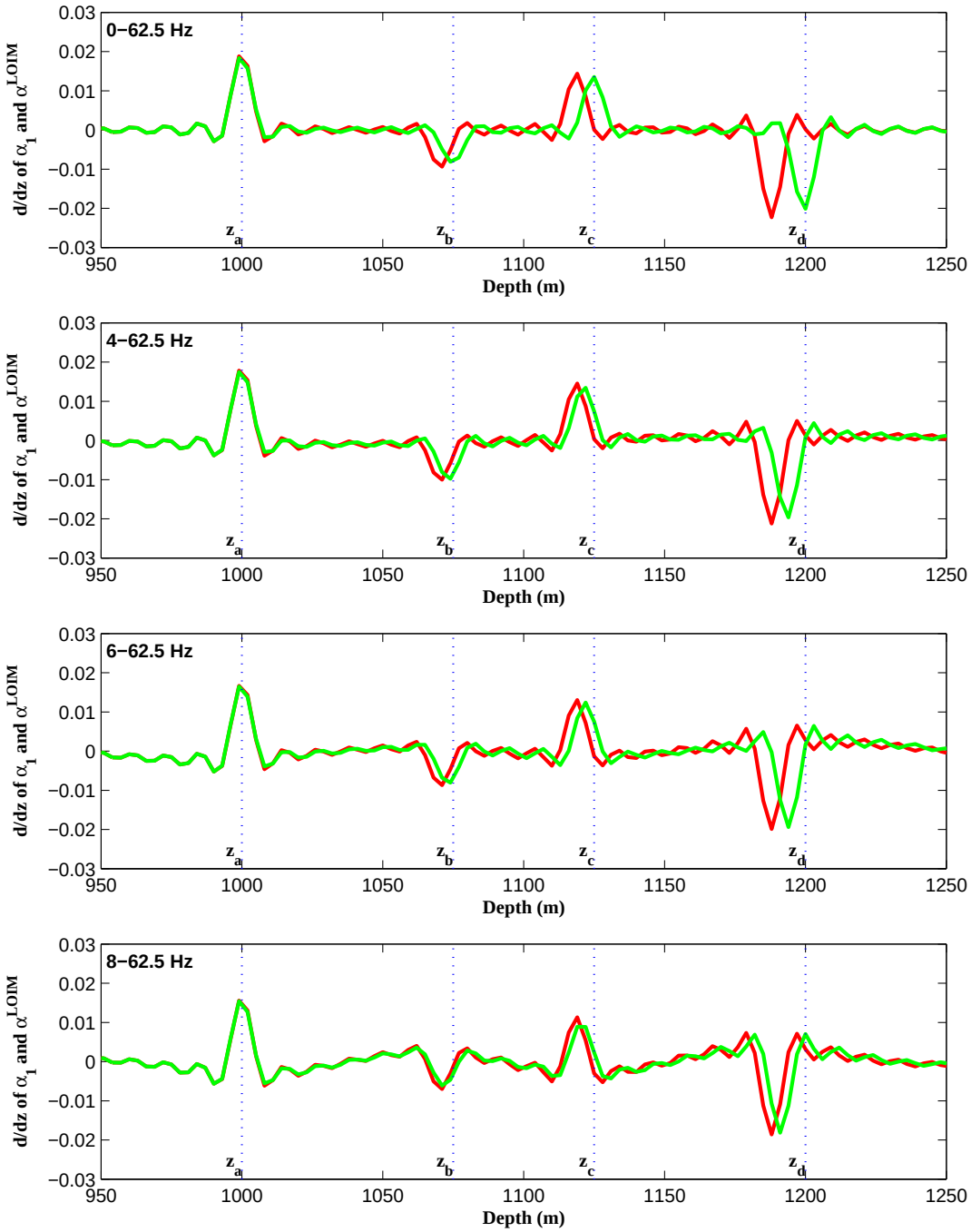

Fig. 4.19: *A five-layer model comparing the derivatives with respect to z of α_1 (in red) and α^{LOIS} (in green) for $\theta_0 = 0$ and different low frequency limits (missing up to 8 Hz). Although there is a gradual degradation of the results when more low frequency is missing, in all cases the mislocated reflectors shift towards their true depths providing an improvement over linear imaging with the reference velocity.*

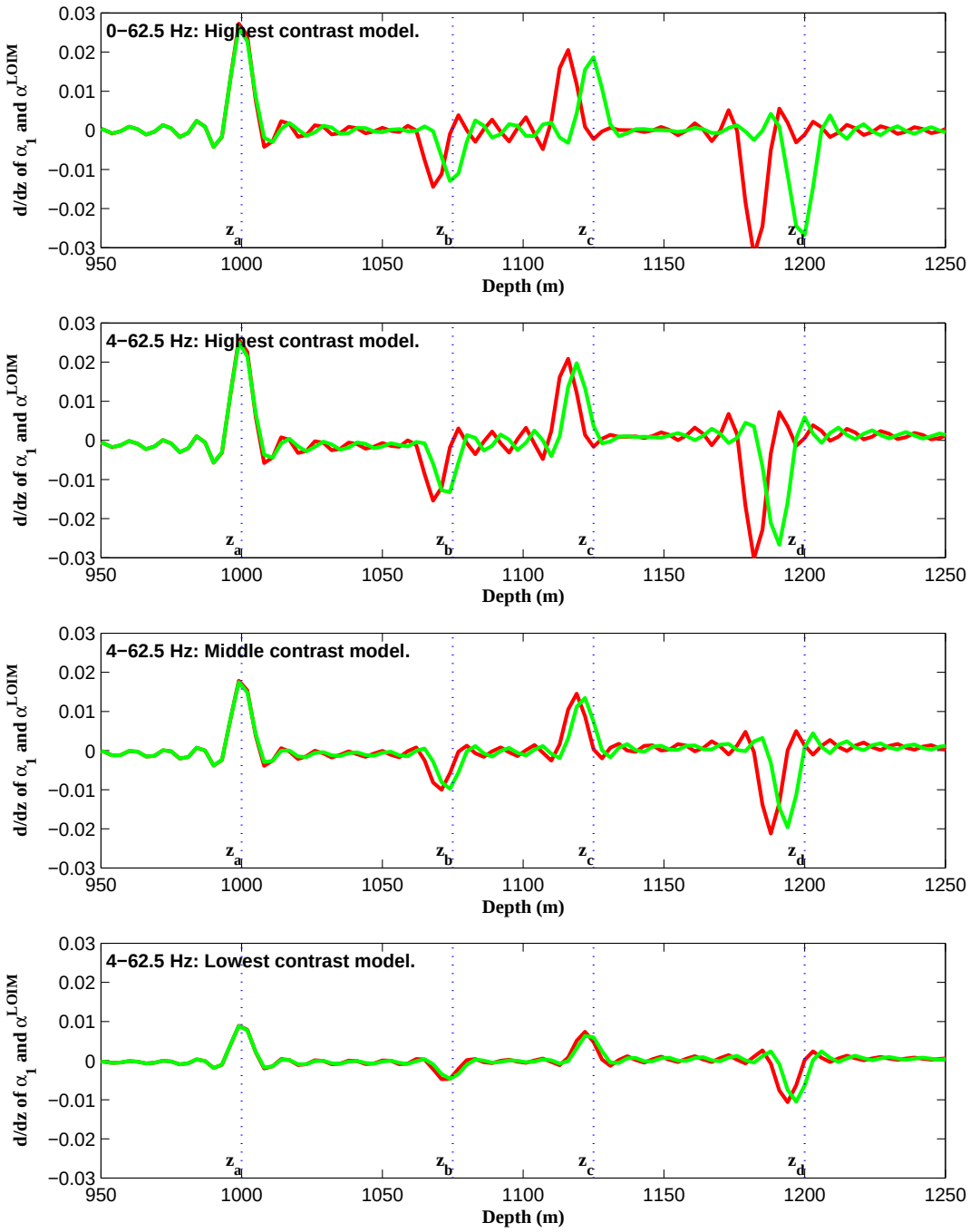

Fig. 4.20: *The effect of contrast between the actual and reference medium on the leading order imaging series for data missing low temporal frequency. A comparison of the derivatives with respect to z of α_1 (in red) and α^{LOIS} (in green) for $\theta_0 = 0$ and three different five-layer models. At top is the result for data that have all low frequencies, including zero frequency. In the other cases the low frequency limit is 4 Hz. The "middle contrast" model is the same as in Figs. 4.17–4.19 and the other two deviate from it by ±50% in their interval velocities.*

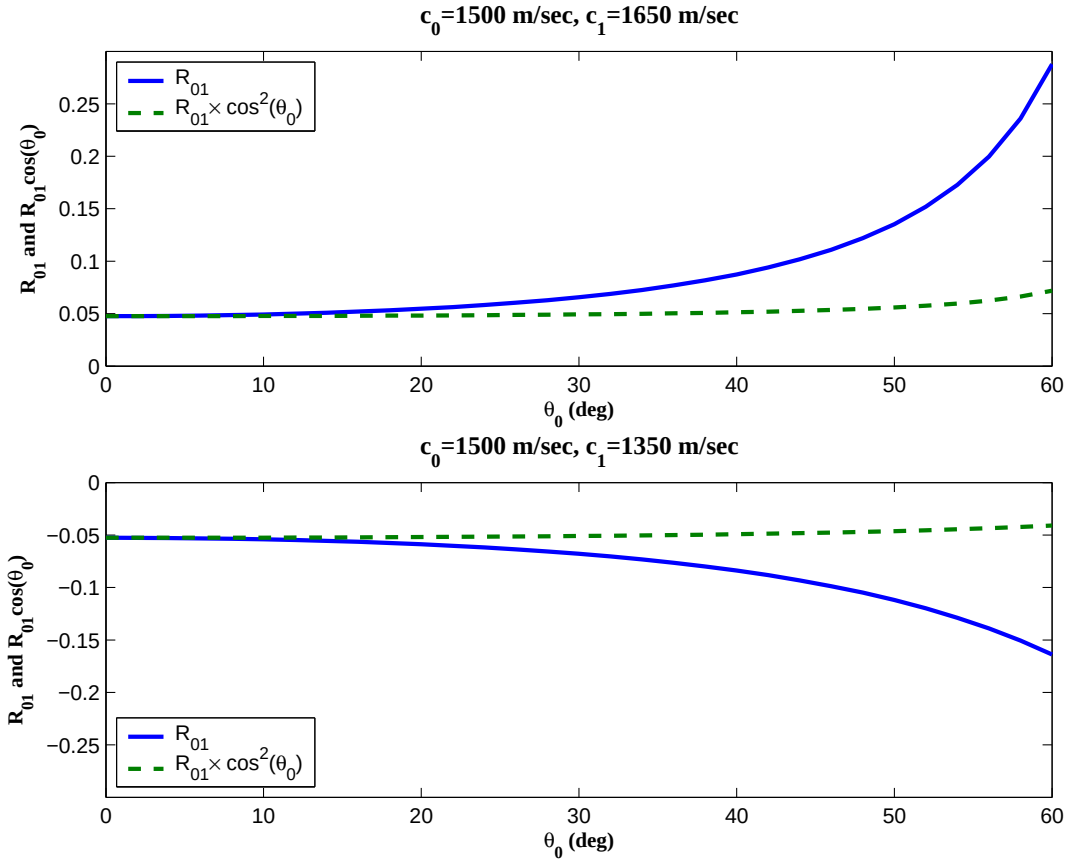

Fig. 4.21: *The variation of reflection coefficient at the first interface ($z = z_a$) as a function of angle for two different models. The first term in the inverse series, α_1, is proportional to $\cos^2\theta_0$ times the data's amplitudes. The net result is that the amplitudes in α_1 will tend to vary more gradually with angle than the amplitudes in the data.*

The relevant question in the current analysis is how does the performance of the imaging series vary with angle when low temporal frequencies are missing? The results displayed in Fig. 4.20 would suggest that the higher "effective contrast" experienced at higher angles would be neither more nor less sensitive to missing low frequencies. However, in the leading order approximation to the imaging series that is currently being studied, higher contrasts will directly impact the accuracy of the predicted depths.Specifically, the smaller the difference between the actual and reference media velocities, the more accurately the leading order imaging series will predict the precise locations of the reflectors.

Figure 4.23 demonstrates how higher angles of incidence fill in the low end of the k_z spectrum for 4−62.5 Hz bandlimited input data. At $\theta_0 = 0°$, the k_z spectrum derives no additional benefit at the low end in the sense that the $(k_z)_{\min}$ is equal to $(\omega)_{\min}/c_0$. However, at $\theta_0 = 45°$, $(k_z)_{\min}$ is reduced by the factor $\cos\theta_0$ and is equivalent to 2.8 Hz (as opposed to 4 Hz) at normal incidence. At higher angles, there is more residual moveout to be corrected

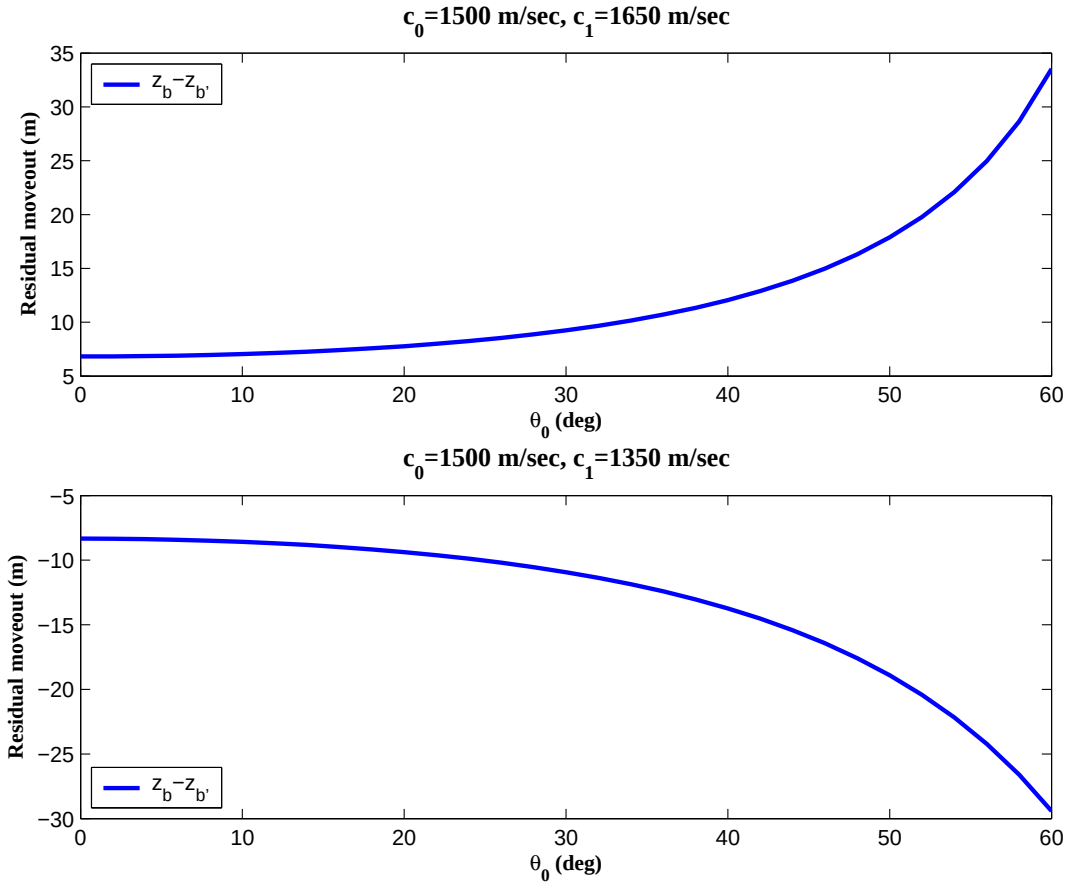

Fig. 4.22: *The residual moveout for two different models corresponding to Fig. 4.21. z_b is the actual depth of a reflector and $z_{b'}$ is its depth predicted by the first term in the imaging series (i.e., through a conventional migration).*

for the nonlinear imaging terms.

Figure 4.24 shows results of the imaging series, for a fixed angle of incidence ($\theta_0 = 45°$), and a range of minimum temporal frequencies. It is encouraging to see that the difference in the predicted depths for $f_{\min} = 0.125$ Hz and $f_{\min} = 2$ Hz are extremely close and there are improvements over the first term for all cases where information below at least 6 Hz is missing.

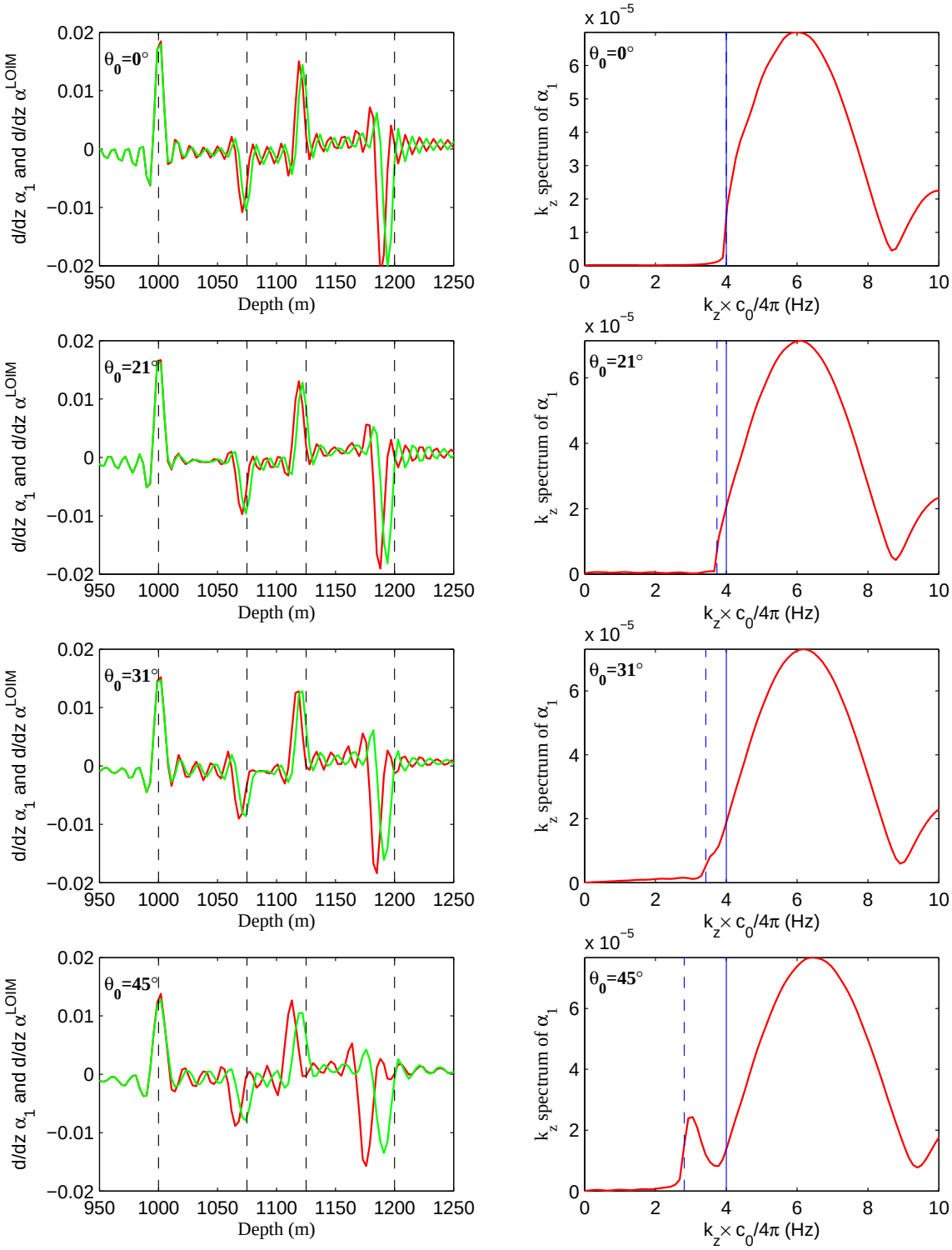

Fig. 4.23: Filling in the low end of the k_z spectrum according to Eq. (4.6) for 4−62.5 Hz bandlimited input data. A comparison, for four different angles of incidence, of α_1, (in red) and α^{LOIS} (in green) and the k_z spectrum of α_1 in each instance (on right).

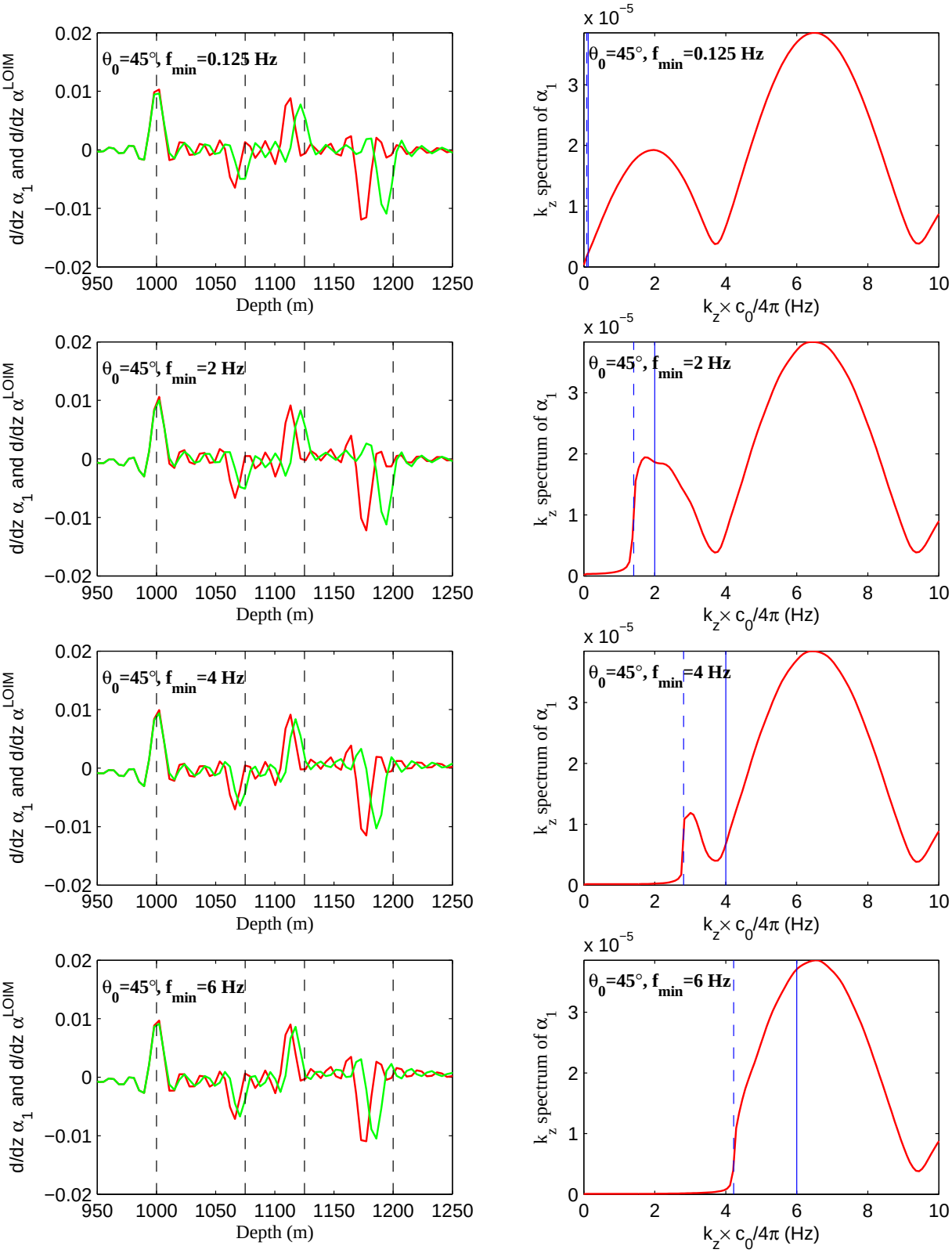

Fig. 4.24: A comparison of α_1 (in red) and α^{LOIS} (in green) and the k_z spectrum of α_1 (on right) for four different low frequency limits. The filling in of the low end of the k_z spectrum according to Eq. (4.6) is apparent. The difference in the depths predicted by the imaging series when having down to 0.125 Hz (top) and only having down to 2 Hz (second from top) is hardly noticeable.

In Fig. 4.25, the effect of missing low frequency on the prestack leading order imaging series is demonstrated on angle gathers over a range of precritical angles. While a gradual deterioration in effectiveness is evident as more low frequency information is removed, in all cases (at least up to $f_{\min} = 4$ Hz) for this example, the results of the imaging series are an improvement over current imaging with the reference velocity (i.e., the depths are more accurate than those predicted by the first term in the series).

It is interesting to consider whether the low k_z information at high angles can be transplanted to low angles of incidence to improve the performance of the leading order imaging series in the latter range. Figure 4.26 shows the effect of transplanting the low end of the k_z amplitude spectrum from $\alpha_1(z, \theta_0 = 50^\circ)$ to the normal incidence trace, $\alpha_1(z, \theta_0 = 0^\circ)$ over the range that it is missing and then computing the leading order imaging series. A small improvement in the location of the deepest reflector is noticeable. This procedure resembles the alternative parameterization discussed earlier in which we can choose to keep omega constant and sum of angles to compute each term in the series, thereby collecting high angle information for each estimate of α^{LOIS}. This parameterization and procedure require further investigation.

4 Discussion

Analysis of the leading order imaging series algorithm for a 1-D acoustic earth that varies only in the z-direction, would suggest that low frequency information is important to its effectiveness because of its integral with respect to z. However, the limits of the integral are the reason why the algorithm can tolerate missing low frequencies while still providing benefit. The algorithm does not call for

$$\int_{-\infty}^{+\infty} \alpha_1(z')dz' \tag{4.11}$$

which is exactly the zero frequency component of the data. We have investigated procedures for improving the actual integral

$$\int_{0}^{z} \alpha_1(z')dz' \tag{4.12}$$

which collects the amplitude and moveout information in the overburden and acts to shift the mislocated reflectors towards their true locations in depth. One effective procedure that improves the accuracy of this integral derives from recognizing that the perturbation is before the onset of a reflector (say, at depth z_a). Redefining the integral to be

$$\int_{z_a-\epsilon}^{z} \alpha_1(z')dz' \tag{4.13}$$

significantly improves the results of the leading order imaging series when low frequencies are missing. To implement this causality-like condition, the first reflector could be automatically

picked or else, if we had a good estimate of the medium velocity down to the onset of an unknown, or less well-defined, medium (see, e.g., Fig. 4.27), we could build that into the reference medium and begin the imaging series at some depth below the subsurface.

The importance of low frequency information to the accuracy of the leading order imaging series motivates the study of methods for spectral extrapolation (Walker and Ulrych, 1983; Innanen et al., 2004). Larger angles of incidence and the concomitant lower k_z information is also expected to improve the accuracy of the depths predicted by the imaging series. We note that trends in seismic data acquisition are towards the recording of lower frequencies. This is a welcome development as these and other new methods are developed that make full use of the recorded data's frequency spectrum.

5 Conclusion

We have demonstrated using reflectivity data in the precritical regime for a 1-D acoustic medium and 3-D wave propagation, that the leading order imaging series retains effectiveness, even when the input data are absent zero and low frequency information. This finding is critically important in the progression to a practical algorithm ready for application to field data. These conclusions merit the generalization to a multidimensional earth (Liu et al., 2004) and more complex wave equations (Zhang and Weglein, 2004a). The imaging of primaries at higher angles, especially in the post-critical regime is also of keen interest (Nita et al., 2004).

The imaging series is shown to benefit from having lower frequency information, in that reflectors will tend to move closer to their true depths than if the low frequency information is absent. Therefore, current trends towards acquiring lower frequency data, as well as existing and new methods for extrapolating this information will both be important to the practical implementation of the imaging series.

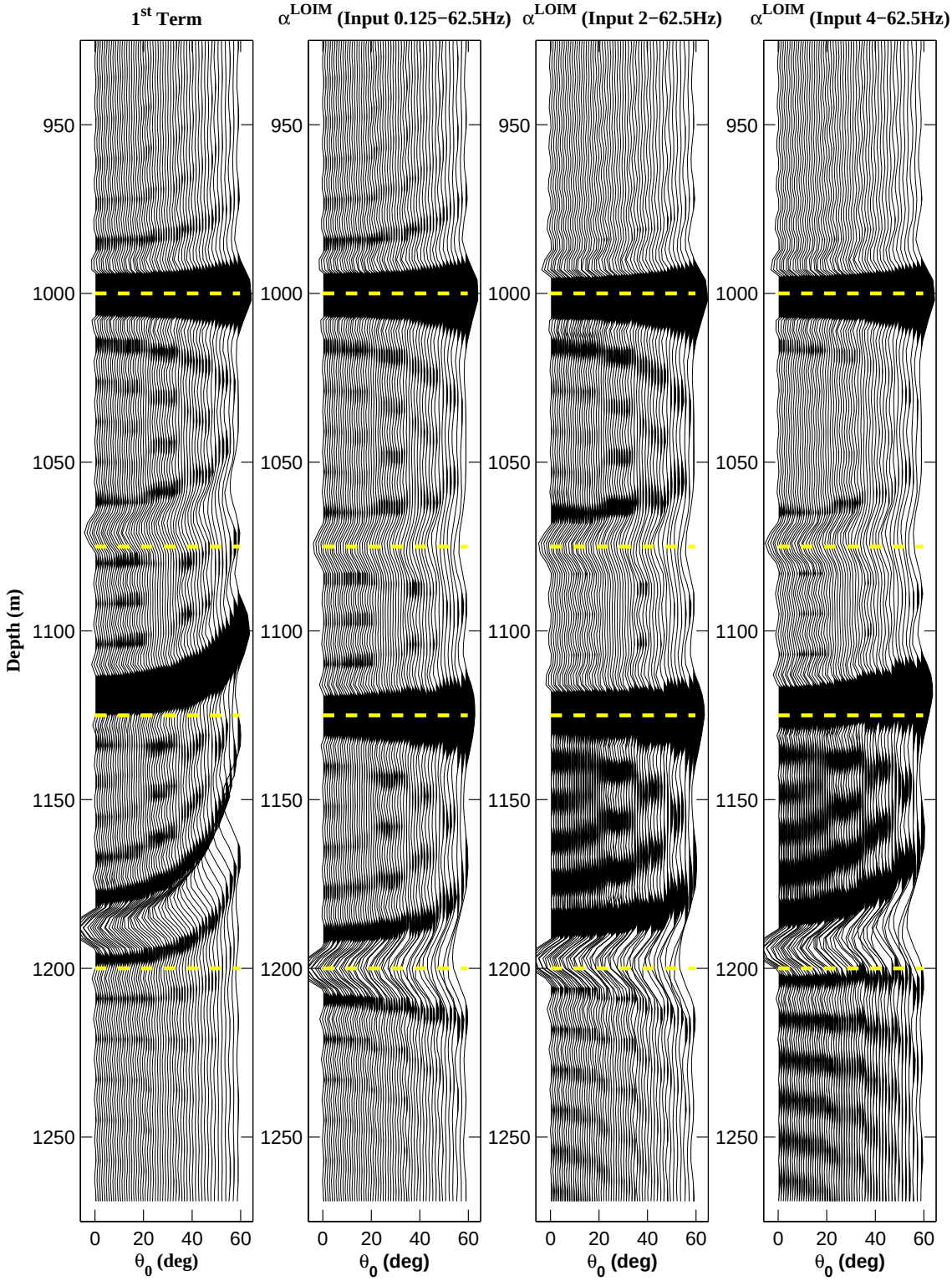

Fig. 4.25: *Prestack leading order imaging series for different low frequency limits. The left panel is the first term in the series and the other three panels are the leading order imaging series results. As more low frequency information is removed, the leading order imaging series results deteriorate but, in all cases, the results are an improvement over the first term.*

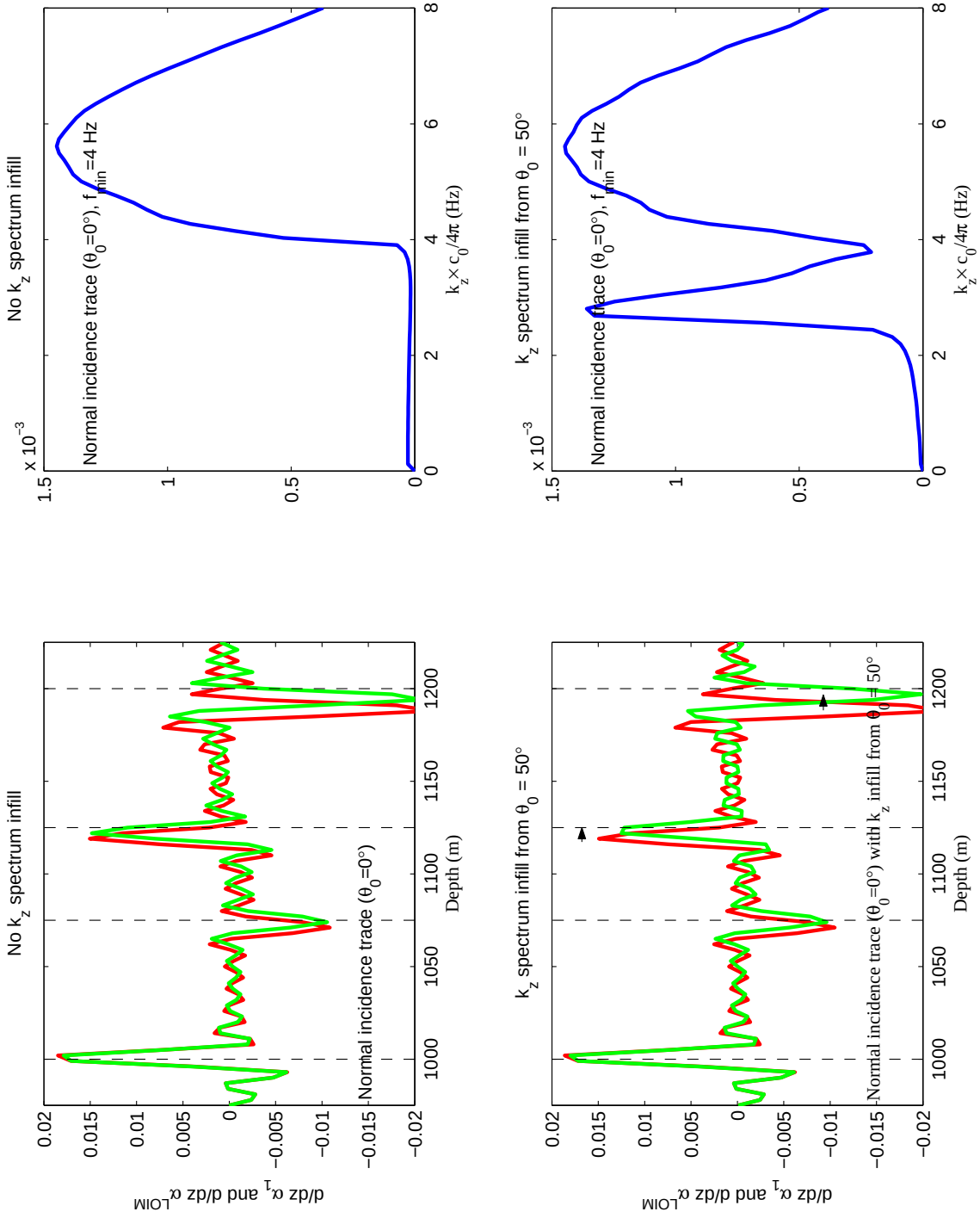

Fig. 4.26: *The effect of transplanting low k_z information from the trace at 50° to the normal incidence trace for 4−62.5 Hz bandlimited input data. A small improvement is noticeable at the deepest reflector.*

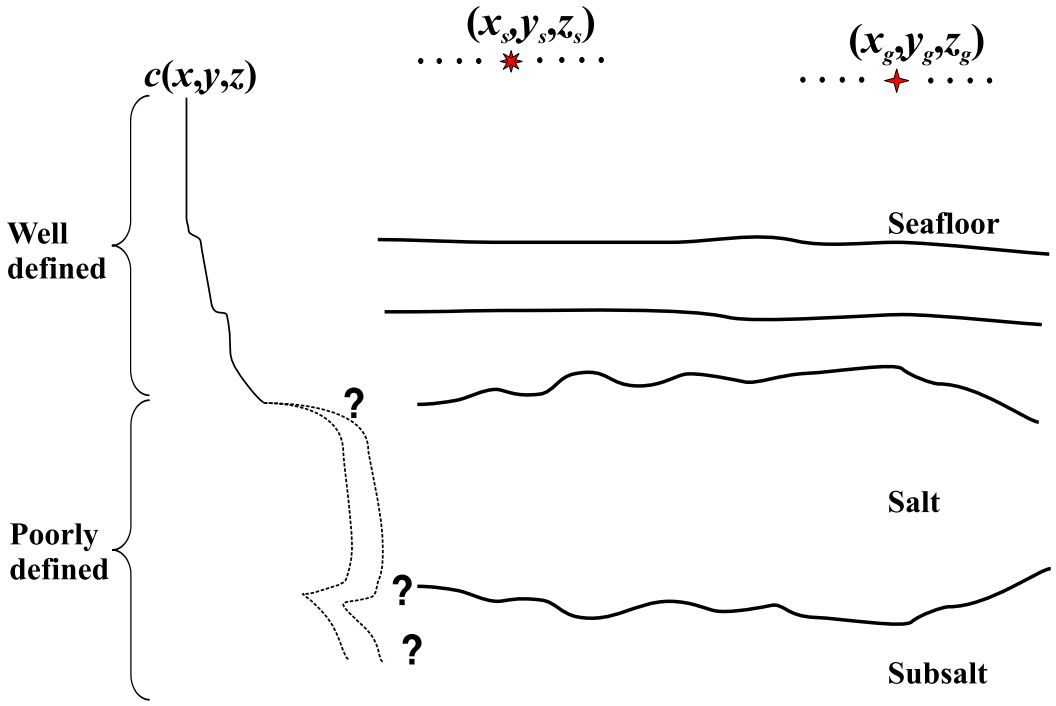

Fig. 4.27: *The problem of subsalt imaging is sometimes described as a combination of complex, rugose top and bottom of salt and weak reflectivity below salt. The velocity down to the top of salt can often be adequately estimated using conventional velocity analysis techniques.*

5. HIGHER ORDER IMAGING TERMS, EXTENSIONS TO A VARIABLE BACKGROUND AND MORE COMPLEX WAVE PROPAGATION

We have isolated an imaging series for the simplest acoustic model, and demonstrated that it improves the predicted depths of reflectors over conventional imaging with the reference velocity even when the input data are frequency bandlimited.

In this last chapter, we address some of the limitations of the current form of the algorithm. Firstly, the leading order imaging series is an approximation to the full imaging potential of the inverse series. Secondly, the homogeneous reference velocity does not represent the current best-practice linear depth imaging algorithms, which can accommodate velocities that vary vertically and laterally. Lastly, a 1-D constant density acoustic model is far from a 3-D viscoelastic medium that almost certainly better describes the actual Earth.

1 Higher order imaging terms

For the problem considered in this thesis, in which the Earth is characterized by a single parameter, the imaging series is written

$$\alpha^{\mathrm{IS}} = \alpha_1 + \alpha_2^{\mathrm{IS}} + \alpha_3^{\mathrm{IS}} + \dots \tag{5.1}$$

where α_i^{IS} is the term in the imaging series that is i^{th} order in the scattered field and is found in the i^{th} term of the inverse series. The leading order imaging series, α^{LOIS}, is the contribution to the imaging series that is leading order in the scattered field:

$$\alpha^{\mathrm{LOIS}} = \alpha_1 + \alpha_2^{\mathrm{LOIS}} + \alpha_3^{\mathrm{LOIS}} + \dots \tag{5.2}$$

where

$$\alpha_i^{\mathrm{LOIS}} \approx \alpha_i^{\mathrm{IS}}.$$

The extent to which the leading order imaging series, α^{LOIS}, is a good approximation to the entire imaging series, α^{IS}, depends on the magnitude of the velocity perturbation above the reflector being imaged. Higher order imaging series that go beyond the leading order

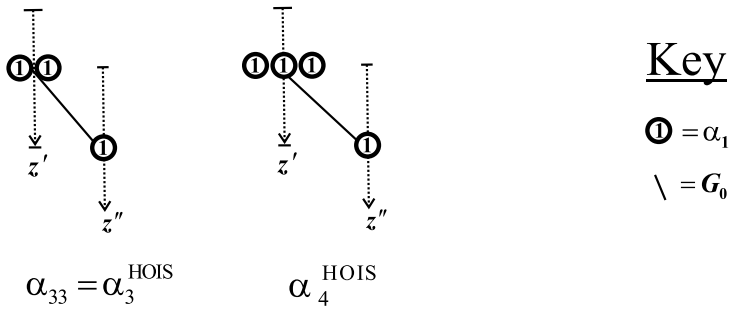

Fig. 5.1: *Higher order imaging components from the third and fourth terms in the inverse series.*

approximation include successively more amplitude terms in the geometric series for the coefficients of the Taylor series that shift the mislocated reflectors. For example, for the second interface the shift is (see Eq. 3.34)

$$(z_b - \hat{z}_b) = -2(\hat{z}_b - z_a)[R_{01}(p) + R_{01}^2(p) + R_{01}^3(p) + \ldots] \tag{5.3}$$

and the leading order imaging series reproduces on the leading order approximation to this shift. For models containing more than two interfaces, the leading order imaging series produces an approximation to the shift at each mislocated interface that is an infinite series in reflection *and transmission* coefficients in the overburden. It is postulated that higher terms in the imaging series will act to unravel these transmission coefficients.

Figure 5.1 (left) illustrates the inverse scattering diagram corresponding to the higher order imaging component of the third term in the inverse series. This term is written mathematically as (see Eq. 3.28)

$$\alpha_{33}(z,p) = \frac{-1}{8\cos^4\theta_0}\left[\int_0^z \alpha_1^2(z',p)dz'\right]\frac{\partial\alpha_1(z,p)}{\partial z}. \tag{5.4}$$

We observe that higher order imaging terms are "mixed task" terms because they contain both separated and self-interaction diagram components. The self-interaction component (above the output point) serves to non-linearly invert the overburden by going further into the series.

For the reflector mislocated at $\hat{z}_b$ by the first term, this portion of α_3 reproduces the expected second order coefficient in Eq. (5.3):

$$\alpha_{33}(z,p) = 8\cos^2\theta_0 R_{01}^2(p)\hat{R}_{12}(p)(z - z_a)H(z - z_a)\delta(z - \hat{z}_b). \tag{5.5}$$

This follows the first order term found in α_2 (Eq. 3.26):

$$\alpha_{22}(z,p) = 8\cos^2\theta_0 R_{01}(p)\hat{R}_{12}(p)(z - z_a)H(z - z_a)\delta(z - \hat{z}_b). \tag{5.6}$$

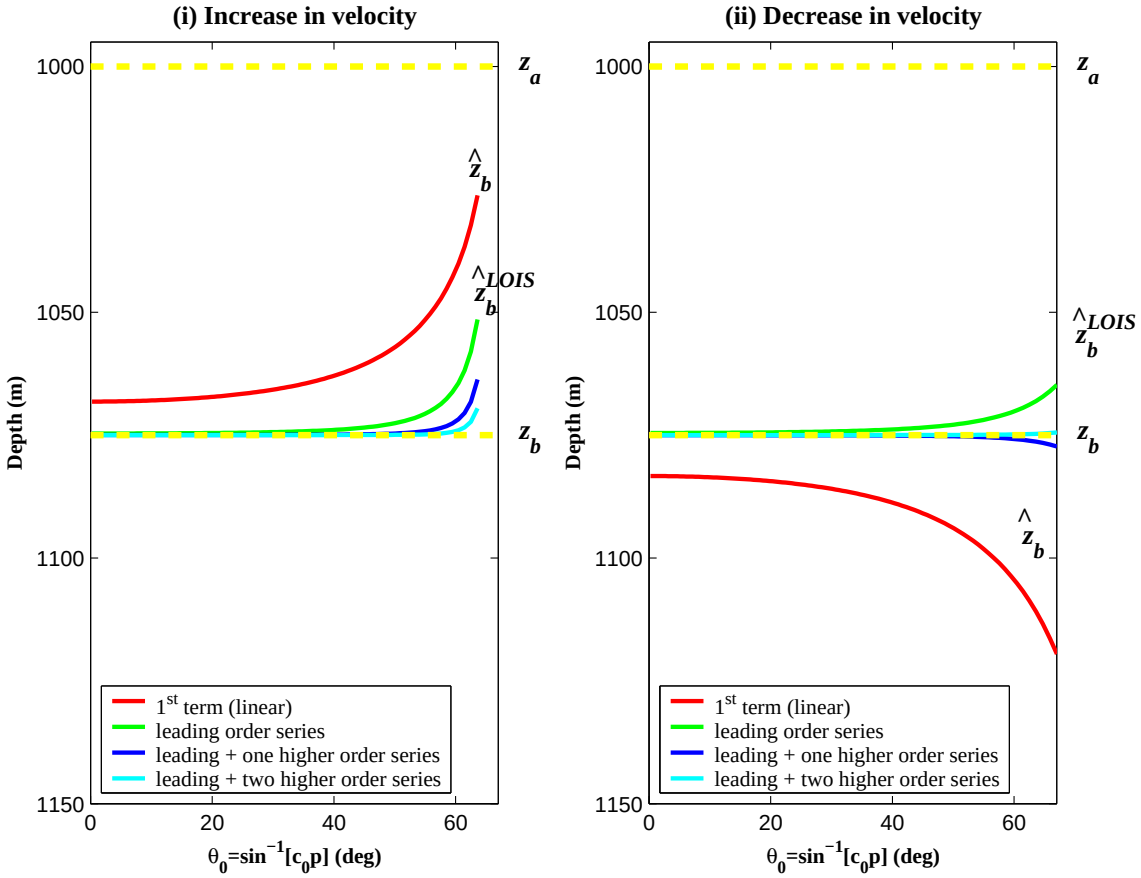

Fig. 5.2: Low contrast analytic example. Depths predicted by the first term in the series and three different imaging series as a function of angle for two specific examples: $z_a = 1000$ m, $z_b = 1075$ m, $c_0 = 1500$ m/sec and $c_1 = 1650$ m/s (i), $c_1 = 1350$ m/sec (ii).

Combining the leading and next higher order term, we have

$$\alpha_{22}(z,p) + \alpha_{33}(z,p) = \underbrace{-2(\hat{z}_b - z_a)\left[R_{01}(p) + R_{01}^2(p)\right]}\times 4\cos^2\theta_0 \hat{R}_{12}(p)\delta(z-\hat{z}_b) \qquad (5.7)$$

where the bracketed portion of Eq. (5.7) corresponds to the first two terms in Eq. (5.3). These are the leading order term and one higher order term, respectively.

Consider two specific examples where the reference velocity $c_0 = 1500$ m/sec and the two reflectors are located at $z_a = 1000$ m and $z_b = 1075$ m. In the first case $c_1 = 1650$ m/sec and in the second case $c_1 = 1350$ m/sec. Figure 5.2 illustrates the depths predicted by the first term in the series and three approximations to the imaging series for two different velocity models. The variation of $z_{b'}$ with angle is the residual moveout. At higher angles, the depth of the second reflector predicted by the first term in the series is less accurate. This is because the constituent plane waves travelling at higher angles of incidence spend a proportionally longer time in the layer with the wrong velocity. Therefore, the non-linear

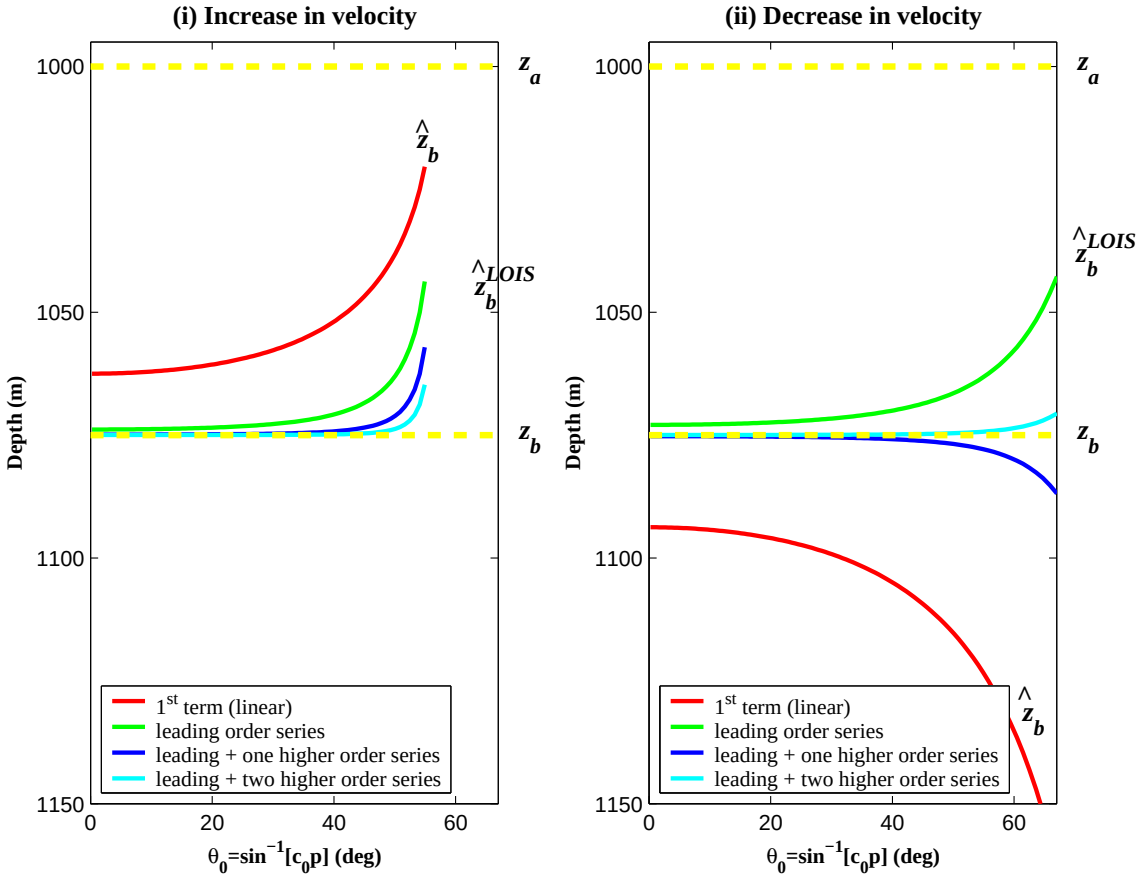

Fig. 5.3: *High contrast analytic example. Depths predicted by the first term in the series and three different imaging series as a function of angle for two specific examples:* $z_a = 1000$ *m,* $z_b = 1075$ *m,* $c_0 = 1500$ *m/sec and* $c_1 = 1800$ *m/sec (i),* $c_1 = 1200$ *m/sec (ii).*

terms in the imaging series have to shift the interface further at higher angles. The fact that the magnitude of the reflection coefficient at the first interface, $|R_{01}|$, increases with angle aids the imaging terms in shifting greater distances with angle. On the other hand, this increase in amplitude will tend to make the leading order approximation in Eq. (3.60) less justifiable. Figure 5.2 shows, for two examples, that including higher order imaging terms improves the accuracy of the predicted depth, especially at higher angles where they are needed more. Figure 5.3 shows two more examples where the contrasts are twice as large as in Fig. 5.2. These examples show how higher order imaging terms become more important for higher contrasts between the actual and reference velocity.

2 Extension to a variable background

There are two important advantages to formulating the leading order imaging series for a reference medium that may vary in one or more dimensions. First, if a closed form of the imaging series does not exist in multi-D, then there is a computational advantage to reformulating the series algorithm for a reference medium in which the background velocity varies spatially. We have seen that for a constant reference velocity, the rate of convergence is greater for actual velocity models that deviate less from this constant background. For realistic earth models in which there may be large and/or rapid velocity variations in the velocity, an imaging series algorithm formulated for a constant reference may turn out to be prohibitively expensive to compute.

The second advantage to formulating the leading order imaging series to accommodate a variable background velocity is in the accuracy of the leading order approximation. For either the series or the closed form, the depths predicted by the leading order imaging series will be more accurate for smaller cumulative differences between the actual and reference media.

In practice, velocity analysis could be used to estimate the actual velocity trend which would more accurately locate reflectors in the first term, and would also subsequently improve the rate of convergence and the accuracy of the leading order imaging series.

For a 1-D normal incidence experiment, we may formulate the inverse problem using a reference medium whose velocity varies with depth (e.g., Clayton and Stolt, 1981; Foster and Carrion, 1984). In this case, the perturbation, α, is related to the actual velocity, c, through the reference velocity, c_0, by

$$\frac{1}{c^2(z)} = \frac{1}{c_0^2(z)}[1 + \alpha(z)]. \tag{5.8}$$

We choose a WKBJ form of the reference Green's function, which in 1-D is (e.g., Liu and Weglein, 2003)

$$G_0(z|z';\omega) = \frac{\sqrt{c_0(z)c_0(z')}}{2i\omega} e^{i\omega|\int_{z'}^{z} \frac{d\zeta}{c_0(\zeta)}|}. \tag{5.9}$$

We observe that the amplitude of this wave is a function of the reference velocity, c_0, at the depth of the source, z', and at the evaluation depth, z. Using the one-dimensional form of Eq. (3.6), we have

$$\begin{aligned} D(z_g = 0|z_s = 0;\omega) &= \int_{-\infty}^{+\infty} G_0(z_g = 0|z';\omega)\frac{\omega^2}{c_0^2(z')}\alpha_1(z')G_0(z'|z_s = 0;\omega)dz' \\ &= \frac{-c_0(0)}{4}\int_{-\infty}^{+\infty} \frac{\alpha_1(z')}{c_0(z')} e^{2i\omega|\int_0^{z'} \frac{d\zeta}{c_0(\zeta)}|} dz'. \end{aligned} \tag{5.10}$$

Strictly speaking, the scattered field, D, is different from the constant velocity reference case since the reference wavefield, G_0 now has a spatially varying amplitude. Solving for $\alpha_1(z)$ through an inverse Fourier transform yields

$$\alpha_1(z) = -8\frac{c_0(z)}{c_0(0)}D(\tau). \tag{5.11}$$

where

$$\tau(z) = 2\int_0^z \frac{d\zeta}{c_0(\zeta)}. \tag{5.12}$$

In contrast to the constant reference velocity case, the phase of α_1 is now a function of the integral of the reference velocity and the amplitude is weighted by the ratio $c_0(z)/c_0(0)$.

Solving for the second term in the inverse series using the same WKBJ Green function yields

$$\alpha_2(z) = -\frac{1}{2}\ldots \tag{5.13}$$

By analogy with the constant reference case, the variable background leading order imaging series can be shown to be

$$\alpha^{\text{LOIS}}(z) = \sum_{n=0}^{\infty} \frac{(1/2)^n (c_0(0))^n}{n!} \left[\int_0^z \frac{\alpha_1(z')}{c_0(z')}dz'\right]^n \frac{\partial^n \alpha_1(z)}{\partial z^n} \tag{5.14}$$

where the first term, α_1, is computed via Eq. (5.11). Clearly Eq. (5.14) also has a closed form which is (see the derivation of Eq. 3.43):

$$\alpha^{\text{LOIS}}(z) = \alpha_1\left(z - \Delta\left(z\right)\right) \tag{5.15}$$

where the vertical shift is computed via

$$\Delta(z) = \frac{c_0(z)}{2}\int_0^z \frac{\alpha_1(z')}{c_0(z')}dz'. \tag{5.16}$$

Keys (2003) arrived at this same formula by comparing the constant-background velocity leading order imaging series with the variable-background velocity forward scattering series to recursively construct the variable-background leading order imaging series. As might be expected, Eqs. (5.14) and (5.15) reduce to the constant velocity background formulae when $c_0(z) = c_0(0)$. They are also straightforwardly generalized to the situation where we have pre-stack input data and we choose horizontal slowness, p, as a parameter.

More here.

3 Model-type dependence

As it stands, the current formulation of the leading order imaging series is restricted to a constant density acoustic model. Furthermore, the algorithm outputs outputs an imaged parameter (actually an estimate of a parameter: α_1), rather than a data-like quantity. If we consider the current derivation as a simple blueprint for deriving an algorithm applicable to more complex multi-parameter (e.g., velocity, bulk modulus, shear modulus, etc.) model types, then we would arrive at multiple imaging formulae – one for each of these parameters. This is in contrast to conventional imaging algorithms that output data-like image gathers which are then input to an inversion procedure to estimate the parameters. An algorithm that images parameters in space is certainly a model-type dependent algorithm because we need to specify the model type in order to know which parameters to image. This approach involves a dissection of the perturbation operator, which in Chapters 3 and 4, was simply $V = k_0^2\alpha$.

The advantage of deriving an algorithm that does not require the explicit description of the perturbation operator is that it will be model-type independent and therefore will be applicable to a wide class of model types. The free surface multiple removal and internal multiple attenuation subseries are examples of model-type independent algorithms. Task-separation based on inverse scattering diagrams is transferable from the single acoustic parameter to a more general operator as discussed by Weglein et al. (2003). We may surmise that the self-interaction and separated diagram components play the same role in inversion as for the specific one parameter acoustic case. This logic held true for the earlier generalization of the free-surface and internal multiple attenuation algorithms derived from the inverse series.

In the imaging case, an alternative approach is to investigate model-type independent imaging. More here.

REFERENCES

Abma, R., W. H. McLain, S. Michell, M. N. Kabir, K. H. Matson, and S. A. Shaw (2002). Comparisons of adaptive subtraction techniques for multiple attenuation. In *72nd Ann. Internat. Mtg: Soc. of Expl. Geophys., Expanded Abstracts*, pp. 2186–2189. Soc. Expl. Geophys.

Aki, K. and P. G. Richards (2002). *Quantitative Seismology* (2nd ed.). University Science Books.

Araújo, F. V. (1994). *Linear and non-linear methods derived from scattering theory: backscattered tomography and internal multiple attenuation*. Ph. D. thesis, Universidade Federal da Bahia.

Baysal, E., D. D. Kosloff, and J. W. C. Sherwood (1983). Reverse time migration. *Geophysics 48*, 1514–1524.

Bergler, S., J. Mann, G. Hoecht, and P. Hubral (2002). The finite-offset CRS stack: an alternative stacking tool for subsalt imaging. In *72nd Annual Internat. Mtg., Soc. Expl. Geophys., Expanded Abstracts*, pp. 2058–2061. Soc. Expl. Geophys.

Berkhout, A. J. (1985). *Seismic Migration: Theoretical Aspects*. Elsevier Publishing Co.

Berkhout, A. J. and D. J. Verschuur (2001). Velocity independent seismic imaging. In *71st Annual Internat. Mtg., Soc. Expl. Geophys., Expanded Abstracts*, pp. 897–900. Soc. Expl. Geophys.

Berkovitch, A. and B. Gelchinsky (1989). Inversion of common reflecting element (CRE) data (migration combined with interval velocity determination). In *59th Annual Internat. Mtg., Soc. Expl. Geophys., Expanded Abstracts*, pp. 1250. Soc. Expl. Geophys.

Bleistein, N. (1984). *Mathematical methods for wave phenomena*. Academic Press.

Bleistein, N., J. K. Cohen, and J. W. Stockwell (2000). *Mathematics of multidimensional seismic imaging, migration and inversion*. Springer-Verlag.

Carvalho, P. M. (1992). *Free-surface multiple reflection elimination method based on non-linear inversion of seismic data*. Ph. D. thesis, Universidade Federal da Bahia.

Carvalho, P. M. and A. B. Weglein (1994). Wavelet estimation for surface multiple attenuation using a simulated annealing algorithm. In *64th Ann. Internat. Mtg: Soc. of Expl. Geophys., Expanded Abstracts*, pp. 1481–1484. Soc. Expl. Geophys.

Carvalho, P. M., A. B. Weglein, and R. H. Stolt (1991). Examples of a nonlinear inversion method based on the t matrix of scattering theory: Application to multiple suppression. In *61st Ann. Internat. Mtg: Soc. of Expl. Geophys., Expanded Abstracts*, pp. 1319–1322. Soc. Expl. Geophys.

Claerbout, J. F. (1971). Toward a unified theory of reflector mapping. *Geophysics 36*(3), 467–481.

Claerbout, J. F. (1985). *Imaging the Earth's Interior*. Blackwell Science Inc.

Clayton, R. W. and R. H. Stolt (1981). A Born-WKBJ inversion method for acoustic reflection data. *Geophysics 46*(11), 1559–1567.

Corrêa, G. J. P., M. Spiegelman, S. Carbotte, and J. C. Mutter (2002). Centered and staggered Fourier derivatives and Hilbert transforms. *Geophysics 67*(5), 1558–1563.

DeSanto, J. A. (1992). *Scalar Wave Theory: Green's Functions and Applications*. Springer-Verlag.

Esmersoy, C. and M. Oristaglio (1988). Reverse time wavefield extrapolation, imaging and inversion. *Geophysics 53*(07), 920–931.

Ewing, W. M., W. S. Jardetzky, and F. Press (1957). *Elastic waves in layered media*. McGraw-Hill Book Co.

Foster, D. J. (2000). Notes on a 1-D acoustic inverse series. Personal Communication.

Foster, D. J. and P. M. Carrion (1984). Born inversion with a variable background velocity (short note). *Geophysics 49*, 1794–1797.

French, W. S. (1974). Two-dimensional and three-dimensional migration of model-experiment reflection profiles. *Geophysics 39*(03), 265–277.

Gelchinsky, B. (1989). Homomorphic imaging in processing and interpretaton of seismic data - fundamentals and schemes. In *59th Annual Internat. Mtg., Soc. Expl. Geophys., Expanded Abstracts*, pp. 983. Soc. Expl. Geophys.

Glogovsky, V., E. Landa, and J. Paffenholz (2002). Integrated approach to subsalt depth imaging: Synthetic case study. *The Leading Edge 21*(12), 1217–1226.

Gray, S. H. (2001). Seismic imaging. *Geophysics 66*(1), 15–17.

Gray, S. H., J. Etgen, J. Dellinger, and D. Whitmore (2001). Seismic migration problems and solutions. *Geophysics 66*(5), 1622–1640.

Guo, Z. (2004). *Single streamer wavelet estimation: Extending Extinction Theorem concepts towards a practical solution*. Ph. D. thesis, University of Houston.

Hagedoorn, J. G. (1954). A process of seismic reflection interpretation. *Geophysical Prospecting 2*, 85–127.

Herron, D. (2000). Pitfalls in seismic interpretation: Depth migration artifacts. *The Leading Edge 19*, 1016–1017.

Innanen, K. A. (2003). *Methods for the treatment of acoustic and absorptive/dispersive wave field measurements*. Ph. D. thesis, University of British Columbia.

Innanen, K. A., A. B. Weglein, and T. J. Ulrych (2004). Basic numerics in the non-linear inversion of primaries: simultaneous imaging and inversion II. *M-OSRP Annual Report 3*.

Jacobs, B. (1980). A program for inversion by T-matrix iteration. *Stanford Exploration Project 24*.

Jiang, Z., J. Yu, G. Schuster, and B. E. Hornby (2005). Migration of multiples. *The Leading Edge 24*(3), 315–318.

Jost, R. and W. Kohn (1952). Construction of a potential from a phase shift. *Phys. Rev.* (87), 977–992.

Kennett, B. L. N. (1983). *Seismic Wave Propagation in Stratified Media* (2nd ed.). Cambridge University Press.

Keys, R. G. (2002). Simplification of a leading order imaging series. Personal Communication.

Keys, R. G. (2003). Derivation of a leading order imaging series for variable velocity case. Personal Communication.

Landa, E. (2004). Imaging without a velocity model using path-summation approach. In *74th Annual Internat. Mtg., Soc. Expl. Geophys., Expanded Abstracts*. Soc. Expl. Geophys.

Liu, F., B. G. Nita, A. B. Weglein, and K. A. Innanen (2004). Inverse scattering series in the presence of lateral variations. *M-OSRP Annual Report 3*.

Liu, F. and A. B. Weglein (2003). Initial analysis of the inverse scattering series for a variable background. *M-OSRP Annual Report 2*, 210–225.

Mann, J., P. Hubral, G. Hoecht, R. Jaeger, and T. Mueller (1999). Applications of the common-reflection-surface stack. In *69th Annual Internat. Mtg., Soc. Expl. Geophys., Expanded Abstracts*, pp. 1829–1832. Soc. Expl. Geophys.

Matson, K. H. (1996). The relationship between scattering theory and the primaries and multiples of reflection seismic data. *Journal of Seismic Exploration 5*, 63–78.

Matson, K. H. (1997). *An inverse-scattering series method for attenuating elastic multiples from multicomponent land and ocean bottom seismic data*. Ph. D. thesis, University of British Columbia.

McMechan, G. (1983). Migration by extrapolation of time-dependent boundary values. *Geophysical Prospecting 31*, 413–420.

Mittet, R. (2002). Multiple suppression by prestack reverse time migration – a nail in the coffin. In *64th Annual Internat. Mtg., Eur. Assn. Geosci. Eng., Expanded Abstracts*, Number P025. Eur. Assn. Geosci. Eng.

Morse, P. M. and H. Feshbach (1953). *Methods of theoretical physics*. McGraw-Hill Book Co.

Moses, H. (1956). Calculation of scattering potential from reflection coefficients. *Phys. Rev.* (102), 559–567.

Nita, B. G., K. H. Matson, and A. B. Weglein (2004). Forward scattering series and seismic events: Far field approximations, critical and postcritical events. *SIAM Journal of Applied Mathematics 64*(6), 2167–2185.

Paffenholz, J., J. Stefani, W. H. McLain, and K. Bishop (2002). SIGSBEE_2A synthetic subsalt dataset - image quality as function of migration algorithm and velocity model error. In *64th Mtg.: Eur. Assn. Geosci. Eng.*, pp. B019. Eur. Assn. Geosci. Eng.

Prosser, R. T. (1969). Formal solutions of inverse scattering problems. *Journal of Mathematical Physics 10*(10), 1819–1822.

Prosser, R. T. (1976). Formal solutions of inverse scattering problems II. *Journal of Mathematical Physics 17*(10), 1775–1779.

Prosser, R. T. (1992). Formal solutions of inverse scattering problems V. *Journal of Mathematical Physics 33*(10), 3493–3496.

Ramirez, A. C. and A. B. Weglein (2005). Paper title. *Journal of Seismic Exploration 0*, 00–00.

Robertsson, J. O. A. and E. Kragh (2002). Rough-sea deghosting using a single streamer and a pressure gradient approximation. *Geophysics 67*, 2005–2011.

Scales, J. A. (1997). *Theory of seismic imaging*. Samizdat Press.

Schneider, W. A. (1978). Integral formulation for migration in two-dimensions and three-dimensions. *Geophysics 43*(1), 49–76.

Shaw, S. A., A. B. Weglein, D. J. Foster, K. H. Matson, and R. G. Keys (2003). Isolation of a leading order depth imaging series and analysis of its convergence properties. *M-OSRP Annual Report 2*, 157–195.

Stolt, R. H. (1978). Migration by Fourier transform. *Geophysics 43*(1), 23–48.

Stolt, R. H. (1984). Comment on "A simple exact method of three-dimensional migration - Theory", by Jakubowicz, H., et al. *Geophysical Prospecting 32*, 347–349.

Stolt, R. H. and Benson (1987). *Seismic Migration*. Society of Exploration Geophysicists.

Stolt, R. H. and B. Jacobs (1980). An approach to the inverse seismic problem. *Stanford Exploration Project 25*.

Stolt, R. H. and A. B. Weglein (1985). Migration and inversion of seismic data. *Geophysics 50*(12), 2458–2472.

Tarantola, A. (1987). *Inverse Problem Theory*. Elsevier Science B.V.

Taylor, J. R. (1972). *Scattering theory: the quantum theory on nonrelativistic collisions*. Wiley, New York.

Treitel, S., P. R. Gutowski, and D. E. Wagner (1982). Plane-wave decomposition of seismograms. *Geophysics 47*(10), 1375–1401.

Verschuur, D. J., A. J. Berkhout, and C. P. A. Wapenaar (1992). Adaptive surface-related multiple elimination. *Geophysics 57*, 1166–1177.

Walker, C. and T. J. Ulrych (1983). Autoregressive recovery of the acoustic impedance. *Geophysics 48*(10), 1338–1350.

Wapenaar, C. P. A. (1992). The infinite aperture paradox. *Journal of Seismic Exploration* (1), 325–336.

Wapenaar, C. P. A., G. L. Peels, V. Budejicky, and A. J. Berkhout (1989). Inverse extrapolation of primary seismic waves. *Geophysics 54*(7), 853–863.

Weglein, A. B., F. V. Araújo, P. M. Carvalho, R. H. Stolt, K. H. Matson, R. T. Coates, D. Corrigan, D. J. Foster, S. A. Shaw, and H. Zhang (2003). Inverse scattering series and seismic exploration. *Inverse Problems 19*, R27–R83.

Weglein, A. B., W. E. Boyce, and J. E. Anderson (1981). Obtaining three-dimensional velocity information directly from reflection seismic data: An inverse scattering formalism. *Geophysics 46*(8), 1116–1120.

Weglein, A. B., P. M. Carvalho, and R. H. Stolt (1992). Nonlinear inverse scattering for multiple suppression: Application to real data. part I. In *62nd Ann. Internat. Mtg: Soc. of Expl. Geophys., Expanded Abstracts*, pp. 1093–1095. Soc. Expl. Geophys.

Weglein, A. B., D. J. Foster, K. H. Matson, S. A. Shaw, P. M. Carvalho, and D. Corrigan (2001). An inverse-scattering sub-series for predicting the spatial location of reflectors without the precise reference medium and wave velocity. In *71st Annual Internat. Mtg., Soc. Expl. Geophys., Expanded Abstracts*, pp. 2108–2111. Soc. Expl. Geophys.

Weglein, A. B., D. J. Foster, K. H. Matson, S. A. Shaw, P. M. Carvalho, and D. Corrigan (2002). Predicting the correct spatial location of reflectors without knowing or determining the precise medium and wave velocity: initial concept, algorithm and analytic and numerical example. *Journal of Seismic Exploration 10*(4), 367–382.

Weglein, A. B., F. A. Gasparotto, P. M. Carvalho, and R. H. Stolt (1997). An inverse-scattering series method for attenuating multiples in seismic reflection data. *Geophysics 62*(6), 1975–1989.

Weglein, A. B. and K. H. Matson (1998). Inverse scattering internal multiple attenuation: an analytic example and subevent interpretation. In *Proc. SPIE*. SPIE.

Weglein, A. B., K. H. Matson, D. J. Foster, P. M. Carvalho, D. Corrigan, and S. A. Shaw (2000). imaging and inversion at depth without a velocity model: Theory, concepts and initial evaluation. In *70th Annual Internat. Mtg., Soc. Expl. Geophys., Expanded Abstracts*, pp. 1016–1019. Soc. Expl. Geophys.

Weglein, A. B., S. A. Shaw, K. H. Matson, J. L. Sheiman, R. H. Stolt, T. H. Tan, A. Osen, G. Correa, K. A. Innanen, Z. Guo, and J. Zhang (2002). New approaches to deghosting towed-streamer and ocean-bottom pressure measurements. In *72nd Annual Internat. Mtg., Soc. Expl. Geophys., Expanded Abstracts*, pp. 1016–1019. Soc. Expl. Geophys.

Weglein, A. B., T. H. Tan, K. H. Matson, S. A. Shaw, and D. J. Foster (2000). prediction of the wavefield anywhere above an ordinary towed streamer: Applications to source wavelet estimation, demultiple, and imaging. In *70th Annual Internat. Mtg., Soc. Expl. Geophys., Expanded Abstracts*, pp. 2413–2415. Soc. Expl. Geophys.

Whitmore, N. D. (1983). Iterative depth migration by backward time propagation. In *53rd Annual Internat. Mtg., Soc. Expl. Geophys., Expanded Abstracts*, pp. 382–385. Soc. Expl. Geophys.

Youn, O. K. and H.-W. Zhou (2001). Depth imaging with multiples. *Geophysics 66*, 246–255.

Zhang, H. and A. B. Weglein (2003). Target identification using the inverse scattering series: inversion of large-contrast, variable velocity and density acoustic media. *M-OSRP Annual Report 2*.

Zhang, H. and A. B. Weglein (2004a). Target identification using the inverse scattering series: data requirements for the direct inversion of large-contrast, inhomogeneous elastic media. *M-OSRP Annual Report 3*.

Zhang, J. and A. B. Weglein (2004b). Deghosting of towed streamer and ocean bottom cable data. *M-OSRP Annual Report 3*.

Ziolkowski, A. (1991). Why don't we measure seismic signatures? *Geophysics 56*(2), 190–201.

APPENDIX

A. DERIVATION OF THE FIRST TERM, α_1

We derive the first term in the inverse series for a constant density acoustic medium and a reference medium that consists of a 3-D wholespace with velocity c_0. The perturbation $V = k_0^2\alpha$ where $k_0 = \omega/c_0$ and the solution for α_1 is a linear inversion of the scattered field, D. Beginning with Eq. (3.6), D are related to α_1 by

$$D\left(\vec{x}_g|\vec{x}_s;\omega\right) = \int_{-\infty}^{+\infty} d\vec{x}'\, G_0\left(\vec{x}_g|\vec{x}';\omega\right) k_0^2\alpha_1\left(\vec{x}'\right) G_0\left(\vec{x}'|\vec{x}_s;\omega\right). \tag{A.1}$$

Implicit in Eq. (A.1) is that the incident field is the result of a point source and not a plane wave. The two reference Green functions in Eq. (A.1) satisfy

$$\left(\nabla^2 + \frac{\omega^2}{c_0^2}\right) G_0 = -\delta \tag{A.2}$$

and the causal solutions are

$$G_0(\vec{x}_g|\vec{x}';\omega) = \frac{-1}{(2\pi)^3}\int_{-\infty}^{+\infty} d\vec{k}' \frac{e^{ik_{x'}(x_g-x')}e^{ik_{y'}(y_g-y')}e^{ik_{z'}(z_g-z')}}{\left[k_0 - (|\vec{k}'| - i\epsilon)\right]\left[k_0 + (|\vec{k}'| + i\epsilon)\right]} \tag{A.3}$$

where $|\vec{k}'| = \sqrt[+]{k_{x'}^2 + k_{y'}^2 + k_{z'}^2}$ and

$$G_0(\vec{x}'|\vec{x}_s;\omega) = \frac{-1}{(2\pi)^3}\int_{-\infty}^{+\infty} d\vec{k}_{x_s} \frac{e^{ik_{x_s}(x'-x_s)}e^{ik_{y_s}(y'-y_s)}e^{ik_{z_s}(z'-z_s)}}{\left[k_0 - (|\vec{k}_{x_s}| - i\epsilon)\right]\left[k_0 + (|\vec{k}_{x_s}| + i\epsilon)\right]} \tag{A.4}$$

where $|\vec{k}_{x_s}| = \sqrt[+]{k_{x_s}^2 + k_{y_s}^2 + k_{z_s}^2}$. The parameter $\epsilon > 0$ shifts the poles in the integrand to ensure that the Green functions are causal (see, e.g., DeSanto, 1992, p.45). For reasons that will become clear later (in Eqs. A.13 and A.14), we add the small imaginary part to k_0 by defining $k_{0+} \doteq k_0 + i\epsilon$. In that case, substituting the Green functions into Eq. (A.1) yields

$$\begin{aligned} D\left(\vec{x}_g|\vec{x}_s;\omega\right) =& \frac{1}{(2\pi)^6}\int_{-\infty}^{+\infty} d\vec{x}' \int_{-\infty}^{+\infty} dk_{x'} \int_{-\infty}^{+\infty} dk_{y'} \\ &\times \int_{-\infty}^{+\infty} dk_{z'} \frac{e^{ik_{x'}(x_g-x')}e^{ik_{y'}(y_g-y')}e^{ik_{z'}(z_g-z')}}{k_{0+}^2 - k_{x'}^2 - k_{y'}^2 - k_{z'}^2} k_0^2\alpha_1(\vec{x}') \\ &\times \int_{-\infty}^{+\infty} dk_{x_s} \int_{-\infty}^{+\infty} dk_{y_s} \int_{-\infty}^{+\infty} dk_{z_s} \frac{e^{ik_{x_s}(x'-x_s)}e^{ik_{y_s}(y'-y_s)}e^{ik_{z_s}(z'-z_s)}}{k_{0+}^2 - k_{x_s}^2 - k_{y_s}^2 - k_{z_s}^2}. \end{aligned} \tag{A.5}$$

Performing a double Fourier transform over x_g and y_g

$$\begin{aligned}
D(k_{x_g}, k_{y_g}, z_g|\vec{x}_s;\omega) =& \int_{-\infty}^{+\infty} dx_g \int_{-\infty}^{+\infty} dy_g D\left(x_g, y_g, z_g|\vec{x}_s;\omega\right) e^{-ik_{x_g}x_g} e^{-ik_{y_g}y_g} \\
=& \frac{1}{(2\pi)^6} \underbrace{\int_{-\infty}^{+\infty} dx_g \int_{-\infty}^{+\infty} dy_g}_{} \int_{-\infty}^{+\infty} d\vec{x}' \int_{-\infty}^{+\infty} dk_{x'} \int_{-\infty}^{+\infty} dk_{y'} \\
& \times \underbrace{e^{ix_g(k_{x'}-k_{x_g})} e^{iy_g(k_{y'}-k_{y_g})}}_{} \int_{-\infty}^{+\infty} dk_{z'} \frac{e^{-ik_{x'}x'} e^{-ik_{y'}y'} e^{ik_{z'}(z_g-z')}}{k_{0+}^2 - k_{x'}^2 - k_{y'}^2 - k_{z'}^2} k_0^2 \alpha_1(\vec{x}') \\
& \times \int_{-\infty}^{+\infty} dk_{x_s} \int_{-\infty}^{+\infty} dk_{y_s} \int_{-\infty}^{+\infty} dk_{z_s} \frac{e^{ik_{x_s}(x'-x_s)} e^{ik_{y_s}(y'-y_s)} e^{ik_{z_s}(z'-z_s)}}{k_{0+}^2 - k_{x_s}^2 - k_{y_s}^2 - k_{z_s}^2}.
\end{aligned} \tag{A.6}$$

Carrying out the integrals over x_g and y_g (braced terms) produces two delta functions: $(2\pi)^2\delta(k_{x'} - k_{x_g})\delta(k_{y'} - k_{y_g})$. Then the integrals over $k_{x'}$ and $k_{y'}$ can be performed giving

$$\begin{aligned}
D(k_{x_g}, k_{y_g}, z_g|\vec{x}_s;\omega) =& \frac{1}{(2\pi)^4} \int_{-\infty}^{+\infty} d\vec{x}' \int_{-\infty}^{+\infty} dk_{z'} \frac{e^{-ik_{x_g}x'} e^{-ik_{y_g}y'} e^{ik_{z'}(z_g-z')}}{k_{0+}^2 - k_{x_g}^2 - k_{y_g}^2 - k_{z'}^2} k_0^2 \alpha_1(\vec{x}') \\
& \times \int_{-\infty}^{+\infty} dk_{x_s} \int_{-\infty}^{+\infty} dk_{y_s} \int_{-\infty}^{+\infty} dk_{z_s} \frac{e^{ik_{x_s}(x'-x_s)} e^{ik_{y_s}(y'-y_s)} e^{ik_{z_s}(z'-z_s)}}{k_{0+}^2 - k_{x_s}^2 - k_{y_s}^2 - k_{z_s}^2}.
\end{aligned} \tag{A.7}$$

Now assume that the velocity perturbation, α, is invariant in the x and y directions, which implies that

$$\alpha_1(\vec{x}) \equiv \alpha_1(z). \tag{A.8}$$

Collecting the exponentials in x' and y' and then carrying out the integrations with respect to these variable produces two more delta functions (braced terms below) allowing integration over k_{x_s} and k_{y_s}:

$$\begin{aligned}
D(k_{x_g}, k_{y_g}, z_g|\vec{x}_s;\omega) =& \frac{1}{(2\pi)^4} \underbrace{\int_{-\infty}^{+\infty} dx' \int_{-\infty}^{+\infty} dy'}_{} \int_{-\infty}^{+\infty} dz' \int_{-\infty}^{+\infty} dk_{z'} \\
& \times \frac{e^{ik_{z'}(z_g-z')}}{k_{0+}^2 - k_{x_g}^2 - k_{y_g}^2 - k_{z'}^2} k_0^2 \alpha_1(z') \\
& \times \int_{-\infty}^{+\infty} dk_{x_s} \underbrace{e^{ix'(k_{x_s}-k_{x_g})}}_{} \int_{-\infty}^{+\infty} dk_{y_s} \underbrace{e^{iy'(k_{y_s}-k_{y_g})}}_{} \\
& \times \int_{-\infty}^{+\infty} dk_{z_s} \frac{e^{-ik_{x_s}x_s} e^{-ik_{y_s}y_s} e^{ik_{z_s}(z'-z_s)}}{k_{0+}^2 - k_{x_s}^2 - k_{y_s}^2 - k_{z_s}^2} \\
=& \frac{1}{(2\pi)^2} \int_{-\infty}^{+\infty} dz' \int_{-\infty}^{+\infty} dk_{z'} \frac{e^{ik_{z'}(z_g-z')}}{k_{0+}^2 - k_{x_g}^2 - k_{y_g}^2 - k_{z'}^2} \\
& \times k_0^2 \alpha_1(z') \int_{-\infty}^{+\infty} dk_{z_s} \frac{e^{-ik_{x_g}x_s} e^{-ik_{y_g}y_s} e^{ik_{z_s}(z'-z_s)}}{k_{0+}^2 - k_{x_g}^2 - k_{y_g}^2 - k_{z_s}^2}.
\end{aligned} \tag{A.9}$$

Note that the integrals over x' and y' in Eq. (A.9), for a laterally invariant medium where α_1 is not a function of x' or y', demonstrates that $k_{x_g} = k_{x_s}$ and $k_{y_g} = k_{y_s}$ reducing the number of independent variables from five to three. As result, the vertical wavenumbers defined by

$$q_g^2 \doteq k_{0+}^2 - k_{x_g}^2 - k_{y_g}^2 \tag{A.10}$$

and

$$q_s^2 \doteq k_{0+}^2 - k_{x_s}^2 - k_{y_s}^2 \tag{A.11}$$

are also equal (i.e., $q_g = q_s$). Substituting Eq. (A.10) into Eq. (A.9) gives

$$\begin{aligned} D(k_{x_g}, k_{y_g}, z_g|\vec{x}_s;\omega) =& \frac{1}{(2\pi)^2} e^{-ik_{x_g}x_s} e^{-ik_{y_g}y_s} \int_{-\infty}^{+\infty} dz' k_0^2 \alpha_1(z') \\ & \times \int_{-\infty}^{+\infty} dk_{z'} \frac{e^{ik_{z'}(z_g - z')}}{q_g^2 - k_{z'}^2} \int_{-\infty}^{+\infty} dk_{z_s} \frac{e^{ik_{z_s}(z' - z_s)}}{q_g^2 - k_{z_s}^2}. \end{aligned} \tag{A.12}$$

We are now in a position to perform the integrals with respect to $k_{z'}$ and k_{z_s}. Treating the singularities in these integrals is straightforward because q_g has a small positive imaginary part due to our use of the causal Green functions in Eqs. (A.3) and (A.4). Therefore, we have two 1-D causal Green functions (see, e.g., DeSanto, 1992, p. 57):

$$\int_{-\infty}^{+\infty} dk_{z'} \frac{e^{ik_{z'}(z_g - z')}}{q_g^2 - k_{z'}^2} = -\int_{-\infty}^{+\infty} dk_{z'} \frac{e^{ik_{z'}(z_g - z')}}{(k_{z'} - q_g)(k_{z'} + q_g)} = -\frac{\pi i}{q_g} e^{iq_g|z_g - z'|} \tag{A.13}$$

and similarly

$$\int_{-\infty}^{+\infty} dk_{z_s} \frac{e^{ik_{z_s}(z' - z_s)}}{q_g^2 - k_{z_s}^2} = -\frac{\pi i}{q_g} e^{iq_g|z' - z_s|}. \tag{A.14}$$

After performing these integrals, we let $\epsilon \to 0$ and so $k_{0+} \to k_0$. Substituting Eqs. (A.13) and (A.14) into Eq. (A.12) gives

$$\begin{aligned} D(k_{x_g}, k_{y_g}, z_g|\vec{x}_s;\omega) =& \frac{1}{(2\pi)^2} e^{-ik_{x_g}x_s} e^{-ik_{y_g}y_s} \int_{-\infty}^{+\infty} dz' k_0^2 \alpha_1(z') \left(-\frac{\pi i}{q_g} e^{iq_g|z_g - z'|}\right) \left(-\frac{\pi i}{q_g} e^{iq_g|z' - z_s|}\right) \\ =& \frac{e^{-ik_{x_g}x_s} e^{-ik_{y_g}y_s}}{-4q_g^2} \int_{-\infty}^{+\infty} dz' e^{iq_g(z' - z_g)} k_0^2 \alpha_1(z') e^{iq_g(z' - z_s)} \\ =& \frac{k_0^2}{-4q_g^2} e^{-ik_{x_g}x_s} e^{-ik_{y_g}y_s} e^{-iq_g(z_g + z_s)} \alpha_1(-2q_g) \end{aligned} \tag{A.15}$$

where in Eq. (A.15) we have made use of the fact that the scattering points are below the measurement surface ($z' > z_g$ and $z' > z_s$). Furthermore, we recognized the Fourier transform of α_1 where $2q_g$ is the Fourier conjugate variable to depth, z. We could rearrange Eq. (A.15) and perform and inverse Fourier transform over $2q_g$ to solve for $\alpha_1(z)$. Instead we set about changing from cartesian to cylindrical coordinates.

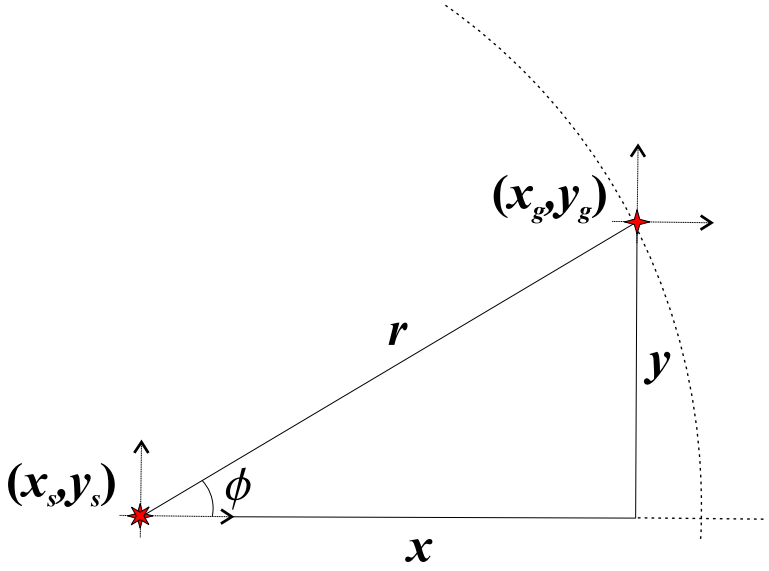

Fig. A.1: Plan view showing the relationship between the horizontal cartesian and cylindrical coordinates. r is the source-receiver offset in the horizontal plane and ϕ is the azimuth. For a 1-D medium, the data are invariant in azimuth.

Performing a double inverse Fourier transform over k_{x_g} and k_{y_g} yields

$$\begin{aligned} D(\vec{x}_g|\vec{x}_s;\omega) =& \frac{1}{(2\pi)^2}\int_{-\infty}^{+\infty} dk_{x_g} e^{ik_{x_g}x_g} \int_{-\infty}^{+\infty} dk_{y_g} e^{ik_{y_g}y_g} D(k_{x_g}, k_{y_g}, z_g|\vec{x}_s;\omega) \\ =& \frac{1}{(2\pi)^2}\int_{-\infty}^{+\infty} dk_{x_g} e^{ik_{x_g}x_g} \int_{-\infty}^{+\infty} dk_{y_g} e^{ik_{y_g}y_g} \frac{k_0^2}{-4q_g^2} e^{-ik_{x_g}x_s} e^{-ik_{y_g}y_s} e^{-iq_g(z_g+z_s)} \alpha_1(-2q_g) \\ =& \frac{1}{(2\pi)^2}\int_{-\infty}^{+\infty} dk_{x_g} \int_{-\infty}^{+\infty} dk_{y_g} \frac{k_0^2}{-4q_g^2} \alpha_1(-2q_g) e^{ik_{x_g}(x_g-x_s)} e^{ik_{y_g}(y_g-y_s)} e^{-iq_g(z_g+z_s)}. \end{aligned} \tag{A.16}$$

Since source and receiver depths z_s and z_g are fixed, both sides of Eq. (A.16) appear to be functions of five variables: x_g, x_s, y_g, y_s and ω (left-hand side) or q_g (right-hand side). However, we found in Eq. (A.9) that the source and receiver horizontal wavenumbers were equal ($k_{x_g} = k_{x_s}$ and $k_{y_g} = k_{y_s}$) reducing the number of independent variables from five to three. Similarly, we may note that D in Eq. (A.16) is a function of the differences $x = (x_g - x_s)$ and $y = (y_g - y_s)$ and that the conjugate variables to these differences are $k_{x_g} = k_x$ and $k_{y_g} = k_y$, respectively. Physical intuition would suggest that the data are really only a function of two independent variables for a 1-D Earth: source-receiver offset, r, and time or temporal frequency, ω. We will change from cartesian to cylindrical coordinates where the *offset* variables satisfy (see Fig. A.1)

$$x = x_g - x_s = r\cos\phi \tag{A.17}$$
$$y = y_g - y_s = r\sin\phi \tag{A.18}$$

and recalling the definition of q_g in Eq. (A.10), we have (for this 1-D case)

$$q_g^2 = k_0^2 - k_x^2 - k_y^2 \tag{A.19}$$
$$= k_0^2 - k_r^2 \tag{A.20}$$

where k_r is defined by

$$k_r^2 \doteq k_x^2 + k_y^2. \tag{A.21}$$

Rewriting Eq. (A.16) in terms of the cartesian offset variables

$$D(x,y;\omega) = \frac{1}{(2\pi)^2}\int_{-\infty}^{+\infty} dk_x \int_{-\infty}^{+\infty} dk_y \frac{k_0^2}{-4q_g^2}\alpha_1(-2q_g)e^{ik_x x}e^{ik_y y}e^{-iq_g(z_g+z_s)}, \tag{A.22}$$

and changing from cartesian to cylindrical coordinates where the conjugate variables satisfy

$$\int_{-\infty}^{+\infty} dk_x \int_{-\infty}^{+\infty} dk_y = \int_0^{\infty} k_r dk_r \int_0^{2\pi} d\tilde{\phi}, \tag{A.23}$$

we substitute Eq. (A.23) into Eq. (A.22) yielding

$$D(r,\phi;\omega) = \frac{1}{(2\pi)^2}\int_0^{\infty} dk_r \int_0^{2\pi} d\tilde{\phi}\frac{k_0^2 k_r}{-4q_g^2}\alpha_1(-2q_g)e^{ik_r\cos\tilde{\phi}r\cos\phi}e^{ik_r\sin\tilde{\phi}r\sin\phi}e^{-iq_g(z_g+z_s)}. \tag{A.24}$$

Then, since,

$$\int_0^{2\pi} e^{ik_r r\left(\cos\tilde{\phi}\cos\phi+\sin\tilde{\phi}\sin\phi\right)}d\tilde{\phi} = \int_0^{2\pi} e^{ik_r r\left[\cos\left(\tilde{\phi}-\phi\right)\right]}d\tilde{\phi} = 2\pi J_0(k_r r), \tag{A.25}$$

where $J_0(k_r r)$ is a zero order Bessel function of the first kind, Eq. (A.24) becomes

$$D(r;\omega) = \frac{1}{(2\pi)}\int_0^{\infty} \frac{k_0^2}{-4q_g^2}\alpha_1(-2q_g)e^{-iq_g(z_g+z_s)}J_0(k_r r)k_r dk_r \tag{A.26}$$

which is an expression, in cylindrical coordinates, for the scattered field in terms of α_1. The data are now clearly seen to be a function of two independent variables. Equation (A.26) can be inverted by recognizing the Fourier-Bessel transform pairs:

$$f(r) = \int_0^{\infty} F(k_r)J_0(k_r r)k_r dk_r \tag{A.27}$$
$$F(k_r) = \int_0^{\infty} f(r)J_0(k_r r)r dr \tag{A.28}$$

which leads to

$$\alpha_1(-2q_g) = 2\pi \frac{-4q_g^2}{k_0^2} e^{iq_g(z_g+z_s)} \int_0^\infty D(r;\omega) J_0(k_r r) r dr \tag{A.29}$$

where

$$q_g = k_0 \sqrt{1 - \frac{k_r^2}{k_0^2}}. \tag{A.30}$$

From Eq. (A.29), we see that α_1 is over-determined (there are more free variables on the right-hand side than on the left). Inverse Fourier transforming both sides of Eq. (A.29) gives

$$\alpha_1(z) = -8 \int_{-\infty}^{+\infty} \frac{q_g^2}{k_0^2} e^{-iq_g(2z-(z_g+z_s))} \int_0^\infty D(r;\omega) J_0(k_r r) r dr dq_g. \tag{A.31}$$

How we perform the q_g integral has implications for handling the over-determinedness. Considering fixed angles of incidence, θ_0, will lead to a number of different estimates of α_1. Fixing θ_0 is the same as fixing horizontal and vertical slownesses, p and ζ, respectively, which are defined by

$$p \doteq \frac{\sin\theta_0}{c_0} \text{ and } \zeta \doteq \frac{\cos\theta_0}{c_0}. \tag{A.32}$$

Note that these slownesses are functions of the reference velocity only, and so do not require knowledge of the actual velocity. They might be more usefully described as *reference* slownesses. With our decision to hold θ_0 fixed, q_g is still allowed to vary through the variation in ω (since $q_g = \omega\zeta$). We proceed by changing variables from q_g to ω:

$$\alpha_1(z,p) = -8\zeta\cos^2\theta_0 \int_{-\infty}^{+\infty} e^{-i\omega\zeta(2z-z_g-z_s)} \int_0^\infty D(r;\omega) J_0(\omega p r) r dr d\omega \tag{A.33}$$

where Eq. (A.32) leads to the relationship

$$\frac{q_g^2}{k_0^2} = \frac{\omega^2\zeta^2}{k_0^2} = c_0^2\zeta^2 = \cos^2\theta_0 \tag{A.34}$$

Defining the two-way vertical travel time, $\tau \doteq \zeta\,(2z - (z_g + z_s))$, and substituting (a) the temporal Fourier transform of the data $D(r,t)$ for $D(r;\omega)$ and (b) the integral form of the Bessel function gives

$$\begin{aligned}
\alpha_1(\tau,p) &= -8\zeta\cos^2\theta_0 \int_{-\infty}^{+\infty} d\omega e^{-i\omega\tau} \int_0^\infty r dr \left(\int_{-\infty}^{+\infty} D(r;t) e^{i\omega t} dt \frac{1}{2\pi} \int_0^{2\pi} e^{i\omega p r\cos\phi} d\phi \right) \\
&= -8\zeta\cos^2\theta_0 \int_{-\infty}^{+\infty} d\omega \int_0^\infty r dr \frac{1}{2\pi} \int_0^{2\pi} d\phi \left(\int_{-\infty}^{+\infty} D(r;t) e^{i\omega(t-(\tau-pr\cos\phi))} dt \right) \\
&= -8\zeta\cos^2\theta_0 \int_0^\infty r dr \frac{1}{2\pi} \int_0^{2\pi} d\phi \left(\int_{-\infty}^{+\infty} D(r;t) 2\pi\delta(t-(\tau-pr\cos\phi)) dt \right) \\
&= -8\zeta\cos^2\theta_0 \int_0^{2\pi} \int_0^\infty D(r;\tau-pr\cos\phi) r dr d\phi.
\end{aligned} \tag{A.35}$$

We may decide to change back to cartesian coordinates, where

$$r = \sqrt{x^2 + y^2}, \quad \phi = \arccos\left(\frac{x}{\sqrt{x^2+y^2}}\right), \quad \phi = \arcsin\left(\frac{y}{\sqrt{x^2+y^2}}\right),$$

$x = (x_g - x_s)$ and $y = (y_g - y_s)$ as illustrated in Fig. 3.1. The partial derivatives are then

$$\begin{aligned}
\frac{\partial r}{\partial x} &= \frac{x}{\sqrt{x^2+y^2}} = \frac{x}{r} \\
\frac{\partial r}{\partial y} &= \frac{y}{\sqrt{x^2+y^2}} = \frac{y}{r} \\
\frac{\partial \phi}{\partial x} &= \frac{-1}{\sqrt{1-\left(\frac{x}{\sqrt{x^2+y^2}}\right)^2}} \times \frac{\left(\sqrt{x^2+y^2} - \frac{x^2}{\sqrt{x^2+y^2}}\right)}{(x^2+y^2)} \\
&= \frac{\left(\frac{x^2}{r} - r\right)}{r^2\sqrt{1-\left(\frac{x^2}{r^2}\right)}} = \frac{\frac{1}{r}\left(x^2 - r^2\right)}{r\sqrt{r^2-x^2}} = \frac{-y}{r^2}
\end{aligned}$$

$$\begin{aligned}
\frac{\partial \phi}{\partial y} &= \frac{1}{\sqrt{1-\left(\frac{y}{\sqrt{x^2+y^2}}\right)^2}} \times \frac{\left(\sqrt{x^2+y^2} - \frac{y^2}{\sqrt{x^2+y^2}}\right)}{(x^2+y^2)} \\
&= \frac{\left(r - \frac{y^2}{r}\right)}{r^2\sqrt{1-\left(\frac{y^2}{r^2}\right)}} = \frac{\frac{1}{r}\left(r^2 - y^2\right)}{r\sqrt{r^2-y^2}} = \frac{x}{r^2}.
\end{aligned}$$

So the Jacobian is

$$\frac{\partial r}{\partial x}\frac{\partial \phi}{\partial y} - \frac{\partial r}{\partial y}\frac{\partial \phi}{\partial x} = \frac{x^2}{r^3} + \frac{y^2}{r^3} = \frac{1}{r}$$

and therefore Eq. (A.35) can be rewritten

$$\alpha_1(\tau, p) = -8\zeta \cos^2\theta_0 \int_{-\infty}^{+\infty}\int_{-\infty}^{+\infty} D(x, y; \tau - px)dxdy. \tag{A.36}$$

Equation (A.36) is recognizable as a scaled slant stack of the recorded data (see, e.g., Treitel et al., 1982).

B. SEPARATION OF α_2 INTO TASK-SPECIFIC TERMS

The integral equation for the second term in the inverse series for the 1-D single parameter acoustic problem is

$$\begin{aligned}\int_{-\infty}^{+\infty} G_0\left(\vec{x}_g|\vec{x}';\omega\right) k_0^2\alpha_2(z')G_0\left(\vec{x}'|\vec{x}_s;\omega\right) d\vec{x}' \\ = -\int_{-\infty}^{+\infty} d\vec{x}'\, G_0\left(\vec{x}_g|\vec{x}';\omega\right) k_0^2\alpha_1(z') \\ \times \int_{-\infty}^{+\infty} d\vec{x}''\, G_0\left(\vec{x}'|\vec{x}'';\omega\right) k_0^2\alpha_1(z'')G_0\left(\vec{x}''|\vec{x}_s;\omega\right). \qquad \text{(B.1)}\end{aligned}$$

Upon substitution of the causal Green functions, the left-hand side becomes

$$\begin{aligned}LHS =& \frac{1}{(2\pi)^6}\int_{-\infty}^{+\infty} d\vec{x}' \int_{-\infty}^{+\infty} dk_{x'} \int_{-\infty}^{+\infty} dk_{y'} \int_{-\infty}^{+\infty} dk_{z'} \frac{e^{ik_{x'}(x_g-x')}e^{ik_{y'}(y_g-y')}e^{ik_{z'}(z_g-z')}}{k_{0+}^2-k_{x'}^2-k_{y'}^2-k_{z'}^2} \\ & \times k_0^2\alpha_2(z')\int_{-\infty}^{+\infty} dk_{x_s} \int_{-\infty}^{+\infty} dk_{y_s} \int_{-\infty}^{+\infty} dk_{z_s} \frac{e^{ik_{x_s}(x'-x_s)}e^{ik_{y_s}(y'-y_s)}e^{ik_{z_s}(z'-z_s)}}{k_{0+}^2-k_{x_s}^2-k_{y_s}^2-k_{z_s}^2} \qquad \text{(B.2)}\end{aligned}$$

and the right-hand side is

$$\begin{aligned}RHS =& \frac{1}{(2\pi)^9}\int_{-\infty}^{+\infty} d\vec{x}' \int_{-\infty}^{+\infty} dk_{x'} \int_{-\infty}^{+\infty} dk_{y'} \int_{-\infty}^{+\infty} dk_{z'} \frac{e^{ik_{x'}(x_g-x')}e^{ik_{y'}(y_g-y')}e^{ik_{z'}(z_g-z')}}{k_{0+}^2-k_{x'}^2-k_{y'}^2-k_{z'}^2} \\ & \times k_0^2\alpha_1(z')\int_{-\infty}^{+\infty} d\vec{x}'' \int_{-\infty}^{+\infty} dk_{x''} \int_{-\infty}^{+\infty} dk_{y''} \int_{-\infty}^{+\infty} dk_{z''} \frac{e^{ik_{x''}(x'-x'')}e^{ik_{y''}(y'-y'')}e^{ik_{z''}(z'-z'')}}{k_{0+}^2-k_{x''}^2-k_{y''}^2-k_{z''}^2} \\ & \times k_0^2\alpha_1(z'')\int_{-\infty}^{+\infty} dk_{x_s} \int_{-\infty}^{+\infty} dk_{y_s} \int_{-\infty}^{+\infty} dk_{z_s} \frac{e^{ik_{x_s}(x''-x_s)}e^{ik_{y_s}(y''-y_s)}e^{ik_{z_s}(z''-z_s)}}{k_{0+}^2-k_{x_s}^2-k_{y_s}^2-k_{z_s}^2} \qquad \text{(B.3)}\end{aligned}$$

where $k_{0+} \doteq k_0 + i\epsilon$ and ϵ is a small positive parameter (see Appendix A). Diagrammatically, forgiving some k_0 factors, we may interpret this equation as shown in Figure B.1 where the scattering points are confined to be deeper than the source and receiver depths.

As with deriving the equation for α_1, the invariability of the perturbation in the horizontal coordinates simplifies the equations significantly. We Fourier transform both sides over x_g

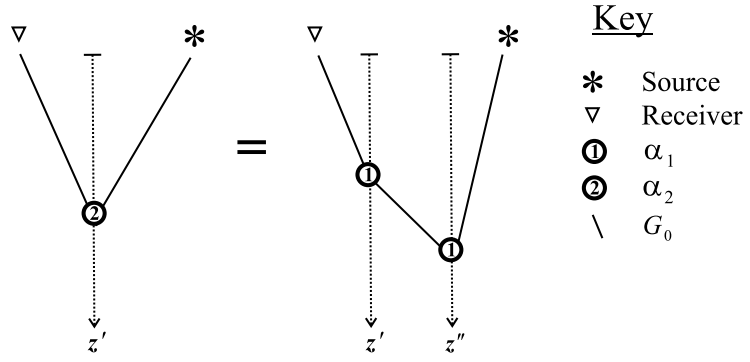

Fig. B.1: *Inverse scattering diagrams representing Eq.(B.1).*

and y_g and perform the integrals over $k_{x'}$ and $k_{y'}$. Therefore,

$$LHS \rightarrow \frac{1}{(2\pi)^4}\int_{-\infty}^{+\infty} d\vec{x}' \int_{-\infty}^{+\infty} dk_{z'} \frac{e^{-ik_{x_g}x'}e^{-ik_{y_g}y'}e^{ik_{z'}(z_g-z')}}{k_{0+}^2-k_{x_g}^2-k_{y_g}^2-k_{z'}^2}$$
$$\times k_0^2\alpha_2(z')\int_{-\infty}^{+\infty} dk_{x_s}\int_{-\infty}^{+\infty} dk_{y_s}\int_{-\infty}^{+\infty} dk_{z_s}\frac{e^{ik_{x_s}(x'-x_s)}e^{ik_{y_s}(y'-y_s)}e^{ik_{z_s}(z'-z_s)}}{k_{0+}^2-k_{x_s}^2-k_{y_s}^2-k_{z_s}^2} \tag{B.4}$$

$$RHS \rightarrow \frac{1}{(2\pi)^7}\int_{-\infty}^{+\infty} d\vec{x}' \int_{-\infty}^{+\infty} dk_{z'} \frac{e^{-ik_{x_g}x'}e^{-ik_{y_g}y'}e^{ik_{z'}(z_g-z')}}{k_{0+}^2-k_{x_g}^2-k_{y_g}^2-k_{z'}^2} k_0^2\alpha_1(z')\int_{-\infty}^{+\infty} d\vec{x}''$$
$$\times \int_{-\infty}^{+\infty} dk_{x''}\int_{-\infty}^{+\infty} dk_{y''}\int_{-\infty}^{+\infty} dk_{z''}\frac{e^{ik_{x''}(x'-x'')}e^{ik_{y''}(y'-y'')}e^{ik_{z''}(z'-z'')}}{k_{0+}^2-k_{x''}^2-k_{y''}^2-k_{z''}^2}k_0^2\alpha_1(z'')$$
$$\times \int_{-\infty}^{+\infty} dk_{x_s}\int_{-\infty}^{+\infty} dk_{y_s}\int_{-\infty}^{+\infty} dk_{z_s}\frac{e^{ik_{x_s}(x''-x_s)}e^{ik_{y_s}(y''-y_s)}e^{ik_{z_s}(z''-z_s)}}{k_{0+}^2-k_{x_s}^2-k_{y_s}^2-k_{z_s}^2}. \tag{B.5}$$

Collecting the exponentials in the horizontal coordinates of the scattering points x', y', x'' and y'', and performing the integrals with respect to these variables produces delta functions

allowing for the k_{x_s} and k_{y_s} integrals, respectively, to be carried out:

$$\begin{aligned}
LHS \rightarrow & \frac{1}{(2\pi)^4} \underbrace{\int_{-\infty}^{+\infty} dx'}\underbrace{\int_{-\infty}^{+\infty} dy'} \int_{-\infty}^{+\infty} dz' \int_{-\infty}^{+\infty} dk_{z'} \frac{e^{ik_{z'}(z_g - z')}}{k_{0+}^2 - k_{x_g}^2 - k_{y_g}^2 - k_{z'}^2} \\
& \times k_0^2 \alpha_2(z') \int_{-\infty}^{+\infty} dk_{x_s} \int_{-\infty}^{+\infty} dk_{y_s} \int_{-\infty}^{+\infty} dk_{z_s} \underbrace{e^{i(k_{x_s} - k_{x_g})x'}} \underbrace{e^{i(k_{y_s} - k_{y_g})y'}} \\
& \times \frac{e^{-ik_{x_s}x_s} e^{-ik_{y_s}y_s} e^{ik_{z_s}(z' - z_s)}}{k_{0+}^2 - k_{x_s}^2 - k_{y_s}^2 - k_{z_s}^2} \\
\rightarrow & \frac{1}{(2\pi)^2} \int_{-\infty}^{+\infty} dz' \int_{-\infty}^{+\infty} dk_{z'} \frac{e^{ik_{z'}(z_g - z')}}{k_{0+}^2 - k_{x_g}^2 - k_{y_g}^2 - k_{z'}^2} k_0^2 \alpha_2(z') \\
& \times \int_{-\infty}^{+\infty} dk_{z_s} \frac{e^{-ik_{x_g}x_s} e^{-ik_{y_g}y_s} e^{ik_{z_s}(z' - z_s)}}{k_{0+}^2 - k_{x_g}^2 - k_{y_g}^2 - k_{z_s}^2}
\end{aligned} \tag{B.6}$$

$$\begin{aligned}
RHS \rightarrow & \frac{1}{(2\pi)^7} \underbrace{\int_{-\infty}^{+\infty} dx'}\underbrace{\int_{-\infty}^{+\infty} dy'} \int_{-\infty}^{+\infty} dz' \int_{-\infty}^{+\infty} dk_{z'} \frac{e^{ik_{z'}(z_g - z')}}{k_{0+}^2 - k_{x_g}^2 - k_{y_g}^2 - k_{z'}^2} \\
& \times k_0^2 \alpha_1(z') \underbrace{\int_{-\infty}^{+\infty} dx''}\underbrace{\int_{-\infty}^{+\infty} dy''} \int_{-\infty}^{+\infty} dz'' \int_{-\infty}^{+\infty} dk_{x''} \int_{-\infty}^{+\infty} dk_{y''} \int_{-\infty}^{+\infty} dk_{z''} \\
& \times \underbrace{e^{i(k_{x''} - k_{x_g})x'}} \underbrace{e^{i(k_{y''} - k_{y_g})y'}} \frac{e^{ik_{z''}(z' - z'')}}{k_{0+}^2 - k_{x''}^2 - k_{y''}^2 - k_{z''}^2} k_0^2 \alpha_1(z'') \int_{-\infty}^{+\infty} dk_{x_s} \int_{-\infty}^{+\infty} dk_{y_s} \\
& \times \int_{-\infty}^{+\infty} dk_{z_s} \underbrace{e^{i(k_{x_s} - k_{x''})x''}} \underbrace{e^{i(k_{y_s} - k_{y''})y''}} \frac{e^{-ik_{x_s}x_s} e^{-ik_{y_s}y_s} e^{ik_{z_s}(z'' - z_s)}}{k_{0+}^2 - k_{x_s}^2 - k_{y_s}^2 - k_{z_s}^2}
\end{aligned} \tag{B.7}$$

$$\begin{aligned}
\rightarrow & \frac{1}{(2\pi)^3} \int_{-\infty}^{+\infty} dz' \int_{-\infty}^{+\infty} dk_{z'} \frac{e^{ik_{z'}(z_g - z')}}{k_{0+}^2 - k_{x_g}^2 - k_{y_g}^2 - k_{z'}^2} k_0^2 \alpha_1(z') \\
& \times \int_{-\infty}^{+\infty} dz'' \int_{-\infty}^{+\infty} dk_{z''} \frac{e^{ik_{z''}(z' - z'')}}{k_{0+}^2 - k_{x_g}^2 - k_{y_g}^2 - k_{z''}^2} k_0^2 \alpha_1(z'') \\
& \times \int_{-\infty}^{+\infty} dk_{z_s} \frac{e^{-ik_{x_g}x_s} e^{-ik_{y_g}y_s} e^{ik_{z_s}(z'' - z_s)}}{k_{0+}^2 - k_{x_g}^2 - k_{y_g}^2 - k_{z_s}^2}.
\end{aligned} \tag{B.8}$$

Having performed all the integrals in the horizontal coordinates, we can evaluate the 1-D

vertical wavenumber integrals:

$$\begin{aligned}
LHS \rightarrow & \frac{k_0^2}{(2\pi)^2} e^{-ik_{x_g}x_s} e^{-ik_{y_g}y_s} \int_{-\infty}^{+\infty} dz' \alpha_2(z') \left(- \int_{-\infty}^{+\infty} dk_{z'} \frac{e^{ik_{z'}(z_g - z')}}{(k_{z'} - q_g)(k_{z'} + q_g)} \right) \\
& \times \left(- \int_{-\infty}^{+\infty} dk_{z_s} \frac{e^{ik_{z_s}(z' - z_s)}}{(k_{z_s} - q_g)(k_{z_s} + q_g)} \right) \\
\rightarrow & \frac{k_0^2}{(2\pi)^2} e^{-ik_{x_g}x_s} e^{-ik_{y_g}y_s} \int_{-\infty}^{+\infty} dz' \alpha_2(z') \left(-\frac{\pi i}{q_g} e^{iq_g|z_g - z'|} \right) \left(-\frac{\pi i}{q_g} e^{iq_g|z' - z_s|} \right) \\
\rightarrow & \frac{-k_0^2}{4q_g^2} e^{-ik_{x_g}x_s} e^{-ik_{y_g}y_s} e^{-iq_g(z_g + z_s)} \int_{-\infty}^{+\infty} dz' \alpha_2(z') e^{2iq_g z'}
\end{aligned} \tag{B.9}$$

where $q_g^2 \doteq k_{0+}^2 - k_{x_g}^2 - k_{y_g}^2$ and we have explicitly set $z' > \{z_g, z_s\}$. Meanwhile, the right-hand side can be simplified:

$$\begin{aligned}
RHS \rightarrow & \frac{1}{(2\pi)^3} \int_{-\infty}^{+\infty} dz' \left(-\frac{\pi i}{q_g} e^{iq_g(z' - z_g)} \right) k_0^2 \alpha_1(z') \\
& \times \int_{-\infty}^{+\infty} dz'' \left(-\frac{\pi i}{q_g} e^{iq_g|z' - z''|} \right) k_0^2 \alpha_1(z'') e^{-ik_{x_g}x_s} e^{-ik_{y_g}y_s} \left(-\frac{\pi i}{q_s} e^{iq_s(z'' - z_s)} \right) \\
\rightarrow & \frac{ik_0^4}{8q_g^3} e^{-ik_{x_g}x_s} e^{-ik_{y_g}y_s} e^{-iq_g(z_g + z_s)} \int_{-\infty}^{+\infty} dz' e^{iq_g z'} \alpha_1(z') \int_{-\infty}^{+\infty} dz'' e^{iq_g|z' - z''|} \alpha_1(z'') e^{iq_g z''}
\end{aligned} \tag{B.10}$$

where, for a 1-D medium, $q_s^2 = q_g^2$ and we have confined $\{z', z''\} > \{z_g, z_s\}$. Having served its purpose, we now let $\epsilon \rightarrow 0$ and so $k_{0+} \rightarrow k_0$. Expanding the absolute value in the exponential and simplifying:

$$\begin{aligned}
RHS \rightarrow & \frac{ik_0^4}{8q_g^3} e^{-ik_{x_g}x_s} e^{-ik_{y_g}y_s} e^{-iq_g(z_g + z_s)} \int_{-\infty}^{+\infty} dz' e^{iq_g z'} \alpha_1(z') \\
& \times \left(\int_{-\infty}^{+\infty} dz'' H(z' - z'') e^{iq_g(z' - z'')} \alpha_1(z'') + \int_{-\infty}^{+\infty} dz'' H(z'' - z') e^{iq_g(z'' - z')} \alpha_1(z'') \right) e^{iq_g z''} \\
\rightarrow & \frac{ik_0^4}{8q_g^3} e^{-ik_{x_g}x_s} e^{-ik_{y_g}y_s} e^{-iq_g(z_g + z_s)} \int_{-\infty}^{+\infty} dz' \alpha_1(z') \\
& \times \left(2 \int_{-\infty}^{+\infty} dz'' H(z' - z'') e^{iq_g(z' - z'')} \alpha_1(z'') \right) e^{iq_g(z' + z'')} \\
\rightarrow & \frac{ik_0^4}{4q_g^3} e^{-ik_{x_g}x_s} e^{-ik_{y_g}y_s} e^{-iq_g(z_g + z_s)} \int_{-\infty}^{+\infty} dz' \alpha_1(z') e^{2iq_g z'} \int_{-\infty}^{+\infty} dz'' H(z' - z'') \alpha_1(z'').
\end{aligned} \tag{B.11}$$

Figure B.2 illustrates the simplification in Eq. (B.11) that arises due to the vertical axis of symmetry. Now equating the two sides, Eqs. (B.9) and (B.11), the phases $\exp(-ik_{x_g}x_s)$,

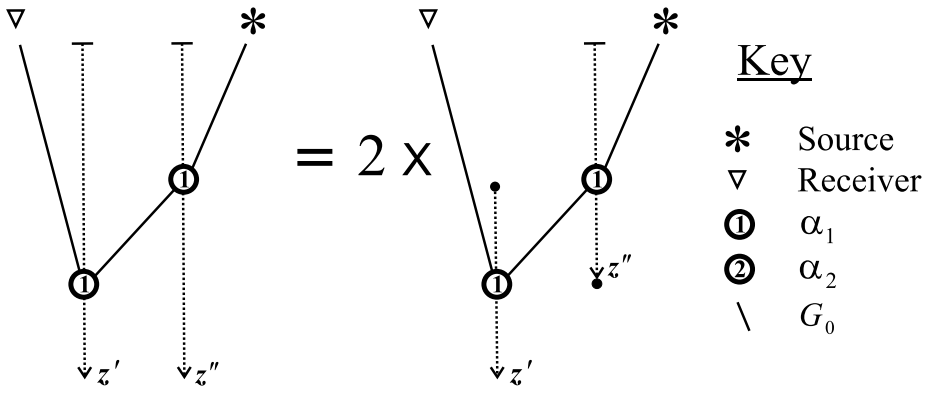

Fig. B.2: *Inverse scattering diagrams representing the simplification in Eq. (B.11) that arises due to the vertical axis of symmetry. The "•" symbol signifies the end-point contributions* $z' = z''$.

$\exp(-ik_{y_g} y_s)$ and $\exp\left(-iq_g\left(z_g + z_s\right)\right)$ cancel leaving

$$\int_{-\infty}^{+\infty} dz' \alpha_2(z') e^{2iq_g z'} = \frac{-ik_0^2}{q_g} \int_{-\infty}^{+\infty} dz' \alpha_1(z') e^{2iq_g z'} \int_{-\infty}^{+\infty} dz'' H(z' - z'') \alpha_1(z''). \tag{B.12}$$

This step is equivalent to source and receiver downward continuation with the constant reference velocity. We can break apart the right hand-side into self-interaction ($z' = z''$) and separated ($z' \neq z''$) daigrams. To effect this separation, we integrate by parts:

$$\int_{-\infty}^{\infty} u dv = uv\Big|_{-\infty}^{\infty} - \int_{-\infty}^{\infty} v du$$

where

$$\begin{aligned}
u =& \int_{-\infty}^{+\infty} dz'' \alpha_1(z'') H(z' - z'') \alpha_1(z') \\
dv =& \frac{-ik_0^2}{q_g} e^{2iq_g z'} dz' \\
\frac{du}{dz'} =& \alpha_1^2(z') + \int_{-\infty}^{+\infty} dz'' \alpha_1(z'') H(z' - z'') \frac{d\alpha_1(z')}{dz'} \\
=& \alpha_1^2(z') + \int_{-\infty}^{z'} dz'' \alpha_1(z'') \frac{d\alpha_1(z')}{dz'} \\
v =& \frac{-k_0^2}{2q_g^2} e^{2iq_g z'}
\end{aligned}$$

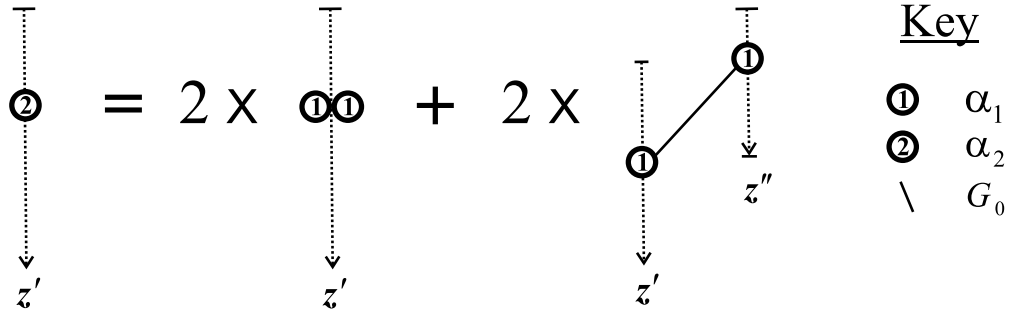

Fig. B.3: *The break-up of the second term in the inverse series into "self-interaction" and "separated" diagram terms (Eq. B.14).*

and so

$$\int_{-\infty}^{+\infty} dz' e^{2iq_g z'} \alpha_2(z') = \left[\frac{-k_0^2}{2q_g^2} e^{2iq_g z'} \int_{-\infty}^{z'} dz'' \alpha_1(z'') \alpha_1(z') \right]_{z'=-\infty}^{\infty} + \int_{-\infty}^{+\infty} dz' e^{2iq_g z'} \frac{k_0^2}{2q_g^2} \left(\alpha_1^2(z') + \int_{-\infty}^{z'} dz'' \alpha_1(z'') \frac{d\alpha_1(z')}{dz'} \right). \quad \text{(B.13)}$$

The boundary terms are zero (assuming α_1, like α, is confined to a finite region) and so

$$\alpha_2(-2q_g) = \int_{-\infty}^{+\infty} dz' e^{2iq_g z'} \frac{k_0^2}{2q_g^2} \left(\alpha_1^2(z') + \int_{0}^{z'} dz'' \alpha_1(z'') \frac{d\alpha_1(z')}{dz'} \right). \quad \text{(B.14)}$$

Figure B.3 illustrates the break-up that takes place when we integrate by parts. We have divided α_2 into self-interaction and separated diagram terms[1].

As in Eq. (A.31), the left-hand-side is a function of one variable (q_g), whereas the right-hand-side is a function of two (q_g and $\omega = k_0 c_0$). For consistency, we choose to keep p constant recognizing that we are estimating $\alpha = \alpha_1 + \alpha_2 + \ldots$ for fixed p values. Therefore, the inverse Fourier transform yields

$$\alpha_2(z,p) = \frac{1}{2\cos^2\theta_0} \left(\alpha_1^2(z,p) + \int_0^z \alpha_1(z',p) dz' \frac{\partial \alpha_1(z,p)}{\partial z} \right) \quad \text{(B.15)}$$

where θ_0 and p are related by Eq. (A.32).

[1] This particularly useful separation step was taken by Foster (2000).

C. A FORMULA FOR THE VELOCITY PERTURBATION IN TERMS OF THE REFLECTION COEFFICIENT AT A SINGLE INTERFACE

We algebraically derive an expression for the velocity perturbation, α, in terms of the angle-dependent reflection coefficient at a single interface. The reference velocity and the velocity in the upper half-space is c_0 and the velocity in the lower half-space is c_1. The interface is at depth $z = z_a$, and so the velocity model is

$$\begin{aligned} c(z) &= c_0 + (c_1 - c_0)H\left(z - z_a\right) \\ &= c_0\left[1 + (\gamma - 1)H\left(z - z_a\right)\right] \end{aligned} \tag{C.1}$$

where we have introduced the parameter $\gamma = c_1/c_0$. From the definition of α (Eq. 3.4), we have

$$\begin{aligned} \alpha(z) = \frac{c_0^2}{c^2(z)} - 1 &= \frac{1}{\left[1 + (\gamma - 1)H\left(z - z_a\right)\right]^2} - 1 \\ &= \left[\frac{1}{1 + (\gamma^2 - 1)} - 1\right] H\left(z - z_a\right) \\ &= \left(\frac{1}{\gamma^2} - 1\right) H\left(z - z_a\right). \end{aligned} \tag{C.2}$$

Meanwhile, we can write the reflection coefficient as a function of the change in velocity at the interface, the incident angle, θ_0, and the transmitted angle, θ_1 :

$$R_{01}(p) = \frac{\zeta_0 - \zeta_1}{\zeta_0 + \zeta_1} = \frac{c_1\cos\theta_0 - c_0\cos\theta_1}{c_1\cos\theta_0 + c_0\cos\theta_1} = \frac{\gamma\cos\theta_0 - \cos\theta_1}{\gamma\cos\theta_0 + \cos\theta_1}. \tag{C.3}$$

Using Snell's Law

$$\sin\theta_1 = \gamma\sin\theta_0 \tag{C.4}$$

we can substitute

$$\cos\theta_1 = \sqrt{1 - \sin^2\theta_1} = \sqrt{1 - \gamma^2\sin^2\theta_0} \tag{C.5}$$

into Eq. (C.3) to eliminate θ_1 :

$$R_{01}(p) = \frac{\gamma\cos\theta_0 - \sqrt{1 - \gamma^2\sin^2\theta_0}}{\gamma\cos\theta_0 + \sqrt{1 - \gamma^2\sin^2\theta_0}} = \frac{\cos\theta_0 - \sqrt{1/\gamma^2 - \sin^2\theta_0}}{\cos\theta_0 + \sqrt{1/\gamma^2 - \sin^2\theta_0}}. \tag{C.6}$$

Rearranging this equation gives

$$\begin{aligned}
1/\gamma^2(p) &= \sin^2\theta_0 + \cos^2\theta_0 \left(\frac{1-R_{01}(p)}{1+R_{01}(p)}\right)^2 \\
&= 1 - \cos^2\theta_0 \left(1 - \left(\frac{1-R_{01}(p)}{1+R_{01}(p)}\right)^2\right) \\
&= 1 - \cos^2\theta_0 \left(1 - \left[1 - 4R_{01}(p) + 8R_{01}^2(p) - 12R_{01}^3(p) + \ldots\right]\right) \\
&= 1 - \cos^2\theta_0 \left[4R_{01}(p) - 8R_{01}^2(p) + 12R_{01}^3(p) - \ldots\right]. \qquad \text{(C.7)}
\end{aligned}$$

Finally, we can substitute Eq. (C.7) into Eq. (C.2) to derive an angle-dependent formula for α :

$$\alpha(z,p) = \left[-4R_{01}(p) + 8R_{01}^2(p) - 12R_{01}^3(p) + \ldots\right] \cos^2\theta_0 H\left(z - z_a\right). \qquad \text{(C.8)}$$

The first term (that is first order in the measured data, i.e., $\mathrm{O}(R_{01})$, is

$$\alpha_1(z,p) = -4R_{01}(p)\cos^2\theta_0 H\left(z - z_a\right). \qquad \text{(C.9)}$$

This is quantitatively equal to the inverse Born approximation (see, e.g., Bleistein et al., 2000, p.105, for the zero-offset result). The consequence of making the Born approximation is to ignore the sum of all the higher order terms. We observe that, for this single interface example,

$$\begin{aligned}
\alpha_2(z,p) &= 8R_{01}^2(p)\cos^2\theta_0 H\left(z - z_a\right) && \text{(C.10)} \\
\alpha_3(z,p) &= -12R_{01}^3(p)\cos^2\theta_0 H\left(z - z_a\right) && \text{(C.11)} \\
\alpha_4(z,p) &= 16R_{01}^4(p)\cos^2\theta_0 H\left(z - z_a\right) && \text{(C.12)} \\
&\vdots
\end{aligned}$$

For contrasts where higher powers in R_{01} are not negligible, we must take more terms in the series (Zhang and Weglein, 2003).

D. SEPARATION OF α_3 INTO TASK-SPECIFIC TERMS

The integral equation for the third term in the inverse series for the single parameter acoustic problem is

$$\begin{aligned}
&\int_{-\infty}^{+\infty} d\vec{x}\,' G_0\left(\vec{x}_{\,g}|\vec{x}\,';\omega\right) k_0^2 \alpha_3(z') G_0\left(\vec{x}\,'|\vec{x}_{\,s};\omega\right) \\
&\qquad = -\int_{-\infty}^{+\infty} d\vec{x}\,' G_0\left(\vec{x}_{\,g}|\vec{x}\,';\omega\right) k_0^2 \alpha_2(z') \\
&\qquad\quad \times \int_{-\infty}^{+\infty} d\vec{x}\,'' G_0\left(\vec{x}\,'|\vec{x}\,'';\omega\right) k_0^2 \alpha_1(z'') G_0\left(\vec{x}\,''|\vec{x}_{\,s};\omega\right) \\
&\qquad - \int_{-\infty}^{+\infty} d\vec{x}\,' G_0\left(\vec{x}_{\,g}|\vec{x}\,';\omega\right) k_0^2 \alpha_1(z') \\
&\qquad\quad \times \int_{-\infty}^{+\infty} d\vec{x}\,'' G_0\left(\vec{x}\,'|\vec{x}\,'';\omega\right) k_0^2 \alpha_2(z'') G_0\left(\vec{x}\,''|\vec{x}_{\,s};\omega\right) \\
&\qquad - \int_{-\infty}^{+\infty} d\vec{x}\,' G_0\left(\vec{x}_{\,g}|\vec{x}\,';\omega\right) k_0^2 \alpha_1(z') \\
&\qquad\quad \times \int_{-\infty}^{+\infty} d\vec{x}\,'' G_0\left(\vec{x}\,'|\vec{x}\,'';\omega\right) k_0^2 \alpha_1(z'') \\
&\qquad\quad \times \int_{-\infty}^{+\infty} d\vec{x}\,''' G_0\left(\vec{x}\,''|\vec{x}\,''';\omega\right) k_0^2 \alpha_1(z''') G_0\left(\vec{x}\,'''|\vec{x}_{\,s};\omega\right). \qquad \text{(D.1)}
\end{aligned}$$

Figure D.1 represents Eq. (D.1) using scattering diagrams (once again forgiving some k_0 factors). Fourier transforming both sides of Eq. (D.1) over x_g and y_g and following the same steps as in deriving Eq. (B.9), the left-hand side becomes

$$LHS \rightarrow \frac{-k_0^2}{4q_g^2} e^{-ik_{x_g}x_s} e^{-ik_{y_g}y_s} e^{-iq_g(z_g+z_s)} \int_{-\infty}^{+\infty} \alpha_3(z') e^{2iq_g z'} dz'. \qquad \text{(D.2)}$$

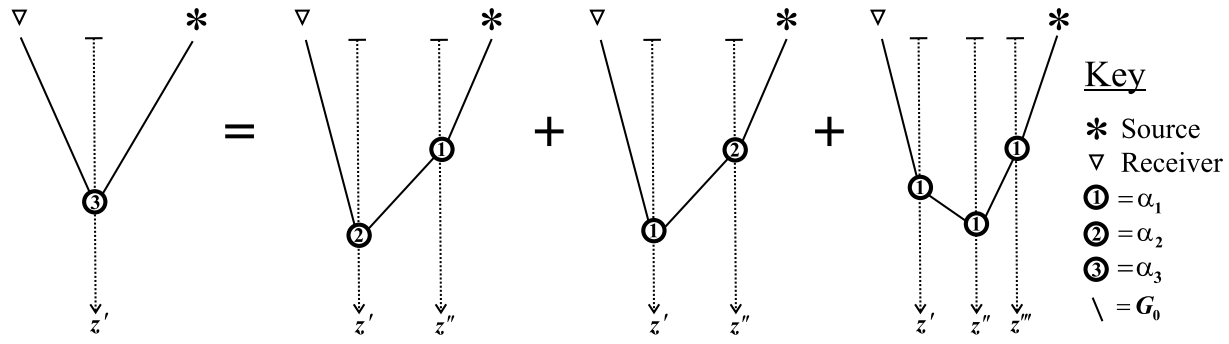

Fig. D.1: *Inverse scattering diagrams representing Eq. (D.1).*

Meanwhile, doing the same thing to the right-hand side, we get

$$
\begin{aligned}
RHS \rightarrow & \frac{k_0^4}{(2\pi)^3} e^{-ik_{x_g}x_s} e^{-ik_{y_g}y_s} \int_{-\infty}^{+\infty} dz' \int_{-\infty}^{+\infty} dk_{z'} \frac{e^{ik_{z'}(z_g - z')}}{q_g^2 - k_{z'}^2} \alpha_2(z') \\
& \times \int_{-\infty}^{+\infty} dz'' \int_{-\infty}^{+\infty} dk_{z''} \frac{e^{ik_{z''}(z' - z'')}}{q_g^2 - k_{z''}^2} \alpha_1(z'') \int_{-\infty}^{+\infty} dk_{z'} \frac{e^{ik_{z_s}(z'' - z_s)}}{q_g^2 - k_{z_s}^2} \\
& + \frac{k_0^4}{(2\pi)^3} e^{-ik_{x_g}x_s} e^{-ik_{y_g}y_s} \int_{-\infty}^{+\infty} dz' \int_{-\infty}^{+\infty} dk_{z'} \frac{e^{ik_{z'}(z_g - z')}}{q_g^2 - k_{z'}^2} \alpha_1(z') \\
& \times \int_{-\infty}^{+\infty} dz'' \int_{-\infty}^{+\infty} dk_{z''} \frac{e^{ik_{z''}(z' - z'')}}{q_g^2 - k_{z''}^2} \alpha_2(z'') \int_{-\infty}^{+\infty} dk_{z'} \frac{e^{ik_{z_s}(z'' - z_s)}}{q_g^2 - k_{z_s}^2} \\
& - \frac{k_0^6}{(2\pi)^4} e^{-ik_{x_g}x_s} e^{-ik_{y_g}y_s} \int_{-\infty}^{+\infty} dz' \int_{-\infty}^{+\infty} dk_{z'} \frac{e^{ik_{z'}(z_g - z')}}{q_g^2 - k_{z'}^2} \alpha_1(z') \\
& \times \int_{-\infty}^{+\infty} dz'' \int_{-\infty}^{+\infty} dk_{z''} \frac{e^{ik_{z''}(z' - z'')}}{q_g^2 - k_{z''}^2} \alpha_1(z'') \\
& \times \int_{-\infty}^{+\infty} dz''' \int_{-\infty}^{+\infty} dk_{z'''} \frac{e^{ik_{z'''}(z'' - z''')}}{q_g^2 - k_{z'''}^2} \alpha_1(z''') \int_{-\infty}^{+\infty} dk_{z_s} \frac{e^{ik_{z_s}(z''' - z_s)}}{q_g^2 - k_{z_s}^2}.
\end{aligned}
\tag{D.3}
$$

The various "k_z" integrals are handled according to the poles shifted in exactly the same way as in the calculations of α_1 and α_2 (see Appendices A and B). This is not a choice but a consequence of the causal Green functions in the Lippmann-Schwinger equation (Eq. 2.7).

Performing the contour integrals yields

$$\begin{aligned}
RHS \rightarrow & \frac{2ik_0^4}{(2q_g)^3} e^{-ik_{x_g}x_s} e^{-ik_{y_g}y_s} e^{-iq_g(z_g+z_s)} \int_{-\infty}^{+\infty} dz' \alpha_2(z') \int_{-\infty}^{+\infty} dz'' H(z'-z'') \alpha_1(z'') e^{2iq_g z'} \\
& + \frac{2ik_0^4}{(2q_g)^3} e^{-ik_{x_g}x_s} e^{-ik_{y_g}y_s} e^{-iq_g(z_g+z_s)} \int_{-\infty}^{+\infty} dz' \alpha_1(z') \int_{-\infty}^{+\infty} dz'' H(z'-z'') \alpha_2(z'') e^{2iq_g z'} \\
& - \frac{k_0^6}{(2q_g)^4} e^{-ik_{x_g}x_s} e^{-ik_{y_g}y_s} \int_{-\infty}^{+\infty} dz' e^{iq_g z'} \alpha_1(z') \int_{-\infty}^{+\infty} dz'' e^{iq_g|z'-z''|} \alpha_1(z'') \\
& \times \int_{-\infty}^{+\infty} dz''' e^{iq_g|z''-z'''|} \alpha_1(z''') e^{iq_g z'''}. \qquad \text{(D.4)}
\end{aligned}$$

The first two terms are mathematically analogous to Eq. (B.11) in the derivation of α_2. Equating both sides, cancelling common factors (effectively downward continuing sources and receivers with the reference velocity) gives

$$\begin{aligned}
\int_{-\infty}^{+\infty} \alpha_3(z') e^{2iq_g z'} dz' = & -\frac{2ik_0^2}{2q_g} \int_{-\infty}^{+\infty} dz' \alpha_2(z') \int_{-\infty}^{+\infty} dz'' H(z'-z'') \alpha_1(z'') e^{2iq_g z'} \\
& - \frac{2ik_0^2}{2q_g} \int_{-\infty}^{+\infty} dz' \alpha_1(z') \int_{-\infty}^{+\infty} dz'' H(z'-z'') \alpha_2(z'') e^{2iq_g z'} \\
& + \frac{k_0^4}{(2q_g)^2} \int_{-\infty}^{+\infty} dz' \int_{-\infty}^{+\infty} dz'' \int_{-\infty}^{+\infty} dz''' \alpha_1(z') \alpha_1(z'') \alpha_1(z''') \\
& \times \Big(H(z'-z'') H(z''-z''') e^{2iq_g z'} \\
& + H\,(z'-z'') H(z'''-z'') e^{2iq_g z'} e^{-2iq_g z''} e^{2iq_g z'''} \\
& + H\,(z''-z') H(z''-z''') e^{2iq_g z''} \\
& + H\,(z''-z') H(z'''-z'') e^{2iq_g z'''} \Big). \qquad \text{(D.5)}
\end{aligned}$$

Figure D.2 illustrates this equation diagrammatically where some additional symmetries have been noted. Incorporating these symmetries, we have

$$\int_{-\infty}^{+\infty} \alpha_3(z') e^{2iq_g z'} dz' = I_3(q_g) = 2I_{31}(q_g) + 2I_{32}(q_g) + 2I_{33}(q_g) + I_{34}(q_g) \qquad \text{(D.6)}$$

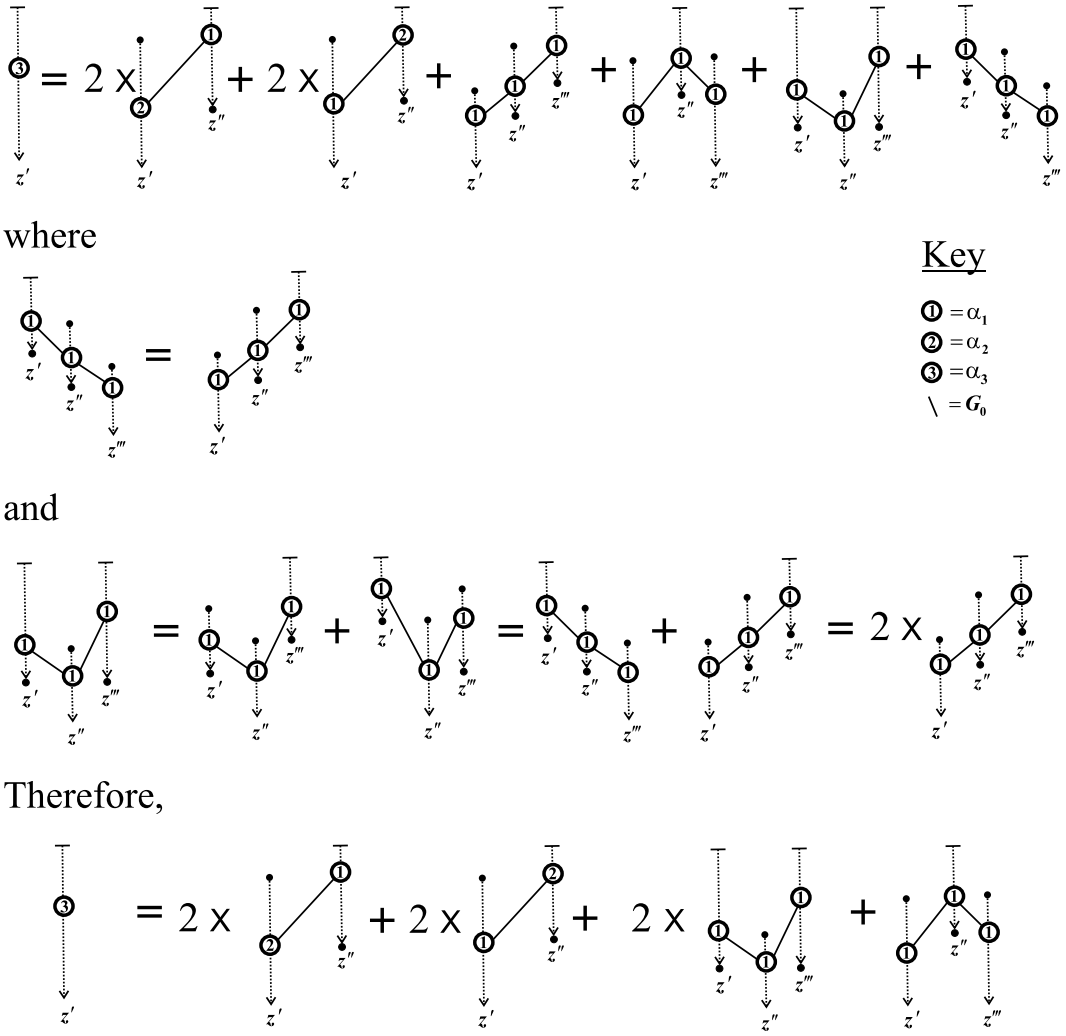

Fig. D.2: Inverse scattering diagrams representing Eqs. (D.5) and (D.6).

where

$$I_{31}(q_g) = k_0^2 \int_{-\infty}^{+\infty} dz' \alpha_2(z') \int_{-\infty}^{+\infty} dz'' H(z'-z'') \alpha_1(z'') \frac{e^{2iq_g z'}}{2iq_g}$$

$$I_{32}(q_g) = k_0^2 \int_{-\infty}^{+\infty} dz' \alpha_1(z') \int_{-\infty}^{+\infty} dz'' H(z'-z'') \alpha_2(z'') \frac{e^{2iq_g z'}}{2iq_g}$$

$$I_{33}(q_g) = -k_0^4 \int_{-\infty}^{+\infty} dz' \int_{-\infty}^{+\infty} dz'' \int_{-\infty}^{+\infty} dz''' \alpha_1(z')\alpha_1(z'')\alpha_1(z''') H(z''-z') H(z''-z''') \frac{e^{2iq_g z''}}{(2iq_g)^2}$$

$$I_{34}(q_g) = -k_0^4 \int_{-\infty}^{+\infty} dz' \int_{-\infty}^{+\infty} dz'' \int_{-\infty}^{+\infty} dz''' \alpha_1(z')\alpha_1(z'')\alpha_1(z''') H(z'-z'') H(z'''-z'') \times \frac{e^{2iq_g z'}}{(2iq_g)^2} e^{-2iq_g z''} e^{2iq_g z'''}.$$

By analogy with Eq. (B.14),

$$I_{31}(q_g) = -\int_{-\infty}^{+\infty} dz' e^{2iq_g z'} \frac{k_0^2}{(2iq_g)^2} \left(\alpha_1(z')\alpha_2(z') + \int_{-\infty}^{+\infty} dz'' H(z'-z'')\alpha_1(z'') \frac{d\alpha_2(z')}{dz'} \right) \tag{D.7}$$

$$I_{32}(q_g) = -\int_{-\infty}^{+\infty} dz' e^{2iq_g z'} \frac{k_0^2}{(2iq_g)^2} \left(\alpha_1(z')\alpha_2(z') + \int_{-\infty}^{+\infty} dz'' H(z'-z'')\alpha_2(z'') \frac{d\alpha_1(z')}{dz'} \right) \tag{D.8}$$

and the third term may be integrated as follows:

$$\begin{aligned}
I_{33}(q_g) =& -k_0^4 \int_{-\infty}^{+\infty} dz' \int_{-\infty}^{+\infty} dz''' \alpha_1(z')\alpha_1(z''') \int_{-\infty}^{+\infty} dz'' \alpha_1(z'') H(z''-z''') H(z''-z') \frac{e^{2iq_g z''}}{(2iq_g)^2} \\
=& k_0^4 \int_{-\infty}^{+\infty} dz' \int_{-\infty}^{+\infty} dz''' \alpha_1(z')\alpha_1(z''') \int_{-\infty}^{+\infty} dz'' \frac{d\alpha_1(z'')}{dz''} H(z''-z''') H(z''-z') \frac{e^{2iq_g z''}}{(2iq_g)^3} \\
&+ 2k_0^4 \int_{-\infty}^{+\infty} dz' \int_{-\infty}^{+\infty} dz''' \alpha_1^2(z')\alpha_1(z''') H(z'-z''') \frac{e^{2iq_g z'}}{(2iq_g)^3} \\
=& -k_0^4 \int_{-\infty}^{+\infty} dz'' \int_{-\infty}^{z''} dz' \int_{-\infty}^{z''} \alpha_1(z') dz''' \alpha_1(z''') \frac{d^2\alpha_1(z'')}{dz''^2} \frac{e^{2iq_g z''}}{(2iq_g)^4} \\
&- 2k_0^4 \int_{-\infty}^{+\infty} dz' \alpha_1(z') \int_{-\infty}^{z'} dz''' \alpha_1(z''') \frac{d\alpha_1(z')}{dz'} \frac{e^{2iq_g z'}}{(2iq_g)^4} \\
&42k_0^4 \int_{-\infty}^{+\infty} dz' \alpha_1(z') \int_{-\infty}^{z'} dz''' \alpha_1(z''') \frac{d\alpha_1(z')}{dz'} \frac{e^{2iq_g z'}}{(2iq_g)^4} \\
&- 2k_0^4 \int_{-\infty}^{+\infty} dz' \alpha_1^3(z') \frac{e^{2iq_g z'}}{(2iq_g)^4} \\
=& -k_0^4 \int_{-\infty}^{+\infty} dz' \frac{e^{2iq_g z'}}{(2iq_g)^4} \\
&\times \left(\left[\int_0^{z'} \alpha_1(z'') dz'' \right]^2 \frac{d^2\alpha_1(z')}{dz'^2} + 6\alpha_1(z') \int_0^{z'} dz'' \alpha_1(z'') \frac{d\alpha_1(z')}{dz'} + 2\alpha_1^3(z') \right).
\end{aligned} \tag{D.9}$$

This break-up is illustrated in Fig. D.3 and is summarized in Fig. D.4. The single term has been split into a purely self-interaction component, a purely separated piece, and a mixed self-interaction and separated diagram term. Only self-interaction at the deepest scattering point is allowed from $I_{33}(q)$.

Meanwhile, we recognize I_{34} as being a starting point in the derivation of the internal multiple attenuation algorithm. As explained by Matson (1997)[1], the initial tests of I_{34} as a potential algorithm proved successful at attenuating internal multiples, but also had the unfortunate

[1] $I_{34} = W_{333}$ in Eq. (5.8) on p. 112 (Matson, 1997), with the substitution $V_1 = k_0^2\alpha_1$. The 1-D normal incidence version is Eq. (4.2) on p. 24 of Araújo (1994).

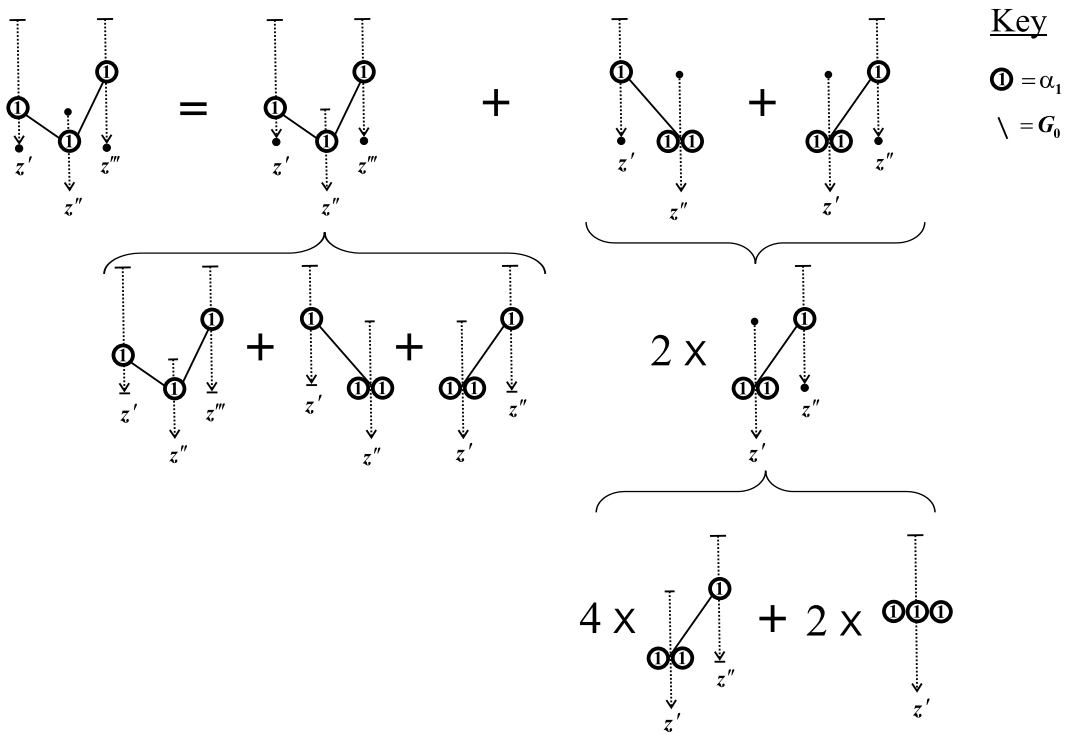

Fig. D.3: *Inverse scattering diagrams representing the separation of* $I_{33}(q)$ *in Eq.(D.9).*

property of simultaneously "altering" primaries. The reason for this will become clearer in the following where it is shown that this term can be further task-separated:

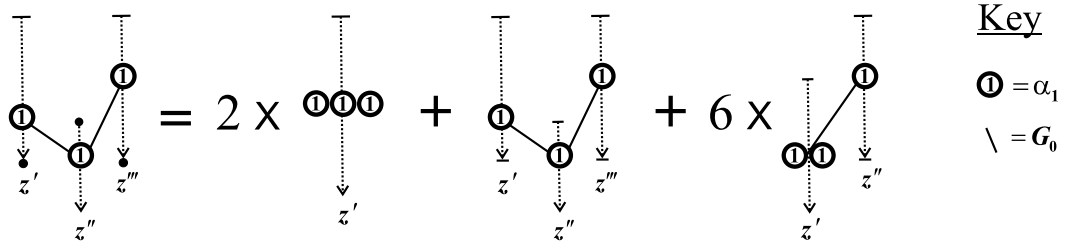

Fig. D.4: Summary of the separation of $I_{33}(q)$ in Eq.(D.9) and Fig.D.3.

$$
\begin{aligned}
I_{34}(q_g) =& -k_0^4 \int_{-\infty}^{+\infty} dz' \int_{-\infty}^{+\infty} dz'' \int_{-\infty}^{+\infty} dz''' \alpha_1(z')\alpha_1(z'')\alpha_1(z''')H(z'-z'')H(z'''-z'') \\
&\times \frac{e^{2iq_g z'}}{(2iq_g)^2} e^{-2iq_g z''} e^{2iq_g z'''} \\
=& k_0^4 \int_{-\infty}^{+\infty} dz'' \int_{-\infty}^{+\infty} dz''' \alpha_1(z'')\alpha_1(z''')H(z'''-z'') \\
&\times \int_{-\infty}^{+\infty} dz' \frac{d\alpha_1(z')}{dz'} H(z'-z'') \frac{e^{2iq_g z'}}{(2iq_g)^3} e^{-2iq_g z''} e^{2iq_g z'''} \\
&+ k_0^4 \int_{-\infty}^{+\infty} dz'' \alpha_1^2(z'') \int_{-\infty}^{+\infty} dz''' \alpha_1(z''')H(z'''-z'') \frac{e^{2iq_g z'''}}{(2iq_g)^3} \\
=& -k_0^4 \int_{-\infty}^{+\infty} dz'' \alpha_1(z'') \int_{-\infty}^{+\infty} dz' \frac{d\alpha_1(z')}{dz'} H(z'-z'') \\
&\times \int_{-\infty}^{+\infty} dz''' \left(\frac{d\alpha_1(z''')}{dz'''} H(z'''-z'') + \alpha_1(z''')\delta(z'''-z'') \right) \frac{e^{2iq_g z'}}{(2iq_g)^4} e^{-2iq_g z''} e^{2iq_g z'''} \\
&- k_0^4 \int_{-\infty}^{+\infty} dz'' \alpha_1^2(z'') \int_{-\infty}^{+\infty} dz''' \left(\frac{d\alpha_1(z''')}{dz'''} H(z'''-z'') + \alpha_1(z''')\delta(z'''-z'') \right) \frac{e^{2iq_g z'''}}{(2iq_g)^4}
\end{aligned}
$$

$$
\begin{aligned}
I_{34}(q_g) =& -k_0^4 \int_{-\infty}^{+\infty} dz'' \alpha_1(z'') \int_{-\infty}^{z''} dz''' \int_{-\infty}^{z''} dz' \frac{d\alpha_1(z''')}{dz'''} \frac{d\alpha_1(z')}{dz'} \frac{e^{2iq_g z'}}{(2iq_g)^4} e^{-2iq_g z''} e^{2iq_g z'''} \\
&- 2k_0^4 \int_{-\infty}^{+\infty} dz''' \int_{-\infty}^{z'''} dz'' \alpha_1^2(z'') \frac{d\alpha_1(z''')}{dz'''} \frac{e^{2iq_g z'''}}{(2iq_g)^4} \\
&- k_0^4 \int_{-\infty}^{z'''} dz'' \alpha_1^3(z'') \frac{e^{2iq_g z''}}{(2iq_g)^4}
\end{aligned}
\tag{D.10}
$$

The first of the three terms in Eq. (D.10) is the portion of α_3 that attenuates internal multiples (Araújo, 1994). The other two terms act on (i.e., process) primaries, which is why

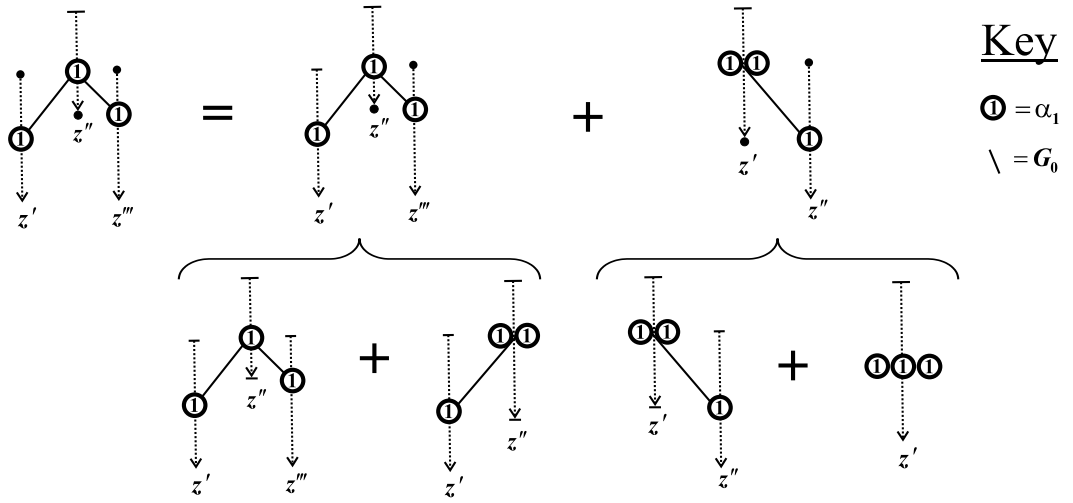

Fig. D.5: *Inverse scattering diagrams representing the separation of* $I_{34}(q)$ *in Eq.(D.10).*

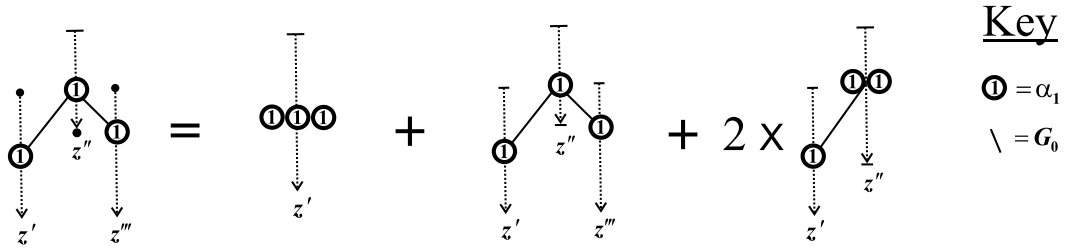

Fig. D.6: *Summary of the separation of* $I_{34}(q)$ *in Eq.(D.10).*

I_{34} was not fully task-separated before. We may rewrite the first term in Eq. (D.10) as

$$\alpha_3^{\mathrm{IM}}(q_g) = -\frac{k_0^4}{(2iq_g)^4}\int_{-\infty}^{+\infty} dz' \frac{d\alpha_1(z')}{dz'} e^{2iq_g z'} \int_{-\infty}^{z'} dz'' \alpha_1(z'') e^{-2iq_g z''} \int_{z''}^{\infty} dz''' \frac{d\alpha_1(z''')}{dz'''} e^{2iq_g z'''} \tag{D.11}$$

for comparison with Eq.(5.12) in Matson (1997) and its 2-D formulation as Eq. (37) in Weglein et al. (1997). The noticeable difference is in the integrand, where in Eq. (D.11) one of the α_1's is not a derivative. This is because the internal multiples appear block-like in the inversion for α. Summarizing Eqs. (D.6–D.11) and inverse Fourier transforming, holding p

constant, gives

$$\begin{aligned}\alpha_3(z,p) =& \frac{2}{4\cos^2\theta_0}\left(\alpha_1(z,p)\alpha_2(z,p) + \int_{-\infty}^{+\infty} dz' H(z-z')\alpha_1(z',p)\frac{\partial\alpha_2(z,p)}{\partial z}\right) \\ &+ \frac{2}{4\cos^2\theta_0}\left(\alpha_2(z,p)\alpha_1(z,p) + \int_{-\infty}^{+\infty} dz' H(z-z')\alpha_1(z',p)\frac{\partial\alpha_2(z,p)}{\partial z}\right) \\ &- \frac{2}{16\cos^4\theta_0}\left(\left[\int_0^z \alpha_1(z',p)dz'\right]^2 \frac{\partial^2\alpha_1(z,p)}{\partial z^2}\right. \\ &\qquad\left. + 3\,\alpha_1(z,p)\int_0^z dz'\alpha_1(z',p)\frac{\partial\alpha_1(z,p)}{\partial z} + \alpha_1^3(z,p)\right) \\ &- \frac{1}{16\cos^4\theta_0}\left(2\left[\int_0^z \alpha_1^2(z',p)dz'\right]\frac{\partial\alpha_1(z,p)}{\partial z} + \alpha_1^3(z,p)\right) + \alpha_3^{\mathrm{IM}}(z,p) \qquad \text{(D.12)}\end{aligned}$$

Substituting $\alpha_2(z,p)$ into Eq. (D.12) we find (see Figs. D.7 and D.8)

$$\begin{aligned}\alpha_3(z,p) =& \frac{2}{8\cos^4\theta_0}\left(2\alpha_1^3(z,p) + 6\alpha_1(z,p)\int_0^z \alpha_1(z',p)dz'\frac{\partial\alpha_1(z,p)}{\partial z}\right. \\ &\qquad\left. + \left[\int_0^z \alpha_1(z',p)dz'\right]^2 \frac{\partial^2\alpha_1(z,p)}{\partial z^z}\right) \\ &- \frac{2}{16\cos^4\theta_0}\left(\left[\int_0^z \alpha_1(z',p)dz'\right]^2 \frac{\partial^2\alpha_1(z,p)}{\partial z^2}\right. \\ &\qquad\left. + 3\,\alpha_1(z,p)\int_0^z dz'\alpha_1(z',p)\frac{\partial\alpha_1(z,p)}{\partial z} + \alpha_1^3(z,p)\right) \\ &- \frac{1}{16\cos^4\theta_0}\left(2\left[\int_0^z \alpha_1^2(z',p)dz'\right]\frac{\partial\alpha_1(z,p)}{\partial z} + \alpha_1^3(z,p)\right) + \alpha_3^{\mathrm{IM}}(z,p). \qquad \text{(D.13)}\end{aligned}$$

Notice that the terms derived from $G_0V_1G_0V_2G_0$ and $G_0V_2G_0V_1G_0$ have the opposite sign to the terms derived from $G_0V_1G_0V_1G_0V_1G_0$. Summing all like terms gives

$$\begin{aligned}\alpha_3(z,p) =& \frac{1}{16\cos^4\theta_0}\left(3\alpha_1^3(z,p) + 2\left[\int_0^z \alpha_1(z',p)dz'\right]^2 \frac{\partial^2\alpha_1(z,p)}{\partial z^z}\right. \\ &+ 12\alpha_1(z,p)\int_0^z \alpha_1(z',p)dz'\frac{\partial\alpha_1(z,p)}{\partial z} - 2\left[\int_0^z \alpha_1^2(z',p)dz'\right]\left.\frac{\partial\alpha_1(z,p)}{\partial z}\right) \\ &+ \alpha_3^{\mathrm{IM}}(z,p) \qquad \text{(D.14)}\end{aligned}$$

The $G_0V_1G_0V_2G_0$ and $G_0V_2G_0V_1G_0$ terms contain parts that are opposite in polarity to their cousins in the $G_0V_1G_0V_1G_0G_0$ and therefore, to some degree, these terms counteract each other. This implies that a straight-ahead implementation of the inverse series contains certain inefficiencies (see also discussion by Innanen, 2003). The strategy of task separation coupled with an understanding of how nonlinear direct inversion can be accomplished presents an opportunity to avoid any such inherent inefficiencies.

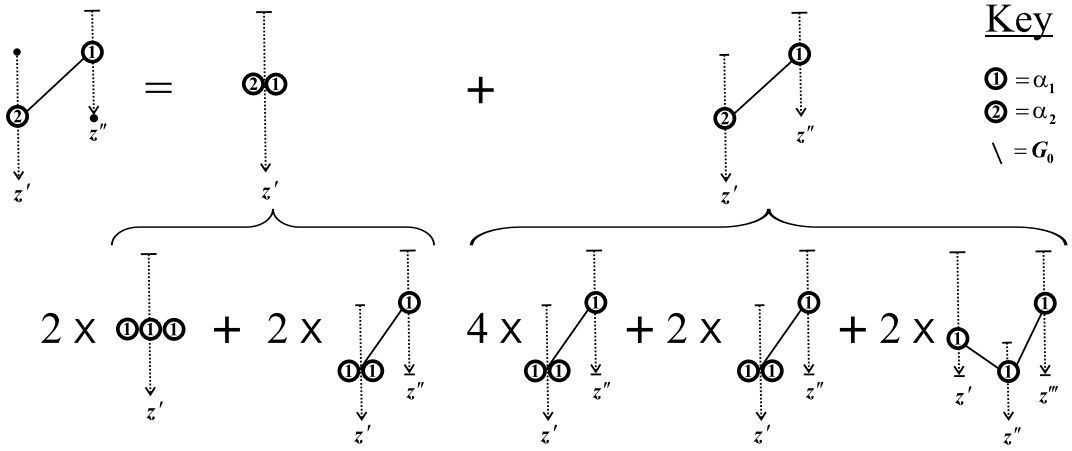

Fig. D.7: *The break-up of the $G_0V_2G_0V_1G_0$ term into task-specific pieces.*

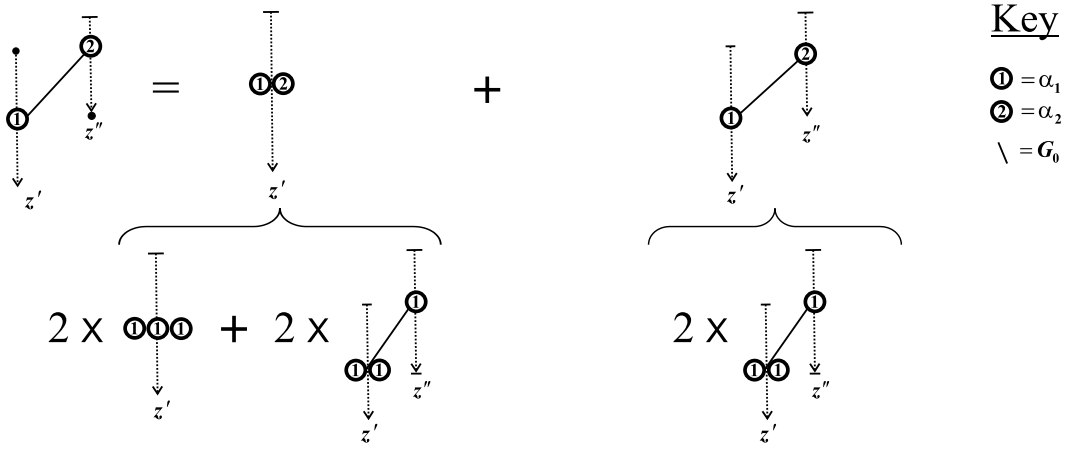

Fig. D.8: *The break-up of the $G_0V_1G_0V_2G_0$ term into task-specific pieces.*